Springer ThesesRecognizing Outstanding Ph.D. Research

Chao Feng

Theoretical and Experimental Studies on Novel High-Gain Seeded Free-Electron Laser Schemes



Springer Theses

Recognizing Outstanding Ph.D. Research

Aims and Scope

The series "Springer Theses" brings together a selection of the very best Ph.D. theses from around the world and across the physical sciences. Nominated and endorsed by two recognized specialists, each published volume has been selected for its scientific excellence and the high impact of its contents for the pertinent field of research. For greater accessibility to non-specialists, the published versions include an extended introduction, as well as a foreword by the student's supervisor explaining the special relevance of the work for the field. As a whole, the series will provide a valuable resource both for newcomers to the research fields described, and for other scientists seeking detailed background information on special questions. Finally, it provides an accredited documentation of the valuable contributions made by today's younger generation of scientists.

Theses are accepted into the series by invited nomination only and must fulfill all of the following criteria

- They must be written in good English.
- The topic should fall within the confines of Chemistry, Physics, Earth Sciences, Engineering and related interdisciplinary fields such as Materials, Nanoscience, Chemical Engineering, Complex Systems and Biophysics.
- The work reported in the thesis must represent a significant scientific advance.
- If the thesis includes previously published material, permission to reproduce this must be gained from the respective copyright holder.
- They must have been examined and passed during the 12 months prior to nomination.
- Each thesis should include a foreword by the supervisor outlining the significance of its content.
- The theses should have a clearly defined structure including an introduction accessible to scientists not expert in that particular field.

More information about this series at http://www.springer.com/series/8790

Chao Feng

Theoretical and Experimental Studies on Novel High-Gain Seeded Free-Electron Laser Schemes

Doctoral Thesis accepted by University of Chinese Academy of Sciences, China



Author
Dr. Chao Feng
Shanghai Institute of Applied Physics
Chinese Academy of Sciences
Shanghai
People's Republic of China

Supervisor
Prof. Zhentang Zhao
Shanghai Institute of Applied Physics
Chinese Academy of Sciences
Shanghai
People's Republic of China

ISSN 2190-5053 ISSN 2190-5061 (electronic) Springer Theses ISBN 978-3-662-49064-8 ISBN 978-3-662-49066-2 (eBook) DOI 10.1007/978-3-662-49066-2

Library of Congress Control Number: 2015957787

© Springer-Verlag Berlin Heidelberg 2016

This work is subject to copyright. All rights are reserved by the Publisher, whether the whole or part of the material is concerned, specifically the rights of translation, reprinting, reuse of illustrations, recitation, broadcasting, reproduction on microfilms or in any other physical way, and transmission or information storage and retrieval, electronic adaptation, computer software, or by similar or dissimilar methodology now known or hereafter developed.

The use of general descriptive names, registered names, trademarks, service marks, etc. in this publication does not imply, even in the absence of a specific statement, that such names are exempt from the relevant protective laws and regulations and therefore free for general use.

The publisher, the authors and the editors are safe to assume that the advice and information in this book are believed to be true and accurate at the date of publication. Neither the publisher nor the authors or the editors give a warranty, express or implied, with respect to the material contained herein or for any errors or omissions that may have been made.

Printed on acid-free paper

This Springer imprint is published by SpringerNature The registered company is Springer-Verlag GmbH Berlin Heidelberg

Parts of this thesis have been published in the following journal articles:

- C. Feng, H.X. Deng, D. Wang, Z.T. Zhao, New J. Phys. 16 (2014) 043021.
- C. Feng, T. Zhang, H.X. Deng, Z.T. Zhao, Phys. Rev. ST Accel. Beams 17 (2014) 070701.
- C. Feng, L. Shen, M. Zhang, D. Wang, Z.T. Zhao, D. Xiang, Nucl. Instrum. Methods A 712 (2013) 113.
- C. Feng, H.X. Deng, G.L. Wang, D. Wang, Z.T. Zhao, Phys. Rev. ST Accel. Beams 16 (2013) 060705.
- C. Feng, J.H. Chen, Z.T. Zhao, Phys. Rev. ST Accel. Beams 15 (2012) 080703.
- C. Feng, M. Zhang, G.Q. Lin, et al., Chin. Sci. Bull. 57 (2012) 3423.
- C. Feng, T. Zhang, J.H. Chen, et al., Phys. Rev. ST Accel. Beams 14 (2011) 090701.
- C. Feng, Z.T. Zhao, Chin. Sci. Bull. 55 (2010) 221.
- B. Liu, W.B. Li, J.H. Chen, et al., Phys. Rev. ST Accel. Beams, 16 (2013) 020704.
- Z.T. Zhao, D. Wang, J.H. Chen, et al., Nature Photon. 6 (2012) 360.

Supervisor's Foreword

High-gain free-electron lasers (FELs), serving as high-intensity, ultra-short coherent light sources, are being actively developed around the world in the past decades. Applications for FELs in the EUV and X-ray regimes are practically unlimited: they can be used within a wide range of femtochemistry, for ultra-high resolution imaging, the investigation of the dynamics in atomic and biological systems and for many more experiments in leading edge sciences.

Study of the operation scheme is one of the core issues of modern FEL physics research and is always an important topic for the design of high-gain FEL facilities. Till date, self-amplified spontaneous emission (SASE) and high-gain harmonic generation (HGHG) are the two leading candidates for approaching EUV to x-ray region. Most of the existing high-gian FEL facilities are based on the SASE principle, which can provide extremely high-intensity, ultra-short light pulses with good spatial coherence but poor temporal coherence and relatively large shot-to-shot fluctuations. HGHG holds the ability for significantly improving the FEL temporal coherence and stability, which has been experimentally demonstrated. However, the high harmonic up-conversion efficiency limited the wavelength cover range of a single stage HGHG. To overcome these problems and meet the new requirements of FEL users, novel high-gain FEL schemes have been proposed in recent years.

This Ph.D. thesis of Dr. Chao Feng mainly focuses on the study of novel high-gain FEL schemes with external seed lasers. The technique of manipulating the phase space of electron beam, which is widely used in novel seeded FEL schemes, has been systematically studied. Several novel FEL schemes have been proposed for the generation of intense coherent FEL pulse with short wavelength, sub-femtosecond pulse length or multiple carrier frequency properties, which meet the requirements of FEL users. Experiments have been carried out for the recently proposed FEL schemes such as echo-enabled harmonic generation and cascaded high-gain harmonic generation. New photon/electron beam diagnostic methods have been developed for these experiments based on the Shanghai deep ultraviolet FEL facility.

Researches on high-gain FELs have been just started in China. However, we already have three high-gain seeded FEL facilities under construction or operation. Investigations on novel seeded FEL schemes will help us to further understand the theoretical basis and functioning of the existing FEL schemes and provide us more options for the operation of these FEL facilities. We also hope that the new methods and techniques drawn from this study will be beneficial to other presently existing or planned high-gain FEL facilities.

Shanghai September 2015 Prof. Zhentang Zhao

Acknowledgments

This thesis was guided by Prof. Zhentang Zhao. I was extremely fortunate to have Prof. Zhentang Zhao as my advisor and mentor at the Shanghai Institute of Applied Physics, Chinese Academy of Science. I would like to express my sincere gratitude to Prof. Zhentang Zhao for his continual support and encouragement during the course of my Ph.D. He has given me every opportunity I could have wished for, and I am always inspired by his motivation, enthusiasm and immense knowledge.

I am heartily thankful to Prof. Dong Wang for his help and guidance during the entire research period. Professor Dong Wang was very helpful and patient as I grew accustomed to being part of a large team for FEL experiment collaboration and learned accelerator commissioning in the process.

I am grateful to Bo Liu, Haixiao Deng, Jianhui Chen, Qiang Gu, Meng Zhang, Wencheng Fang, Xingtao Wang and Tong Zhang for their selfless support and helpful discussions in FEL theory and experimental research. I would also like to thank Prof. Chuangxiang Tang, Prof. Qika Jia, Prof. Zhirong Huang, Dr. Yuantao Ding, Prof. Alex Chao and Prof. Dao Xiang for their encouragement, insightful comments and kindly help in my research.

Finally, I would like to thank my parents for their love, patience, caring support and perspective.

Contents

1			n	1 6			
2	Basic Theory of FEL						
	2.1	Energy	y Exchange Equation	9			
	2.2	Phase	Evolution Equation	11			
	2.3						
	2.4	Equati	ons for Harmonic Generation Seeded FEL Schemes	13			
		2.4.1	HGHG-FEL	14			
		2.4.2	EEHG-FEL	16			
	Refe	erences		17			
3	The	oretical	Studies on Novel High-Gain Seeded FEL Schemes	19			
	3.1	The E	lectron Beam Phase Space Manipulation Techinique	19			
	3.2	Pre-de	ensity Modulation of the Electron Beam				
		for En	hancing Seeded FELs	27			
	3.3						
		3.3.1	Analytical Calculations	32			
		3.3.2	Hard X-Ray FEL Based on the EESHG Scheme	34			
	3.4						
		3.4.1	Principles of PEHG	36			
		3.4.2	Three-Dimensional Manipulation for Realizing				
			the Phase Merging Effect	42			
		3.4.3	Generation of Soft X-Ray Radiation Based				
			on a Single Stage PEHG	44			
	3.5						
		with a	Mode-Locked Seeded FEL	46			
		3.5.1	Mode-Locking of a Seeded FEL	47			
		3.5.2	Generation of Intense APTs	50			
	3.6	Chirpe	ed Pulse Amplification of a Seeded FEL	54			
		3.6.1	Chirped Pulse Amplification in a Seeded FEL	55			
		3.6.2	Start-to-End Simulations Based on the SDUV-FEL	57			

xii Contents

	3.7	Slippa	ge Effect on Energy Modulation in Seeded FELs	61	
		3.7.1	Energy Modulation with Slippage Effect	63	
		3.7.2	HGHG and EEHG with Short Seed Laser Pulses	67	
		3.7.3	3D Simulations for SXFEL	70	
		3.7.4	Slippage-Boosted by a Sub-harmonic Modulator	72	
	Refe			74	
4	Exp	erimen	tal Studies on Novel High-Gain Seeded FEL Schemes	77	
	4.1		uction of the SDUV-FEL	77	
4.2 Measurement of the Slice Energy Spread of Electron					
		Beam	via CHG	80	
		4.2.1	CHG Based Energy Spread Measurement Method	81	
		4.2.2	Experimental Results at the SDUV-FEL	84	
	4.3	Experi	imental Studies of the EEHG	90	
		4.3.1	Energy Chirp Effects on HGHG and EEHG	90	
		4.3.2	Design Studies for the EEHG Experiment		
			at the SDUV-FEL	92	
		4.3.3	Experimental Results of EEHG Lasing		
			at the SDUV-FEL	93	
	4.4	Experi	imental Studies of the Cascaded HGHG	96	
		4.4.1	Design Studies for the Cascaded HGHG Experiment		
			at the SDUV-FEL	96	
		4.4.2		-	
			Experiment at the SDUV-FEL	103	
	Refe	rences		105	
_				107	
5	Con	ciusion	s and Prospects	107	

Chapter 1 Introduction

Abstract In this chapter, we first give a quick review of the general idea and applications of the accelerator-based light sources. Then a brief introduction of the development history and current status of high-gain FEL facilities around the world are given. After that, we show the evolutions of high-gain FEL schemes either based on SASE or external seeding lasers. The advantages and limits of these schemes have also been discussed.

Keywords Storage rings · High-gain FELs · SASE · Seeded FELs

The development of new kinds of light sources often leads to dramatic change in various areas of science and technology. It is not unusual that new fields appear due to the appearance of a new kind of light source. In the late 19th century, the discovery of x-ray opens the door for the understanding of matter on the level of atoms, electrons, and spins. In 1960s, the invention of the laser provided scientists with a stronger and fully coherence source of light, which can significantly improve the spatial and temporal resolutions of an experiment measurement. The introduction of synchrotron light sources dramatically increases the speed of traditional x-ray measurements and allowed the collection of much higher quality data. The most spectacular impact of synchrotron light sources based on electron storage rings (SRs) maybe in the structure determination of biological systems. Thousands of protein structures were solved with atomic resolution using SRs in the last decades.

However, the development of SRs seems already reached the technical limites. Therefore a new tool, the free-electron laser (FEL) has become the new center of interest. FEL is such a device that uses relativistic electron beams passing through a periodic magnetic structure to generate coherent radiation. The electron beam in FEL works as the lasing medium in a conventional laser. FEL usually consists of a linear accelerator (linac) and an undulator system, as shown in Fig. 1.1. The linac provides high brightness electron beams with relativistic energy in vacuum. Then the electron beam is sent through a periodic lattice of alternating magnetic dipolar fields, known as an undulator. The wiggle of the electron beam in the undulator results in the initial synchrotron radiation. After a long undulator beam line, the

1

2 1 Introduction

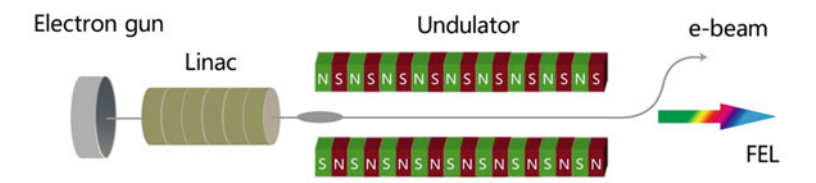


Fig. 1.1 Schematic layout of a FEL

initial light will be amplified and quasicoherent intense radiation will be produced. The extreme high intensity together with the excellent transverse coherence of FEL provide about 10 orders of magnitude improvement in peak brightness above that offered by the synchrotron radiation sources based on SRs.

Compared with the conventional lasers, FELs have the advantage of tunable wavelength from THz to x-ray, high intensity up to 10–100 GW and ultrafast time structures at the femtosecond to sub-femtosecond level. Because of the ultra-high brightness and full coherence properties, a high gain X-ray FEL is superior to any advanced synchrotron light sources and will bring lots of new understanding to many scientific fields, such as molecular biology, materials science, catalysis engineering and medical science.

There are already many FEL facilities around the world, as shown in Fig. 1.2. Most of these facilities are based on the self-amplified spontaneous emission (SASE) [1, 2], where the radiation amplification process starts from the electron beam shot noise. The first experimental demonstration of SASE principle in the infrared wavelength range was carried out in 1996 [3, 4]. In 2000, the first saturation of SASE in the visible wavelength was achieved at Argonne National Laboratory (ANL) [5, 6]. After that, the FEL output wavelength has been extended



Fig. 1.2 High-gain FEL facilities all over the world

1 Introduction 3

Name/Location	Minimum	Energy	Operation	Status		
	wavelength (nm)	(GeV)	scheme			
Hard x-ray FEL						
LCLS/SLAC@USA	0.15	14.3	SASE	Operational		
SACLA/Spring-8@Japan	0.06	8	SASE	Operational		
European-XFEL/DESY@Germany	0.1	17.5	SASE	Construction		
PAL XFEL/PAL@Korea	0.1	10	SASE	Construction		
SwissFEL/PSI@Switzerland	0.1	6	SASE	Construction		
Soft x-ray FEL						
FLASH/DESY@Germany	4.45	1.2	SASE	Operational		

1.7

2.4

0.84

4

Cascaded

SASE/Seeded

HGHG

SASE

Cascaded

HGHG

Operational

Construction

Construction

Construction

Table 1.1 Current High-gain x-ray FEL facilities all over the world

0.6

8.8

4

FERMI/ELETTRA@Italy

LCLS-II/SLAC@USA

SXFEL/SINAP@China

SPARX/Italy

to VUV wavelength at DESY in 2001 [7, 8] and reach 13 nm in 2006 [9]. The world-first hard x-ray FEL facility, the LCLS [10], was born in 2009 at SLAC. The LCLS can be operated at x-ray wavelengths from 2.2 to 0.12 nm. In addition to the LCLS and FLASH, other FELs now operating include the vacuum ultraviolet FEL in Italy called FERMI@Elettra [11] and a hard x-ray FEL called SACLA [12], part of Japan's RIKEN research institute. A second soft x-ray installation at DESY, FLASH-2, is beginning operations [13], and a hard and soft x-ray FEL facility in South Korea (PAL-XFEL) will be completed soon [14]. Other projects under construction include the large European XFEL project at DESY [15] and the SwissFEL at the Paul Scherrer Institute in Switzerland [16]. In China, we now have one high-gain FEL, the Shanghai Deep Ultraviolet FEL test facility (SDUV-FEL) [17], in operation and two more high-gain FEL facilities, the Shanghai Soft x-ray FEL test facility (SXFEL) [18] and the Dalian Coherent light source user facility (DCLS) [19] under construction. Table 1.1 lists some high-gain x-ray FEL facilities that are either operational or under construction all over the world.

The operation scheme is the central of interest of FEL physics. Up to now, SASE is still the main operation mode for high-gain FELs. As shown in Fig. 1.3a, the undulator system for SASE is quite simple. The initial spontaneous emission that produced by the electron beam shot noise is amplified by continuous interaction with the electron beam over the full undulator length until the FEL reachs the saturation power. SASE-FEL holds the capability of producing intense x-ray FEL with perfect transverse coherence. However, the output of SASE FEL typically has poor temporal coherence and large shot-to-shot power fluctuation due to the start-up from noise.

4 1 Introduction

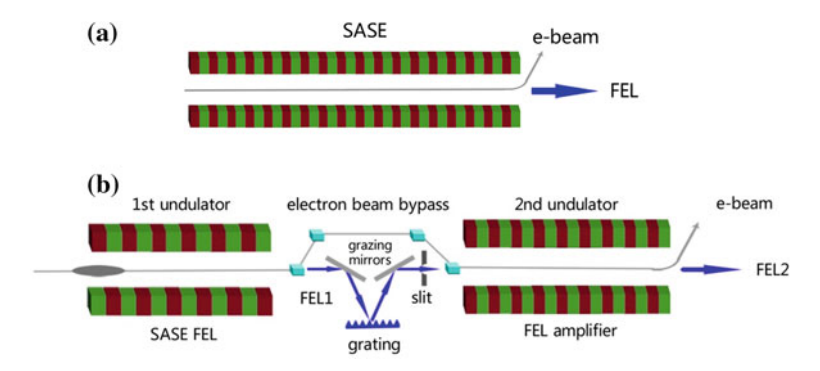


Fig. 1.3 SASE (a) and self-seeding (b)

The temporal coherence of SASE can be significantly improved by the self-seeding scheme [20–23], which employs double undulator configuration, as shown in Fig. 1.3b. The SASE radiation generated by the first undulator section is purified by an x-ray monochromator and this monochromatic light is further amplified until saturation by the same electron beam in the second undulator section.

The temporal coherence and intrinsic pulse energy fluctuations of the SASE and self-seeding schemes can be further improved by using seeded FELs with external seed lasers, as shown in Fig. 1.4. The output property of a seeded FEL is a direct map of the seed laser's attributes which ensures high degree of temporal coherence and small pulse energy fluctuations with respect to SASE. With respect to the self-seeding, seeding with external lasers has the additional advantage of that the FEL pulse is locked to an external signal. This allows a more precise time synchronization, which is especially important for the pump-probe experiments. From now on we will be referring to the laser-based seeding schemes simply as seeded FELs.

The simplest seeded FEL is so called the direct seeding, as illustrated in Fig. 1.4a. In this scheme, an intense laser source is empolyed to dominate the incoherent spontaneous emission at the very beginning of the undulator. After that, the coherent radiation can be amplified expotentially until saturation. At short wavelength, the only available coherent source is generated though the high-harmonic generation (HHG) process, which benefit from the highly nonlinear interaction of a very intense optical laser pulse with a rare gas. The HHG direct seeding scheme has been successfully demonstrated at VUV wavelengths [24]. However, due to the strong intensity drop of HHG at very high harmonics, the HHG direct seeding is still not suitable for x-ray FEL generation in the near future.

To circumvent the need for the seed source at short wavelength, frequency up-conversion schemes relied on optical-scale electron beam phase space manipulation have been envisioned to convert the commercial available seed source to shorter wavelength. The most famous frequency up-conversion scheme is so called the high-gain harmonic generation (HGHG) (Fig. 1.4b) [25], which consists of two

1 Introduction 5

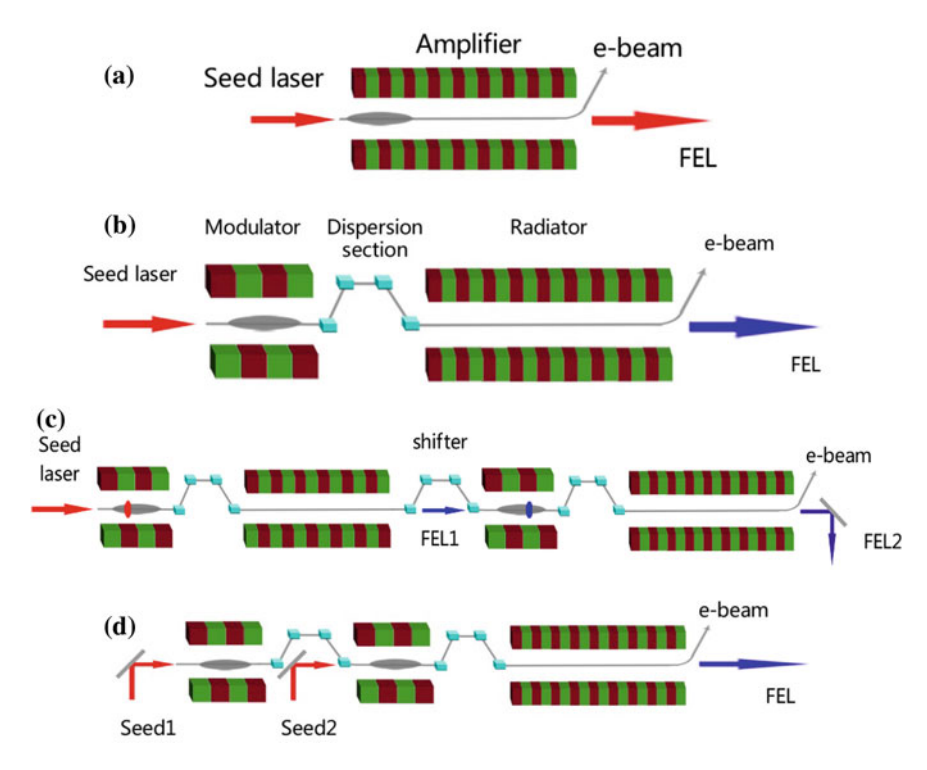


Fig. 1.4 High-gain FEL with external seeding lasers a direct seeding, b HGHG, c cascaded HGHG and d EEHG

undulators separated by a small chicane. A seed laser pulse is first used to interact with the electrons in a short undulator, called modulator, to generate a sinusoidal energy modulation in the electron beam longitudinal phase space at the scale of seed laser wavelength. The formed energy modulation then develops into an associated density modulation by a dispersive magnetic chicane, called the dispersion section (DS). High harmonic components of the seed laser frequency can be generated in the electron beam density distribution, making this approach powerful for generating short wavelength FEL pulses. However, significant bunching at higher harmonics usually needs to strengthen the energy modulation in HGHG, which will result in a degradation of the amplification process in the radiator. Thus the requirement of FEL amplification on the beam energy spread prevents the possibility of reaching short wavelength in a single stage HGHG. For this reason, the cascading stages of HGHG scheme (Fig. 1.4c) [26] have been proposed. The FEL generated by intermediate radiator can be used as the seed laser for the following HGHG stage with the help of the "fresh bunch" technique. Analysis within the framework of idealized models promisingly indicates that cascading several stages of HGHG can produce fully coherent soft x-rays. The cascaded HGHG scheme seems an attractive way for the soft x-ray light source. We can find 6 1 Introduction

in Table 1.1 that at least two soft x-ray facilities, the FERMI and the SXFEL, adopt the cascaded HGHG scheme as the main operation mode.

In order to improve the frequency multiplication efficiency in a single stage, more complicated phase space manipulation techniques have been developed. The most famous one is the so called echo-enabled harmonic generation (EEHG) (Fig. 1.4d) [27, 28], which employs two modulators and two dispersion sections to introduce echo effect into the electron beam phase space for enhancing the frequency multiplication efficiency with a relatively small energy modulation. The analytical calculations and simulation results imply that a single-stage EEHG FEL is able to generate high power soft X-ray radiation with narrow bandwidth close to Fourier transform limited directly from a UV seed source [29, 30]. However, when compared with HGHG, the microbunching that generated by EEHG seems more sensitive to the machine and electron beam parameters. What's more, the CSR and ISR effects induced by the first DS may smear out the fine structure of EEHG.

From above discussions, we can find that although numbers of novel high-gain FEL schemes have been proposed and technically developed to improve the performances of the classical SASE and HGHG, they still have their own disadvantages and limitations. Proof-of-principle experiments are desired to test and study these novel principles. On the other hand, as the numbers of FEL facilities and users increase, new demands for FEL output properties, such as ultra-high peak power, fully coherence, attosecond pulse length, two color, etc. have been proposed. New FEL operation schemes are needed to meet these requirements. As a result, the proposal and demonstraten of novel high-gain FEL schemes is still a hot topic in FEL community in nowadays. In this thesis, we will focus on the theoretical and experimental studies on novel high-gain seeded FEL schemes.

References

- Kondratenko AM, Saldin EL (1980) Generating of coherent radiation by a relativistic electron beam in an ondulator. Part Accel 10:207–216
- 2. Bonifacio R, Pellegrini C, Narducci LM (1984) Collective instabilities and high-gain regime in a free electron laser. Opt Commun 50(6):373–378
- 3. Bonifacio R, Pierini P, Pellegrini C et al (1994) Slippage, noise and superradiant effects in the UCLA FEL experiment. Nucl Instrum Methods Phys Res Sect A Accel Spectrom Detect Assoc Equip 341(1):285–288
- 4. Saldin EL, Schneidmiller EA, Yurkov MV (1999) Numerical simulations of the UCLA experiments on a high gain SASE FEL. In: The sixteenth advanced international committee on future accelerators beam dynamics workshop on nonlinear and collective phenomena in beam physics, vol. 468, no. 1. AIP Publishing, pp. 321–333
- Arnold ND, Attig J, Banks G et al (2001) Observation and analysis of self-amplified spontaneous emission at the APS low-energy undulator test line. Nucl Instrum Methods Phys Res Sect A Accel Spectrom Detect Assoc Equip 475(1):28–37
- Lewellen JW, Milton SV, Gluskin E et al (2002) Present status and recent results from the APS SASE FEL. Nucl Instrum Methods Phys Res Sect A Accel Spectrom Detect Assoc Equip 483(1):40–45

References 7

 Ischebeck R, Feldhaus J, Gerth C et al (2003) Study of the transverse coherence at the TTF free electron laser. Nucl Instrum Methods Phys Res Sect A Accel Spectrom Detect Assoc Equip 507(1):175–180

- 8. Dohlus M, Flöttmann K, Kozlov OS et al (2004) Start-To-End Simulations of SASE FEL at the TESLA Test Facility, Phase I: comparison with experimental results. Nucl Instrum Methods Phys Res Sect A Accel Spectrom Detect Assoc Equip 528(1):448–452
- 9. Ackermann W, Asova G, Ayvazyan V et al (2007) Operation of a free-electron laser from the extreme ultraviolet to the water window. Nat Photonics 1(6):336–342
- 10. Emma P, Akre R, Arthur J et al (2010) First lasing and operation of an ångstrom-wavelength free-electron laser. Nat Photonics 4(9):641–647
- 11. Allaria E, Appio R, Badano L et al (2012) Highly coherent and stable pulses from the FERMI seeded free-electron laser in the extreme ultraviolet. Nat Photonics 6(10):699–704
- 12. Ishikawa T, Aoyagi H, Asaka T et al (2012) A compact X-ray free-electron laser emitting in the sub-angstrom region. Nat Photonics 6(8):540–544
- 13. Schreiber S, Faatz B, Feldhaus J et al (2011) Status of the FEL user facility FLASH. In: 33rd FEL Conference (FEL2011), Shanghai, August 2011, JACOW, p 267
- Kang HS, Kim KW, Ko IS (2013) Current status of PAL-XFEL project. In: Proceedings of the 4th International Particle Accelerator Conference (IPAC2013), Shanghai, May 2013, JACoW, p 2074
- Altarelli M, Brinkmann R, Chergui M et al (2007) The European x-ray free-electron laser.
 Technical design report, DESY 2006-097, DESY XFEL Project Group, ISBN 978-3-935702-17-1
- Ganter R (2010) SwissFEL-Conceptual design report. Paul Scherrer Institute (PSI), Villigen (Switzerland). Funding organisation: Paul Scherrer Institute (PSI), Villigen (Switzerland)
- Zhao ZT, Dai ZM, Zhao XF et al (2004) The Shanghai high-gain harmonic generation DUV free-electron laser. Nucl Instrum Methods Phys Res Sect A Accel Spectrom Detect Assoc Equip 528(1):591–594
- Zhao ZT, Chen SY, Yu LH et al (2011) Shanghai soft X-ray free electron laser test facility. In: Proceedings of the 2nd international particle accelerator conference (IPAC2011), San Sebastián, Spain, JACoW, p 3011
- 19. Deng HX, Zhang M, Duan G et al (2014) Simulation studies on laser pulse stability for Dalian coherent light source. Chinese Physics C 38(2):028101
- 20. Feldhaus J, Saldin EL, Schneider JR et al (1997) Possible application of X-ray optical elements for reducing the spectral bandwidth of an X-ray SASE FEL. Optics Communications 140(4):341–352
- Saldin EL, Schneidmiller EA, Shvyd'ko YV et al (2001) X-ray FEL with a meV bandwidth.
 Nucl Instrum Methods Phys Res Sect A Accel Spectrom Detect Assoc Equip 475(1):357–362
- Geloni G, Kocharyan V, Saldin E (2011) A novel self-seeding scheme for hard X-ray FELs.
 J Mod Opt 58(16):1391–1403
- Amann J, Berg W, Blank V et al (2012) Demonstration of self-seeding in a hard-X-ray free-electron laser. Nat Photonics 6(10):693–698
- Lambert G, Hara T, Garzella D et al (2008) Injection of harmonics generated in gas in a free-electron laser providing intense and coherent extreme-ultraviolet light. Nat Phys 4:296– 300
- 25. Yu LH (1991) Generation of intense UV radiation by subharmonically seeded single-pass free-electron lasers. Phys Rev A 44(8):5178–5193
- Yu LH, Ben-Zvi I (1997) High-gain harmonic generation of soft X-rays with the "fresh bunch" technique. Nucl Instrum Methods Phys Res Sect A Accel Spectrom Detect Assoc Equip 393 (1):96–99
- Stupakov G (2009) Using the beam-echo effect for generation of short-wavelength radiation. Phys Rev Lett 102(7):074801
- Xiang D, Stupakov G (2009) Echo-enabled harmonic generation free electron laser. Phys Rev Spec Top—Accel Beams 12(3):030702

8 1 Introduction

29. Feng C, Wang D, Zhao ZT (2012) Proceedings of the 3rd international particle accelerator conference (IPAC2012) New Orleans, Louisiana, May 2012, p 1724

30. Zhao ZT, Wang D, Chen JH et al (2012) First lasing of an echo-enabled harmonic generation free-electron laser. Nat Photonics 6(6):360–363

Chapter 2 Basic Theory of FEL

Abstract This chapter shows the basic theory of FEL. We start with the energy exchange equation that describes the interaction between the electrons and radiation. From these deductions, we get the resonant condition and pendulum equation of the FEL. As this thesis is mainly focus on FEL with external seed lasers, equations for harmonic generation schemes include HGHG and EEHG are derived in detail to get the final bunching factor of these schemes.

Keywords Resonant condition • Pendulum equation • Bunching factor

2.1 Energy Exchange Equation

Here we take the planar undulator as an example to introduce the basic theory of FEL. As shown in Fig. 2.1, considering a planar undulator with period of λ_u and a sinusoidal magnetic field in the y direction:

$$B_{\nu}(z) = B_0 \sin(k_{\nu} z) \tag{2.1}$$

where $k_u = 2\pi/\lambda_u$, and the electron motion in the x-z plane can be written as

$$m\gamma \frac{d^2x}{dt^2} = e\left(v_y B_z - v_z B_y\right) = -eB_0 c \sin(k_u z)$$
(2.2)

where m, γ and e is the mass, relativistic energy and charge of an electron, respectively. B_0 is the peak magnetic field of the undulator, c is the speed of light in vacuum, and v_z is the velocity of the electron. When the electron energy is high enough, $v_z \approx c$ and we can change the independent variable from t to z with

$$dt = \frac{dz}{v_z} \approx \frac{dz}{c}.$$
 (2.3)

[©] Springer-Verlag Berlin Heidelberg 2016 C. Feng, *Theoretical and Experimental Studies on Novel High-Gain Seeded Free-Electron Laser Schemes*, Springer Theses, DOI 10.1007/978-3-662-49066-2_2

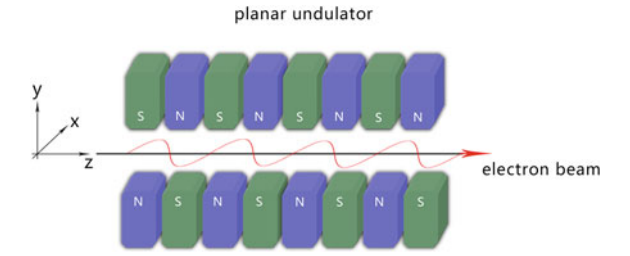


Fig. 2.1 Electron beam trajectory in a planar undulator

And Eq. (2.2) is changed to

$$x'' = -\frac{eB_0}{\gamma mc}\sin(k_u z). \tag{2.4}$$

Integrate Eq. (2.4) along z, we can get

$$x' = \frac{eB_0}{\gamma mck_u} \cos(k_u z) \equiv \frac{K}{\gamma} \cos(k_u z)$$
 (2.5)

where $K = eB_0 / mck_u \approx 0.934B_0 [Tesla] \lambda_u [cm]$ is the undulator parameter. Integrate Eq. (2.5) again, we arrive at

$$x = \frac{K}{\gamma k_u} \sin(k_u z) \tag{2.6}$$

The radiation field generated by the electrons propagates collinearly with the electron beam:

$$\mathbf{E} = \hat{\mathbf{x}}E_0\cos(k_s z - \omega_s t + \theta_0) \tag{2.7}$$

where $\omega_s = ck_s = 2\pi c/\lambda_s$ is the radiation frequency. The electron's transverse velocity induced by the undulator magnet is

$$v_x = \frac{Kc}{\gamma}\cos(k_u z). \tag{2.8}$$

Since the average velocity of the electron is approximately constant

$$\mathbf{v} = c\sqrt{1 - 1/\gamma^2} \tag{2.9}$$

 v_z can be calculated by:

$$v_z = c \left(1 - \frac{1 + K^2/2}{2\gamma^2} \right) - \frac{K^2 c}{4\gamma^2} \cos(2k_u z), \tag{2.10}$$

So the average electron longitudinal velocity is

$$\overline{v}_z = c \left(1 - \frac{1 + K^2/2}{2\gamma^2} \right).$$
 (2.11)

The energy exchange between the electrons and the field should be

$$mc^{2}\frac{d\gamma}{dt} = e\mathbf{E} \cdot v_{x} = \frac{eE_{0}Kc}{\gamma}\cos(k_{u}z)\cos(k_{s}z - \omega_{s}t + \phi)$$

$$= \frac{eE_{0}Kc}{2\gamma}\left\{\cos[(k_{s} - k_{u})z - \omega_{s}t + \phi] + \cos[(k_{s} + k_{u})z - \omega_{s}t + \phi]\right\}$$
(2.12)

The energy will transfer from electrons to radiation field when $e\mathbf{E} \cdot v_x < 0$. When $e\mathbf{E} \cdot v_x > 0$, the energy of the field will be transferred to the electron, which is used for the inverse FEL (iFEL).

2.2 Phase Evolution Equation

From Eq. (2.12), we can get the rate change of the ponderomotive phase θ can be written as

$$\frac{d\theta}{dt} \approx 2k_u c,$$
 (2.13)

where

$$\theta = (k_s + k_u)z - \omega_s t + \phi \tag{2.14}$$

Derivation of Eq. (2.14),

$$\frac{d\theta}{dt} = (k_s + k_u)v_z - ck_s \tag{2.15}$$

Using Eq. (2.11) and $k_u/k_s \ll 1$, we get

$$\frac{d\theta}{dt} = (k_s + k_u)\bar{v}_z - ck_s = ck_s \left(\frac{k_u}{k_s} - \frac{1 + K^2/2}{2\gamma^2}\right)$$
(2.16)

2.3 Resonance Condition and Pendulum Equation

In order to obtain a stationary phase $d\theta/dt = 0$, we need

$$\frac{k_u}{k_s} = \frac{\lambda_s}{\lambda_u} = \frac{1 + K^2/2}{2\gamma^2}$$
 (2.17)

This is the famous resonant condition. For a given resonant energy γ_r , the output wavelength can be written as

$$\lambda_s = \frac{\lambda_u}{2\gamma_r^2} \left(1 + K^2 / 2 \right). \tag{2.18}$$

Here we introduce the normalized electron energy variable parameter

$$\eta = \frac{\gamma - \gamma_r}{\gamma_-} \ll 1,\tag{2.19}$$

and the phase equation is changed to

$$\frac{d\theta}{dt} = 2k_u c\eta \tag{2.20}$$

Equation (2.12) can be written as

$$\frac{d\eta}{dt} = \frac{1}{\gamma_r} \frac{d\gamma}{dt} = -\frac{eE_0 K[JJ]c}{2\gamma \gamma_r mc^2} \sin \theta, \qquad (2.21)$$

where

$$[JJ] = J_0 \left(\frac{K^2}{4 + 2K^2}\right) - J_1 \left(\frac{K^2}{4 + 2K^2}\right). \tag{2.22}$$

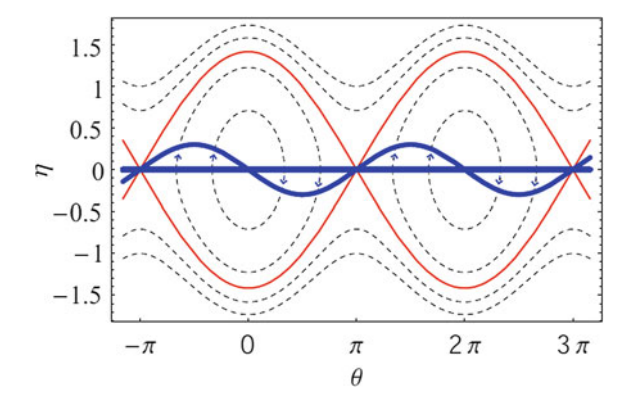
Use $cdt \approx dz$, Eqs. (2.20) and (2.21) can be rewritten as

$$\begin{cases} \frac{d\theta}{dz} = 2k_u \eta \\ \frac{d\eta}{dz} = -\frac{eE_0 K[JJ]}{2\gamma_r^2 mc^2} \sin \theta \end{cases}$$
 (2.23)

From Eq. (2.23) we can get the familiar pendulum equation

$$\frac{d^2\theta}{dz^2} + \Omega_s^2 \sin\theta = 0 \tag{2.24}$$

Fig. 2.2 Electron motion in the longitudinal phase space due to the presence of the radiation field and the undulator



where $\Omega_s^2 = eE_0K[JJ]/2k_umc^2\gamma_r^2$ is the synchrotron rotation frequency. In the low-gain regime, the synchrotron rotation frequency can be considered as a constant. Intergation of Eq. (2.24) and we get

$$\left(\frac{d\theta}{dz}\right)^2/2 - \Omega_s^2 \cos\theta = U = Const \tag{2.25}$$

Figure 2.2 shows the electron's phase space trajectory in the combined system of the radiation field and the undulator. The dashed lines are the phase-space trajectories, and the solid red line is the separatrix, which is the boundary separating trapped and un-trapped trajectories. The region inside the separatrix is called the "bucket". The FEL interaction causes the electrons to gain or lose energy, depending on their ponderomotive phase. Electrons with ponderomotive phase between $[2n\pi, (2n+1)\pi]$ lose energy and move to the bottom of the bucket. Electrons with ponderomotive phase between $[(2n-1)\pi, 2n\pi]$ gain energy and move to the top of the bucket. The resulting energy modulation causes the electrons to develop density modulation with the period of the radiation wavelength.

2.4 Equations for Harmonic Generation Seeded FEL Schemes

As we have mentioned in Chap. 1, harmonic generation schemes with external seed lasers hold the ability to generate stable and fully coherent radiation at short wavelength. In these schemes, the electron beam is manipulated in a nonlinear way to create density modulations at higher harmonics of the seed frequency. Benefit from the coherent density modulation, seeded FEL schemes can be used to increase the stability and temporal coherence over a SASE FEL. In this section, we give the basic theory for both HGHG and EEHG.

2.4.1 HGHG-FEL [1, 2]

The HGHG scheme consists of two undulators separated by a small chicane. In the modulator, the electron beam interacts with a seed laser pulse to generate the energy modulation, which have a maximal value of

$$\Delta \gamma = \frac{k_1 a_1 a_m l_m [JJ]}{\gamma},\tag{2.26}$$

where k_1 is the wave number of the seed laser, l_m is the length of the modulator, a_1 and a_m is the vector potential of the laser and the undulator, respectively. Here we assume an initial Gaussian beam energy distribution with an average energy $\gamma_0 mc^2$ and use the variable $p = (\gamma - \gamma_0)/\sigma_\gamma$ for the dimensionless energy deviation of a particle, where σ_γ is the initial beam energy spread. Thus the initial longitudinal phase space distribution should be written as

$$f_0(p) = \frac{N_0}{\sqrt{2\pi}} \exp\left(-\frac{1}{2}p^2\right),$$
 (2.27)

where N_0 is the number of electrons per unit length of the beam. After passing through the modulator, the electron beam is modulated with amplitude $A = \Delta \gamma / \sigma_{\gamma}$, where $\Delta \gamma$ is the energy modulation depth induced by the seed laser, and the dimensionless energy deviation of the electron beam becomes

$$p' = p + A\sin(k_1 s), \tag{2.28}$$

where s is the longitudinal position. And the longitudinal beam distribution evolves to

$$f_1(\zeta, p) = \frac{N_0}{\sqrt{2\pi}} \exp\left[-\frac{1}{2}(p - A\sin\zeta)^2\right],$$
 (2.29)

After the dispersion section, the energy modulation will be converted into density modulation. The longitudinal position will be changed to

$$s' = s + R_{56}p\sigma_{\gamma}/\gamma \tag{2.30}$$

where R_{56} is the strength of the chicane and p is the beam energy after the energy modulation. The distribution function can be written as

$$f_{HGHG}(\zeta, p) = \frac{N_0}{\sqrt{2\pi}} \exp\left\{-\frac{1}{2}[p - A\sin(\zeta - Bp)]^2\right\},$$
 (2.31)

where $B = R_{56}k_1\sigma_{\gamma}/\gamma$ is the dimensionless strength of the dispersion section. Integration of Eq. (2.31) over p gives the beam density distribution

$$N(\zeta) = \int_{-\infty}^{\infty} dp f_{HGHG}(\zeta, p)$$
 (2.32)

The density modulation of the electron beam can be quantified by the bunching factor, which has a maximum value of unity:

$$b = \frac{1}{N_0} \left| \left\langle e^{-ia\zeta} N(\zeta) \right\rangle \right| \tag{2.33}$$

And the bunching factor at kth harmonic can be written as:

$$b_k = J_k(kAB) \exp\left(-\frac{1}{2}k^2B^2\right)$$
 (2.34)

The bunched electron beam will be sent into the radiator for high harmonic radiation. In the first two gain lengths of the radiator, the FEL works in the coherent harmonic generation regime, where the harmonic field grows linearly with the distance traversed in the radiator z, and the peak power grows as z^2 . So the coherent radiation power after two gain lengths can be written as

$$P_{coh} = \frac{Z_0 I_p^2 K^2 b_k^2 [JJ]^2}{32\pi \Sigma_A \gamma^2} (2L_G)^2$$
 (2.35)

where $Z_0 = 377\Omega$, I_p is the current of the electron beam. After about two gain lengths, the longitudinal dynamic of the electron beam induced by the radiated fields become important, and the radiation power will be exponentially amplified along the radiator until saturation. The saturation power can be estimated by

$$P_{sat} = 1.6\rho \times \left(\frac{L_{G1D}}{L_{G3D}}\right)^2 \frac{\gamma m_e c^2 I_p}{e}, \qquad (2.36)$$

where ρ is the Pierce parameter [3], L_{G1D} and L_{G3D} is the one-dimensional and three-dimensional gain length of the FEL, respectively. From Eqs. (2.35) and (2.36), we get the saturation length of the HGHG-FEL:

$$L_{sat} = L_{G3D} \left[\ln \left(\frac{P_{sat}}{P_{coh}} \right) + 2 \right] \tag{2.37}$$

2.4.2 EEHG-FEL [4, 5]

The EEHG technique employs two pairs of modulator and dispersion section to introduce the echo effect into the electron beam phase space for enhancing the frequency multiplication of the current modulation with a relatively small energy modulation.

After sending the electron beam through the first modulator and dispersion section, the longitudinal beam distribution is similar to Eq. (2.31). Here we assume the energy modulation amplitude induced by the first seed laser is A_1 , and the strength of the first dispersion section is B_1 , then Eq. (2.31) can be rewritten as

$$f_2(\zeta, p) = \frac{N_0}{\sqrt{2\pi}} \exp\left\{-\frac{1}{2} [p - A_1 \sin(\zeta - B_1 p)]^2\right\}$$
 (2.38)

After the second energy modulation, the beam energy is changed to

$$p' = p + A_2 \sin(k_2 s + \varphi) \tag{2.39}$$

where A_2 is the energy modulation amplitude induced by the second seed laser, k_2 is the wave number of the second seed laser and φ is the relative phase of the second seed laser to the first seed laser. After passing through the second dispersive chicane, the longitudinal position of the electrons change to

$$s' = s + R_{56}^{(2)} p \sigma_{\gamma} / \gamma \tag{2.40}$$

where p now refer to the electron energy the entrance to the second dispersion section. The strength of the second dispersion section is $B_2 = R_{56}^{(2)} k_1 \sigma_{\gamma} / \gamma$, and we get the longitudinal phase space distribution at the entrance to the radiator

$$f_{EEHG}(\zeta, p) = \frac{N_0}{\sqrt{2\pi}} \exp\left[-\frac{1}{2} \left\{p - A_2 \sin(K\zeta - KB_2 p + \varphi) - A_1 \sin[\zeta - (B_1 + B_2)p + A_2 B_1 \sin(K\zeta - KB_2 p + \varphi)]\right\}^2\right]$$
(2.41)

where $K = k_2/k_1$. Integration of Eq. (2.41) over p gives the beam density distribution, and the bunching factor can be written as

$$b_{n,m}(\zeta,p) = \left| J_m[-(Km+n)A_2B_2] \right| \times \left| J_n\{-A_1[nB_1 + (Km+n)B_2]\} \exp\left\{ -\frac{1}{2}[nB_1 + (Km+n)B_2]^2 \right\} \right|$$
(2.42)

The up-conversion harmonic number is k = n + Km.

Analysis shows that the nth bunching factor attains its maximum when $n_1 = \pm 1$ and $n_2 = n_3 \cdot n_1$ is chosen to be -1 to make B_1 and B_2 have the same sign. For given A_1 and A_2 , the maximal bunching factor is achieved when $B_2 = \left(n_2 + 0.81n_2^{1/3}\right)/nA_2$ and B_1 is the solution of

$$A_2[J_0(A_1\xi) - J_2(A_1\xi)] = 2\xi J_1(A_1\xi)$$
(2.43)

where $\xi = B_1 - (Km - 1)B_2$. There are infinite number of roots of Eq. (2.43), however, only two roots that have minimal absolute value maximize the expression. The maximal bunching factor of EEHG is

$$b_k \approx \frac{0.39}{(k+1)^{1/3}} \tag{2.44}$$

The FEL gain process in the radiator is similar with that in the HGHG. The saturation power and saturation length of EEHG can also be calculated by Eqs. (2.36) and (2.37).

References

- Yu LH (1991) Generation of intense UV radiation by sub harmonically seeded single-pass free-electron lasers. Phys Rev A 44(8):5178-5193
- Yu LH, Wu J (2002) Theory of high gain harmonic generation: an analytical estimate. Nucl Instrum Methods Phys Res Sect A 483(1):493

 –498
- 3. Bonifacio R, Pellegrini C, Narducci LM (1984) Collective instabilities and high-gain regime in a free electron laser. Opt Commun 50(6):373–378
- Stupakov G (2009) Using the beam-echo effect for generation of short-wavelength radiation. Phys Rev Lett 102(7):074801
- Xiang D, Stupakov G (2009) Echo-enabled harmonic generation free electron laser. Phys Rev Spec Top Accel Beams 12(3):030702

Chapter 3 Theoretical Studies on Novel High-Gain Seeded FEL Schemes

Abstract In this chapter, the technique of manipulating of electron beam phase space at optical wavelength has been systematically studied. After that, several novel high-gain FEL schemes, including the pre-density modulation (PDM), echo-enabled staged harmonic generation (EESHG), phase-merging enhanced harmonic generation (PEHG), mode-locking of seeded FEL, chirped pulse amplification of coherent harmonic generation (CPA-CHG), have been proposed and studied to improve the performance of SASE and HGHG. Theoretical and simulation studies for seeded FEL schemes with ultra-short seed laser pulses are presented to show the phase error multiplication process in harmonic generation schemes. We found that the slippage effect in the modulator can be used to slow down this multiplication process, which may aid in the production of transform-limited short-wavelength pulses for seeded FELs.

Keywords PDM \cdot EESHG \cdot PEHG \cdot Mode-locking \cdot CPA-CHG \cdot Phase error multiplication \cdot Slippage effect

3.1 The Electron Beam Phase Space Manipulation Techinique

Recent advances in the generation and control of high brightness electron beams have lead to a new class of intense accelerator based light sources. With these advances has come tremendous progress in the techniques of beam phase space manipulation in accelerators and high-gain FELs. In linacs, the phase space manipulation technique has been extensively used for bunch compression, emittance exchange, laser heater, bunch measurement, etc. In high-gain FELs, the phase space manipulation is often operated at the optical wavelength scale: a conventional laser pulse is used to interact with an electron beam inside a short magnetic undulator (modulator) to introduce a sinusoidal energy distribution in the longitudinal phase space (energy modulation). After that, a dispersion chicane is often

adopted for introducing a momentum compaction factor to convert the energy modulation into density modulation. This progress can be considered as a bunch compression process at the optical scale. Several distinct combinations of this modulator-chicane arrangement can be used to tailor the electron beam's energy and current distributions and so introduce microbunchings that contain high-harmonic components of the seed. Most of the seeded FEL schemes are based on this laser-manipulation technique.

Here we assume an initial Gaussian beam energy distribution with an average energy $\gamma_0 mc^2$ and use the variable $p=(\gamma-\gamma_0)/\sigma_\gamma$ for the dimensionless energy deviation of a particle, where σ_γ is the rms energy spread. So the initial longitudinal phase space distribution should be $f_0(p)=N_0\exp(-p^2/2)/\sqrt{2\pi}$, after n successive modulator and chicane pairs, the energy distribution along the longitudinal direction is changed to

$$p_n = p_{n-1} + A_n \sin(k_n s_{n-1} + \varphi_n), \tag{3.1}$$

where k_n and φ_n is the wave number and phase of the nth seed laser. $A_n = E_n/\sigma_E$ is the scaled energy modulation amplitude induced by the seed laser. The corresponding longitudinal coordinate transformations can be written as

$$s_n = s_{n-1} + B_n p_n / k_1, (3.2)$$

where $B_n = R_{56}^{(n)} k_1 \sigma_E / E_0$ is the dimensionless dispersion strength of the *n*th chicane. $R_{56}^{(n)}$ is the momentum compaction of the *n*th chicane. The density modulation of the electron beam can be measured by the bunching factor, which has a maximum value of unity. The initial bunching factor at *k*th harmonic of the seed is given by

$$b_k = \left\langle \int e^{-iks_n} f_f(s_n, p_n) dp_n \right\rangle \tag{3.3}$$

where $f_f(s_n, p_n)$ is the density distribution of the electron beam. Equations (3.1)–(3.3) can be used to perform simple one-dimensional phase space (p–z) simulations and help us to understand the phase space manipulation processes in various harmonic generation schemes.

Figure 3.1 shows the phase space and corresponding bunching factor distributions of a single stage HGHG with $A_1 = 6$ and $B_1 = 0.2$. As we mentioned above, the frequency multiplication efficiency of a single stage HGHG is limited to a small number (~ 10) for a single stage HGHG. Significant bunching at higher harmonics by strengthening the energy modulation would increase the energy spread of the electron beam [1], as shown in Fig. 3.2, which would result in a degradation of the amplification process in the final radiator.

In order to improve the frequency multiplication efficiency in a single stage, more complicated phase space manipulation techniques that employ

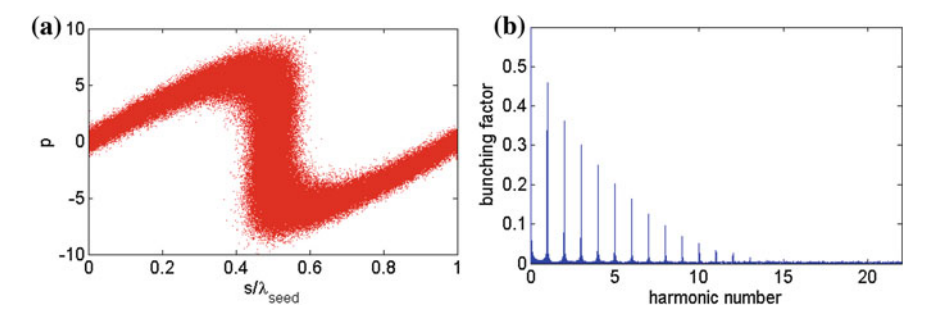


Fig. 3.1 The final phase space a and bunching factor b distributions of the HGHG

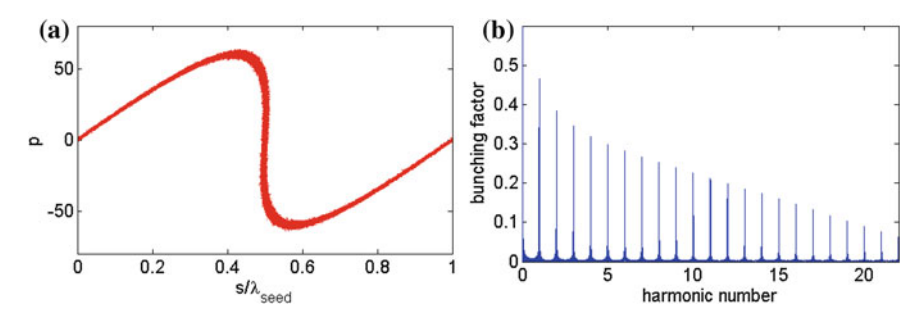


Fig. 3.2 The final phase space a and bunching factor b distribution of the HGHG with very large energy modulation amplitude

double-modulator or even trible modulator configurations have been developed. The first double-modulator scheme, termed Slience scheme, is proposed in Refs. [2, 3], where a second modulator is directly added after the first modulator to suppress the laser induced energy spread. In the first modulator, the electron beam obtains a large energy modulation by a seeding laser with large power. Meanwhile, the bunching of fundamental and higher harmonics develops greatly due to its large energy spread in this section. Then the electron beam experiences a π phase shift and enters the second modulator, in which it interacts with another seeding laser whose phase is the same as that in the first modulator and thus is π different from that of the current electron beam. Therefore, the electron beam's energy spread will be effectively suppressed, while its bunching will still increase due to the existing energy spread. Finally, it passes a dispersion section which induces a larger bunching factor, as shown in Fig. 3.3.

A modified version of the Slience scheme, termed enhanced-HGHG (EHGHG), was proposed in Ref. [4]. In this scheme, after passing through the first modulator, the electron beam is compressed by a dispersion section and then passes a so-called de-modulator. By fine tuning the strength of the dispersion section to introduce a relative π phase shift between the seed laser and the electron beam in the second modulator, the laser-induced energy spread can be compressed. In the mean time,

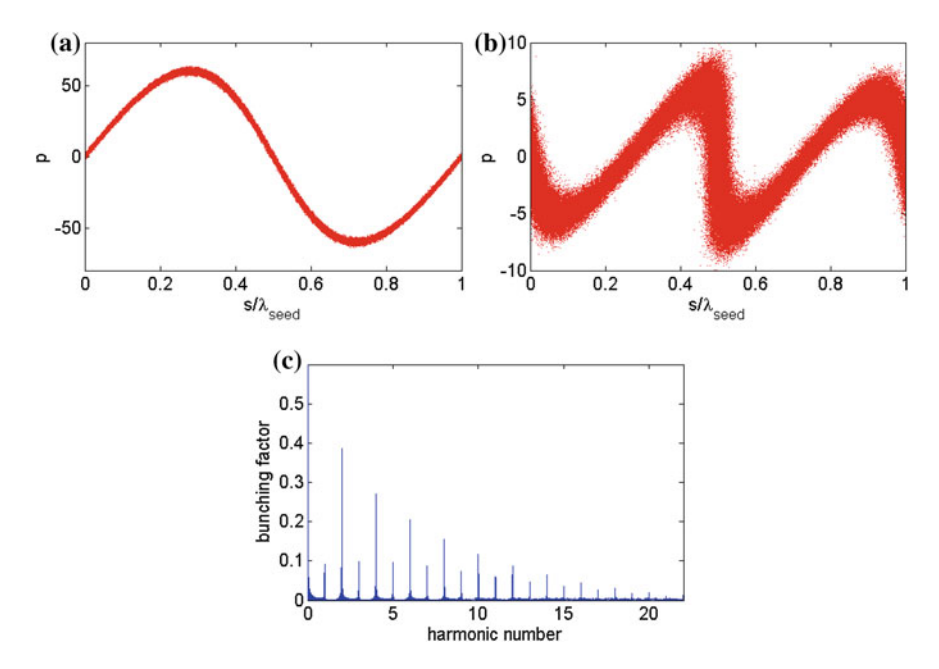


Fig. 3.3 Longitudinal phase space evolution in the Slience scheme. **a** Phase space at the exit of the first modulator. **b** Phase space at the exit of the dispersion chicane. **c** Bunching factor at the exit of the dispersion chicane

the formed bunching would not be degraded as the micro-bunching is located around the zero-phase of the seed laser in the two modulators. The advantage of EHGHG to the Slience scheme is that the bunching enhancement is manly realized in the dispersion section, so it doesn't require a very high power seed laser. The phase space evolution of the electron beam in the EHGHG is shown in Fig. 3.4a, b. Figure 3.4c gives the corresponding bunching factor distribution at the entrance to the radiator.

The common character of the phase space evolution processes in Figs. 3.2, 3.3 and 3.4 is the electron beam stretchen in the longitudinal phase space. By stretching the electron beam with a very powerful laser pulse, the final coherent micro-bunching can be further compressed in the longitudinal direction. As a result, the harmonic up-conversion efficiency will be enhanced. An alternative method for stretching the electron beam in the longitudinal phase space is increasing the strength of the dispersion section, which is also the key point for understanding the physical mechanism of the EEHG. In the standard EEHG scheme, the electron beam is first energy modulated by a seed laser in the first modulator and then sent through a chicane with strong momentum compaction, which makes the energy modulation macroscopically smeared out, but in the phase space of the electron beam, many small pieces along the longitudinal direction appear (Fig. 3.5a). The electron beam with this energy bands structure will be modulated again in the

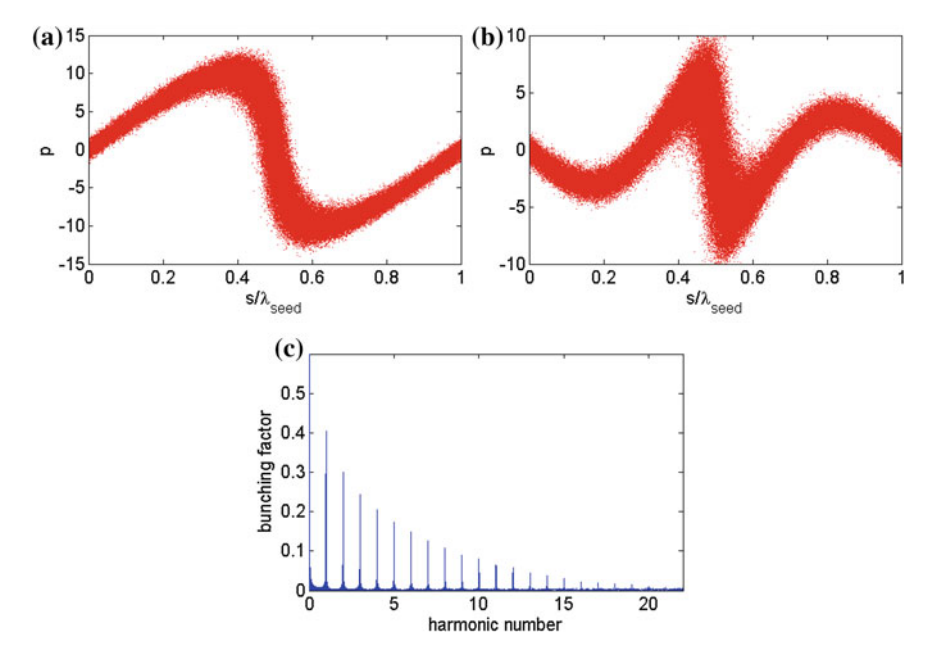


Fig. 3.4 Longitudinal phase space evolution in the EHGHG scheme. **a** Phase space at the exit of the dispersion section. **b** Phase space at the exit of the second modulator. **c** Bunching factor at the exit of the second modulator

second modulator by another laser beam. After passing through the second chicane, the separated energy bands will be converted into the separated current bands (Fig. 3.5b) which can introduce a maximal bunching factor at very high harmonics (Fig. 3.5c) of the seed.

The bunching factor of EEHG can be written as

$$b_k = \left| \sum_{n=-\infty}^{\infty} J_{-n-k} \{ -A_1[(n+k)B_1 + kB_2] J_n[kA_2B_2] \} e^{-1/2[(n+k)B_1 + kB_2]^2} \right|.$$
 (3.4)

Analysis shows that the bunching factor is mainly decided by $n = \pm 1$, and Eq. (3.4) can be expressed as

$$b_{k} = \left| J_{k+1} \{ A_{1}[(k+1)B_{1} + kB_{2}] J_{1}[kA_{2}B_{2}] \} e^{-1/2[(k+1)B_{1} + kB_{2}]^{2}} - J_{k-1} \{ A_{1}[(k-1)B_{1} + kB_{2}] J_{1}[kA_{2}B_{2}] \} e^{-1/2[(k+1)B_{1} + kB_{2}]^{2}} \right|$$
(3.5)

In order to make the two dispersion chicanes have the same sign, n = -1 is often adopted. However, we found n = 1 will lead to a larger maximal bunching factor. Here we choose n = 1 and $B_2 = -B_1$, then Eq. (3.5) can be simplified as:

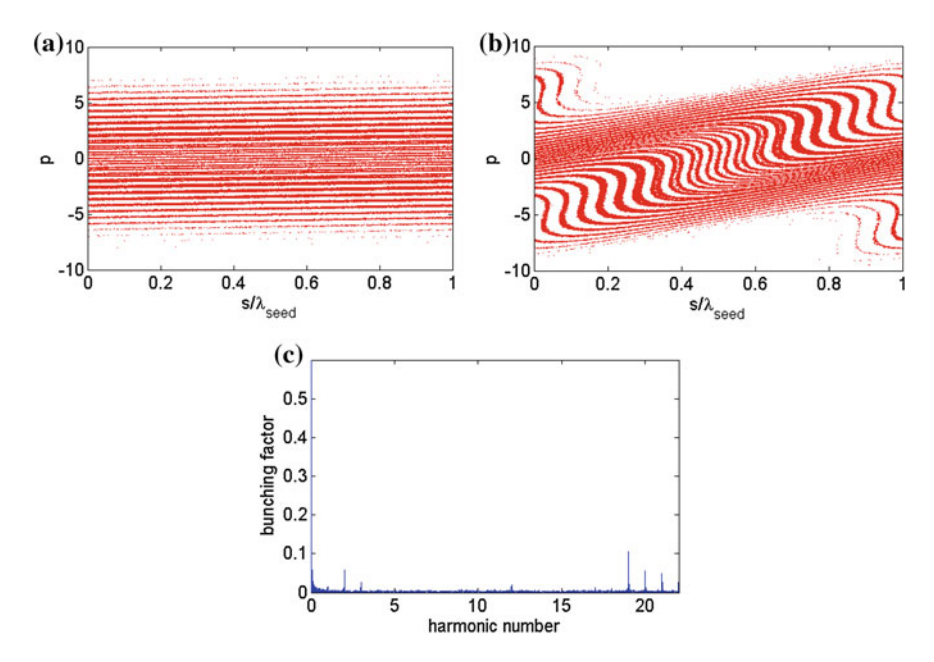


Fig. 3.5 Longitudinal phase space evolution in the EEHG scheme. **a** Phase space at the exit of the first dispersion section. **b** Phase space at the exit of the second dispersion section. **c** Bunching factor at the exit of the second dispersion section

$$b_k = \left| \frac{2k}{A_1 B_1} J_k [A_1 B_1] J_1 [k A_2 B_1] e^{-B_1^2/2} \right|$$
 (3.6)

For k > 4, the maximal value of $2kJ_k[A_1B_1]/A_1B_1$ will approach $1.33/k^{1/3}$ when $A_1B_1 \approx k + 0.81k^{1/3}$. The maximal value of $J_1[kA_2B_1]e^{-B_1^2/2}$ is about 0.58. So the maximal bunching factor will approach

$$b_k \approx \frac{0.77}{k^{1/3}},$$
 (3.7)

which is nearly 2 times larger than the bunching factor of a standard EEHG for the same harmonic number. However, a very large A_1 is required in this case to make the bunching factor reach its maximal value. To suppress the large energy spread induced by the first seed laser, a third modulator should be added. The phase space evolution of this triple-modulator scheme is shown in Fig. 3.6.

In the first modulator, a very large energy modulation amplitude is induced by the seed laser ($A_1 = 40$). For this large energy modulation, a small dispersion strength ($B_1 = 0.56$) is sufficient for converting the energy modulation into energy bands, as shown in Fig. 3.6a. As the energy spread for each energy band is very small, we only need a very weak seed laser to generate energy modulation

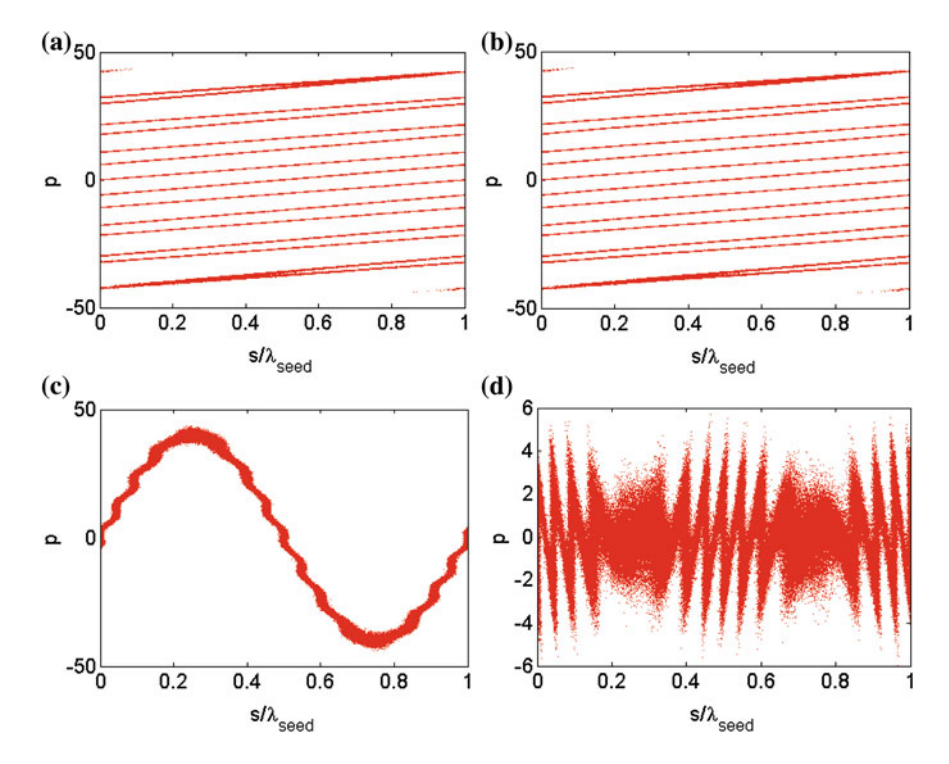


Fig. 3.6 Longitudinal phase space evolution in the triple-modulator scheme. **a** Phase space at the exit of the first dispersion section. **b** Phase space at the exit of the second modulator. **c** Phase space at the exit of the second dispersion section. **d** Phase space at the exit of the third modulator

amplitude of $A_2=0.15$ in the second modulator (Fig. 3.6b). Because the energy modulation amplitude is much smaller than the beam's initial energy spread, it is difficult to see the difference in Fig. 3.6a, b. After passing through the second dispersion section with strength of $B_2=-0.56$, the resulting phase space is shown in Fig. 3.6c. In the third modulator, a seed laser with π phase shift is used to suppress the energy spread, and the final phase space is shown in Fig. 3.6d. The corresponding bunching factor at various harmonics is shown in Fig. 3.7, where one can find that the bunching factor at 20th harmonic is much larger than a standard EEHG and the laser induced energy spread in Fig. 3.6d is much smaller than the initial beam energy spread.

To generation sufficient bunching factor at ultra-high harmonics via the triple-modulator scheme, one needs to introduce a very large A_1 , which will be very challenging. This problem can be fixed by using the triple modulator-chicane scheme (TMC) [5], which adopt three modulator-chicane modules to manipulate the electron beam phase space. The phase space evolution in the TMC with $A_1 = A_3 = 5, A_2 = 0.05, B_1 = -B_2 = 4.7, B_3 = 0.176$ is shown in Fig. 3.8. The phase space evolution before the third chicane is similar with the triple-modulator scheme,

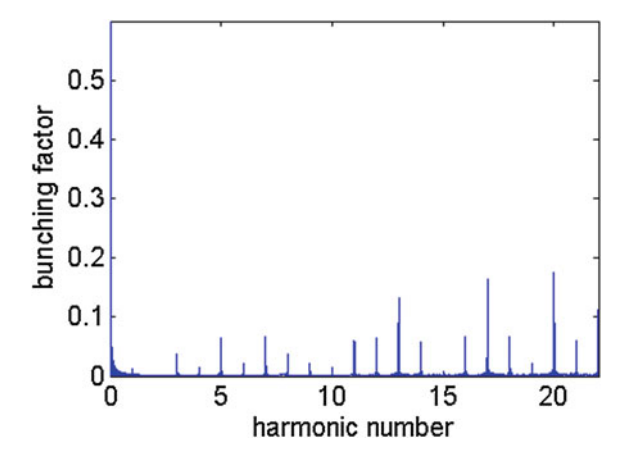


Fig. 3.7 Bunching factor distribution of the trible-modulator scheme

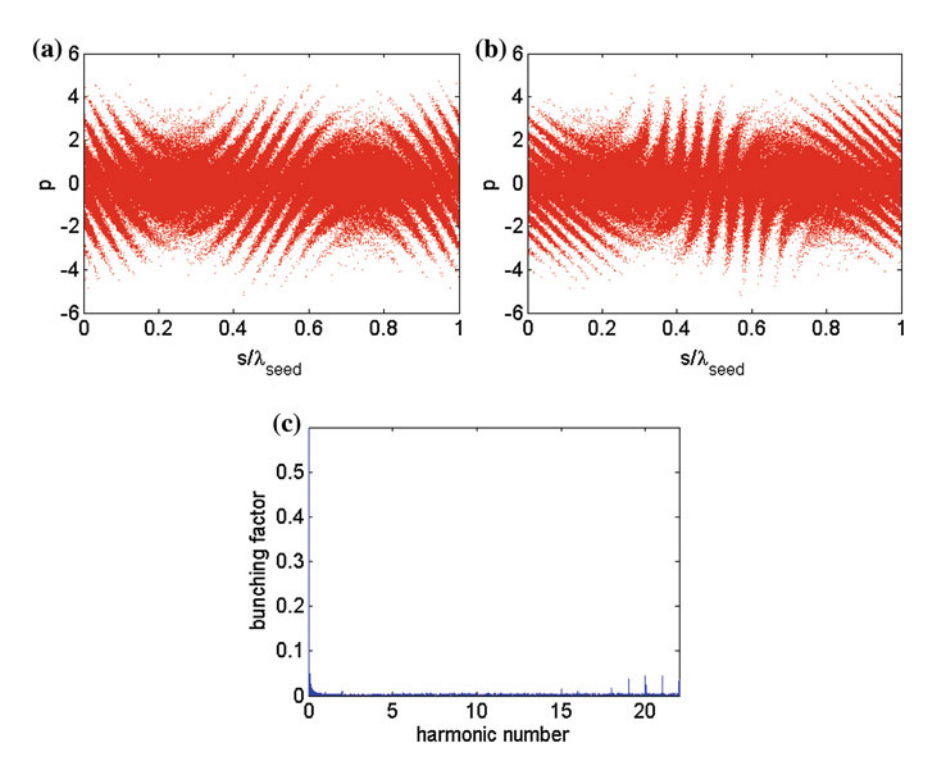


Fig. 3.8 Longitudinal phase space evolution in the TMC. **a** Phase space at the exit of the third modulator. **b** Phase space at the exit of the third dispersion section. **c** Bunching factor at the exit of the third dispersion section

however, the coherent micro-bunching is still not formed before the third modulator due to the small energy modulation amplitudes in the three modulators. As a result, a third chicane is needed to convert the energy modulation into density modulation. The maximal bunching factor of TMC is a little smaller than that of a standard EEHG. The unique advantages of TMC is that only a small energy modulation is needed in the second modulator, which opens new opportunities for using an HHG source to seed x-ray FELs with final radiation wavelength at sub-nanometer level.

The laser based electron beam manipulation technique allows one to rearrange the particle distribution in the phase space to meet the requirement of various applications. With this technique, one can create micro-structures and imprint micro-correlations in relativistic electron beams with extremely high precision in both the temporal and spatial domain, thereby offering numerous options to tailor the properties of the FEL output. Hereafter, we will propose numbers of new seeded FEL schemes. All of these new schemes are based on the laser-associate electron beam manipulation technique.

3.2 Pre-density Modulation of the Electron Beam for Enhancing Seeded FELs

In order to further enhance the harmonic up-conversion efficiency and also reduce the additional energy spread of harmonic generation schemes, here we propose the pre-density modulation (PDM) method. The schematic of the PDM enhanced HGHG and EEHG schemes are shown in Fig. 3.9. The PDM is consists of one short undulator and one chicane, which are similar to the modulator and dispersion section in a standard HGHG. Figure 3.10 shows the physics processes of PDM. The electron beam is first energy modulated through a very short undulator by a seed laser (Fig. 3.10b). Then a small chicane is used for over-bunching of the electron

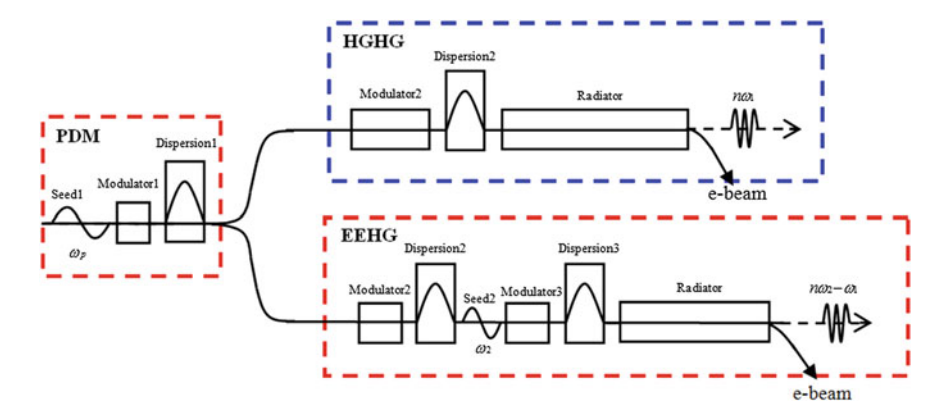


Fig. 3.9 Schematic of the PDM enhanced HGHG and EEHG

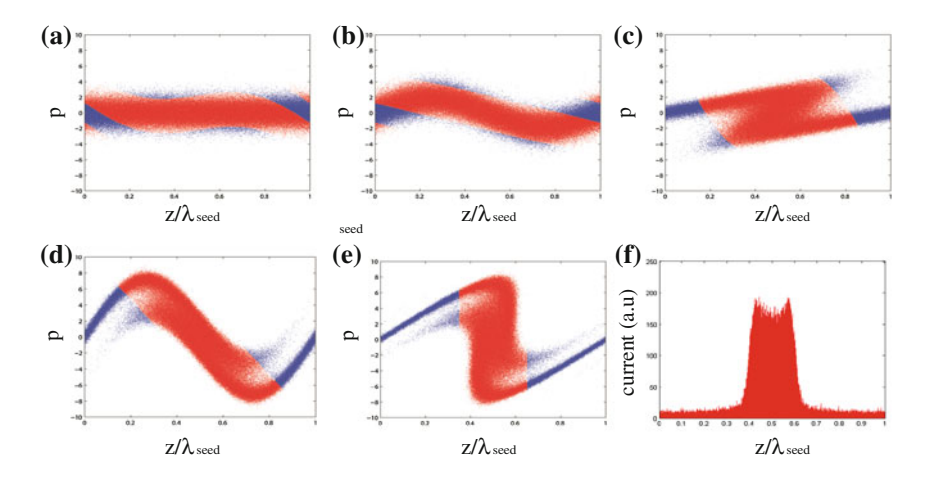


Fig. 3.10 Longitudinal phase space evolution in the PDM enhanced HGHG scheme, the red electrons make a contribution to the microbunching. **a** Phase space at the entrance to modulator; **b** Phase space after the undulator in PDM; **c** Phase space at the exist of PDM; **d** Phase space at the exist of modulator in HGHG; **e** Phase space at the exist of dispersion in HGHG. **f** Current distribution at the entrance to the radiator

beam like Fig. 3.10c shows. This overbunching is aiming at gathering most of the electronics in the phase range of $-\pi/2$ to $\pi/2$ of the fundamental optical field. Then this pre-density modulated beam can be send into HGHG or EEHG. Since the microbunching is already formed after PDM, intense coherent radiation at the seed wavelength will be generated in the following modulator, and the electron beam will be modulated by its own radiation, as shown in Fig. 3.10d. Sending then the beam through the dispersion section will convert this structure into a very strong microbunching at the fundamental wavelength as Fig. 3.10e shows. The current distribution of Fig. 3.10e is shown in Fig. 3.10f.

The laser induced electron beam energy spread in the PDM enhanced HGHG is smaller than that of a standard HGHG with the same energy modulation amplitude. Figure 3.11 shows the comparison of the energy distributions of the electron beam from these two schemes. The comparison of the bunching distributions are given in Fig. 3.12. For HGHG, the high harmonic bunching factor exponentially decreases as the harmonic number increases. However, for the PDM enhanced HGHG, the bunching factor at fundamental is over 0.7, and bunching factors at some high harmonics are also enhanced.

PDM can also be used to enhance the bunching factor of an EEHG. One feature of EEHG is that there are always two maximum bunching factors around the target radiation wavelength. To show the physical mechanism behind this, we carried out one dimensional simulations with optimized parameters that maximize the bunching factor at 30th harmonic. The longitudinal phase space at the entrance to the radiator is shown in Fig. 3.13a and the corresponding bunching factors at various harmonic numbers are shown in Fig. 3.13b. It is clear that besides the 30th

Fig. 3.11 Comparison of electron energy distribution at the entrance to the radiator of HGHG (*blue*) and PDM enhanced HGHG (*red*)

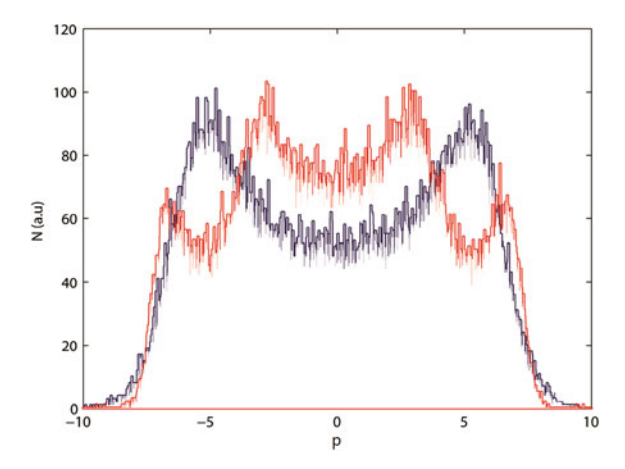
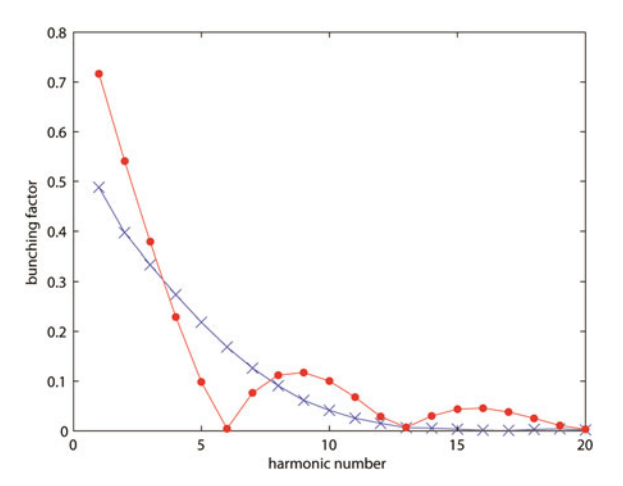


Fig. 3.12 Comparison of the bunching factors of HGHG (*blue*) and PDM enhanced HGHG (*red*)



harmonic, another maximum bunching factor at 32nd harmonic appears. The complicated echo structure in one wavelength region (Fig. 3.13a) can be divided into two uniform bunching structures as shown in Fig. 3.13c, d. We found that there are 30 beamlets in Fig. 3.13c and 32 beamlets in Fig. 3.13d, which indicate a presence of the 30th and 32nd harmonics of the seed laser.

The PDM can be used to enhance the bunching factor of EEHG at the target harmonic. Figure 3.14a shows the longitudinal phase space of the PDM enhanced EEHG. The corresponding bunching factors is given in Fig. 3.14b. We find that there is only one maximum value at the target wavelength, and the 62nd harmonic is also enhanced which can be used to significantly extend the short-wavelength range of the EEHG scheme.

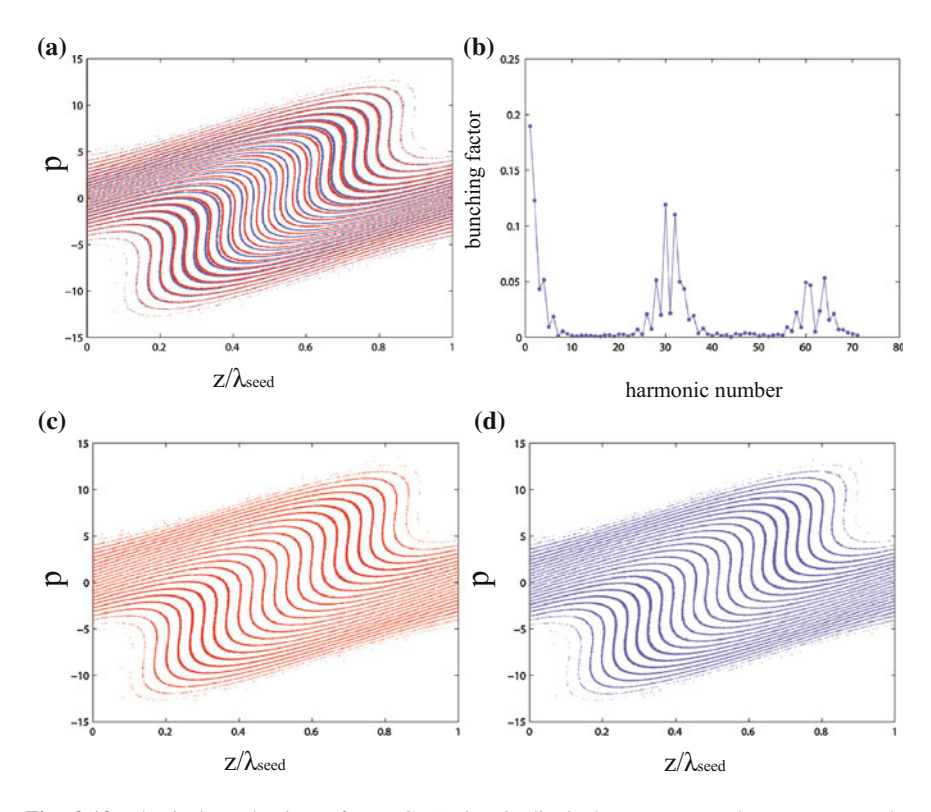


Fig. 3.13 Physical mechanism of EEHG (a) longitudinal phase space at the entrance to the radiator, which is mixed with the red part (c) and the blue part (d); b bunching factor versus harmonic numbers of the seed laser

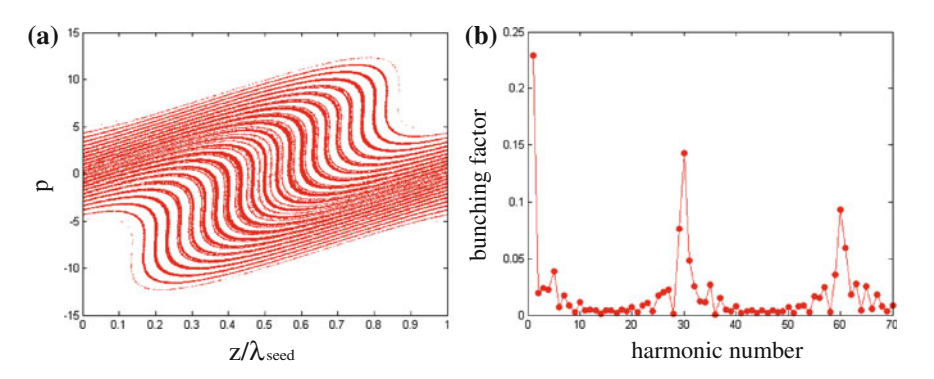


Fig. 3.14 Enhance the bunching factor of EEHG by a PDM a longitudinal phase space at the entrance to the radiator; b bunching factor versus harmonic numbers of the seed laser

3.3 The Echo-Enabled Staged Harmonic Generation

Although the EEHG scheme has a remarkable up frequency conversion efficiency, it is still very difficult to use a single stage EEHG to generate hard x-ray radiation directly from a VUV seed laser. If borrowing the idea from cascaded HGHG to make a cascaded EEHG, as shown in Fig. 3.15a, how to transport the radiation from the first stage to the two modulators in the second stage might become extremely complicated and a great challenge. To mitigate this problem, we propose the Echo-enabled Staged Harmonic Generation for coherent hard x-ray FEL generation. Figure 3.15b shows the schematic setup of EESHG scheme, which consists of an EEHG, a beam shifter and an HGHG like configuration, but the HGHG part is equivalent to an EEHG by jointly using the first modulator and first dispersion section with the EEHG part.

The evolving process of the longitudinal phase space in the first stage of EESHG is shown in Fig. 3.16. The M1 and the DS1 help to obtain separate energy bands all over the whole electron beam (Fig. 3.16a). In the M2, the seed laser 2 is adjusted so that only the tail half part of the electron beam is energy modulated (Fig. 3.16b), then this beam is sent through the DS2 which converts the energy modulated part into a density modulation (Fig. 3.16c), where the head part, called "fresh" part hereafter, is also pulled with an additionally small strength and makes the spacing between the adjacent energy bands more narrow. The radiation from the R1, which uses the EEHG pre-bunched tail part, serves as the seed laser of the second stage. The shifter between these two stages is so tuned that the fresh part of the e-beam can exactly interact with the seed laser 3 in M3. Noticing that the fresh part has

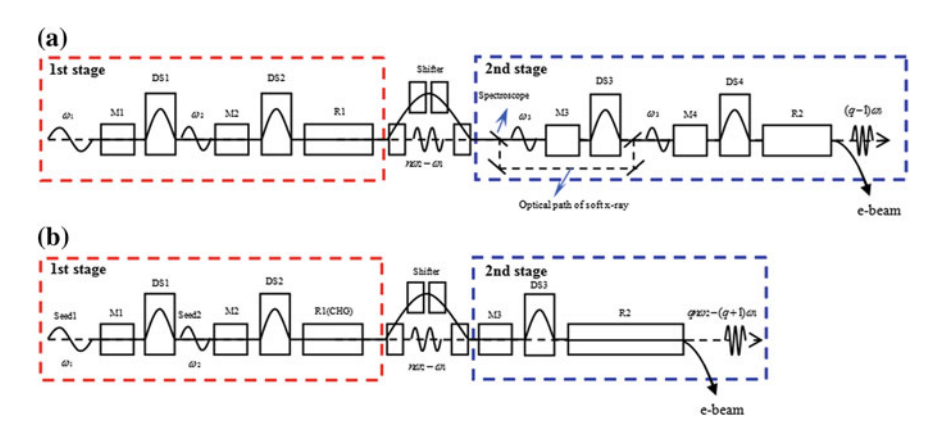


Fig. 3.15 a Using usual method to cascade two stages of EEHG scheme. **b** EESHG scheme. The first stage is an EEHG and the second stage is an HGHG like configuration, which also works in EEHG principle. (Reprint from Ref. [6]. Copyright with kind permission from Springer Science + Business Media)

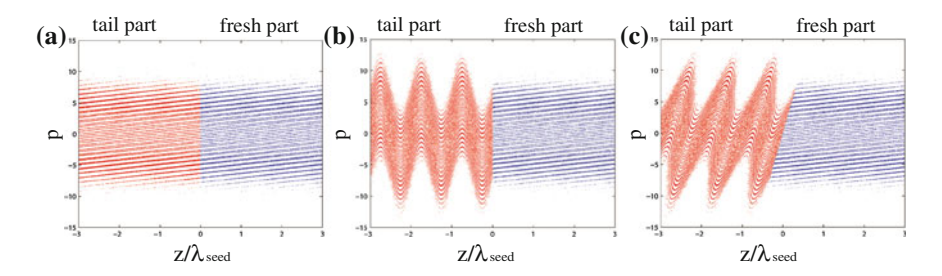


Fig. 3.16 Sketch map of longitudinal phase space in the first stage of EESHG. a Phase space after the DS1. b Phase space after the M2. c Phase space after the DS2

already been modulated and shredded to energy beamlets in the first stage, for the fresh part, the second stage together with the M1 and DS1 can also be considered as a whole EEHG. In this way, the output from the R2, which is tuned at the harmonic of the seed laser 3, can be extended to even hard x-ray region. In addition, since the needed seed laser power for the second stage is much smaller than the saturation power of the first stage, the length of the R1 is so chosen to make it work in the coherent harmonic generation (CHG) [7, 8] regime, which reduces not only the machine size but also its impact on the fresh part.

3.3.1 Analytical Calculations

The first stage of EESHG is a usual EEHG scheme, which is already studied in detail. Here we only pay attention to the fresh part of the e-beam.

The distribution function of the electron beam after DS2 can be written as

$$f_2(\zeta, p) = \frac{N_0}{\sqrt{2\pi}} \exp\left\{-\frac{1}{2} [p - A_1 \sin(\zeta - B_1 p)]^2\right\}.$$
(3.8)

When the fresh part passing through the DS2 and the beam shifter, the longitudinal phase follows

$$z'' = z + R_{56(c)} p\sigma_E / E_0 (3.9)$$

where $R_{56(c)} = R_{56}^{(1)} + R_{56}^{(2)} + R_{56}^{(s)}$ and $R_{56}^{(s)}$ is the strength of the beam shifter. In the second stage, with the dimensionless amplitude A_3 , the wave number of the seed laser k_3 and the dispersive strength of DS3 $R_{56(3)}$, one can write

 $p^{'}=p+A_{3}\sin(k_{3}z)$ and $z^{'}=z+R_{56(3)}p\sigma_{E}/E_{0}$, so the final distribution function of the fresh part after the DS3 is

$$f_{EESHG}(\zeta, p) = \frac{N_0}{\sqrt{2\pi}} \exp\left[-\frac{1}{2} \left\{ p - A_3 \sin(K'\zeta - K'B_3p + \phi') - A_1 \sin[\zeta - (B_c + B_3)p + A_3B_c \sin(K'\zeta - K'B_3p + \phi')] \right\}^2\right]$$
(3.10)

where $B_3 = R_{56(3)}k1\sigma_E/E_0$, $B_c = R_{56(c)}k_1\sigma_E/E_0$, $K_c = k_3/k_1$, and ϕ' is the phase of the seed laser 3. The bunching factor at the entrance to the R2 can be written as

$$b_{n,q} = \left| e^{-1/2[nB_c + (K'q + n)B_3]^2} J_q[-(K'q + n)A_3B_3] J_n\{-A_1[nB_c + (K'q + n)B_3]\} \right|$$
(3.11)

where n and q are integer numbers. we limit our considerations to the n=-1, m>0 and q>0 condition, where m is also an integer number related to the bunching factor of the first stage. A_1,A_2,B_1,B_2 and B_c are determined in the first stage. When we maximum the bunching factor of the second stage, we have to change A_3 and B_3 to maximize $b_{n,q}$. B_3 should be optimized by $B_3=(B_c-\xi)/(K_cq-1)$ first, where $\xi=B_1-(Km-1)B_2$, and A_3 can be optimized by $A_3=(q+0.81q^{1/3})/(K_cqB_3-B_3)$, after doing this, the beam modulation is observed at the frequency $\omega_c=q\omega_3-\omega_1$. When m>4, the maximal bunching factor is

$$|b_{-1,q}| \approx \frac{0.67}{(q+1)^{1/3}} J_1(A_1 \xi) e^{-\xi^2/2}$$
 (3.12)

Generally q is a big number, in our scheme $\omega_3 \gg \omega_1$, so the output frequency $\omega_c = q\omega_3 - \omega_1$ is nearly only determined by ω_3 , since $\omega_3 = m\omega_2 - \omega_1$, and the final output frequency can be written as

$$\omega_c = qm\omega_2 - (q+1)\omega_1 \tag{3.13}$$

If we assume the frequency of the seed laser 1 and seed laser 2 equal, $\omega_1 = \omega_2$, then the output frequency satisfies

$$\omega_c = (qm - q - 1)\omega_1 \tag{3.14}$$

which means the final output frequency should be qm - q - 1 times of the initial one.

	emittance 0.8						
		SASE	EESHG				
			First stage			Second stage	
			Modulator 1	Modulator 2	Radiator	Modulator	Radiator
Seed laser	Power/MW	/	185	3700	1	240	/
	λ_s /nm	1	160	160	7	2	
Undulator	λ _u /cm	1.5	20	20	10	4	1.5
	$a_{\rm u}$	0.93	15.153	15.153	2.178	3.66	0.959
	L_u /m	100	2	2	6	2	40
	Total length/m	100	52				
Dispersion	R ₅₆ /mm	/	4.46	0.05	1	0.0025	/
FEL	λ/nm	0.1	2			0.1	
	Pout/GW	2	0.36			1.2	
	Harmonic number	/	80 20			20	
Shifter	R ₅₆ /mm	/	0.03				

Table 3.1 Comparison of the optimized parameters with SASE and EESHG

Electron beam: Energy 6.135 GeV, Current 3000 A, Slice energy spread 4×10^{-5}

Reprint from Ref. [6]. Copyright with kind permission from Springer Science + Business Media

Hard X-Ray FEL Based on the EESHG Scheme

To explore the performance of the EESHG scheme with realistic parameters, we design a hard x-ray FEL. The optimization is conducted using GENESIS [9] and the simulation parameters are summarized in Table 3.1.

The wavelength of VUV seed laser 160 nm with the frequency of seed laser 1 and seed laser 2 equal is considered to get 0.1 nm radiation with a saturation power around 1.2 GW using EESHG. Since we don't pursue a very high saturation power in the first stage, a relatively large energy modulation, which will substantially improve the harmonic number of the first stage, is introduced in the M2. We choose the power of seed laser 2 about 3.7 GW, which makes the dimensionless amplitude $A_2 = 13$, and the maximum bunching factor is about 0.08 at 80th harmonic. The longitudinal phase space after the DS2 is shown in Fig. 3.17a, from which one can find that the energy spread is much bigger than the initial value. Figure 3.17b plots the radiation power along R1. The output power is over 360 MW, which is sufficient as a seed laser for the second stage. Since the performance of the second stage may be degraded by the impact on the fresh part from the first stage, to make the bunching factor big enough, we only choose to optimize the 20th harmonic for the second stage, and thus the total harmonic number is 1600. The longitudinal phase space after the DS3 is shown in Fig. 3.17c. Figure 3.17d illustrates the radiation power along R2. The bunching factor of the 20th harmonic of the seed laser 2 is

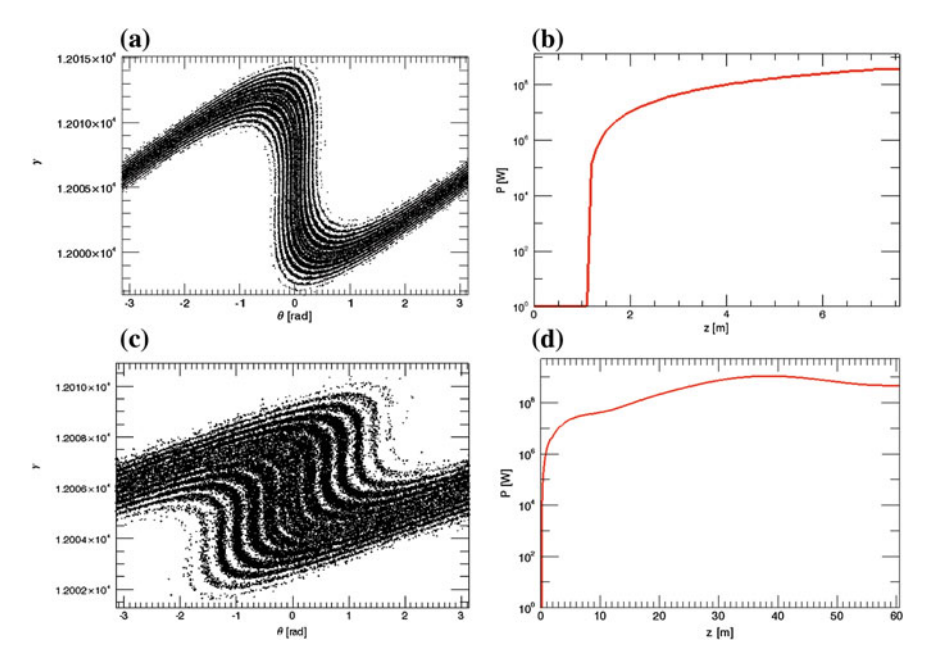


Fig. 3.17 a Longitudinal phase space at the entrance to the R1. **b** Radiation power vs R1 distance for the first stage. **c** Longitudinal phase space at the entrance to the R2. **d** Radiation power versus R2 distance for the second stage. (Reprint from Ref. [6]. Copyright with kind permission from Springer Science + Business Media)

about 0.1 at the entrance to the R2 and the saturation length is about 36 m, which is much shorter in comparison with the SASE case. It is therefore the EESHG scheme holds the great potential to remarkably further reduce size and cost of a compact hard x-ray FEL facility.

3.4 Phase-Merging Enhanced Harmonic Generation

While EEHG has unprecedented up-frequency conversion efficiency and allows the generation of ultrahigh harmonic with relatively small energy modulation, its configuration is more complex when compared with HGHG, and the CSR, ISR effects induced by the large chicane may smear out the fine structure in the phase space. Recently, the idea of using a transverse gradient undulator (TGU) to mitigate the effects of electron beam energy spread in laser-plasma driven FELs has been described [10]. Inspired by this work, a novel phase space manipulation technique, originally termed cooled-HGHG, has been proposed for significantly improving the frequency up-conversion efficiency of a single stage HGHG [11]. This technique benefits from the transverse-longitudinal phase space coupling, while other harmonic generation schemes only manipulate the longitudinal phase space of the

electron beam. Different form the original idea of using TGU to compensate the effects of beam energy spread by making every electron satisfies the resonant condition in the undulator, this novel scheme utilizes a different operating regime of the TGU: when the transversely dispersed electrons pass through the TGU modulator, around the zero-crossing of the seed laser, the electrons with the same energy will merge into a same longitudinal phase, which holds great promise for generating fully coherent short-wavelength radiation at very high harmonics of the seed.

At the first glance, this phase-merging phenomenon is very similar with the electron beam energy spread cooling. However, the beam energy spread within the range less than seed laser wavelength is reduced, while the global beam energy spread does not change in such a process. Therefore, in order to clearly and unanimously illustrate the physics behind it, we rename such a scheme as phase-merging enhanced harmonic generation (PEHG). In this section, systematical studies for the PEHG together with its variants will be presented.

3.4.1 Principles of PEHG

The initial proposed PEHG consists of a dogleg followed by a HGHG configuration with a TGU modulator, as shown in Fig. 3.18a. The dogleg with dispersion η is used to transversely disperse the electron beam, while the TGU modulator is used for the energy modulation and precisely manipulating the electrons in the horizontal dimensional. It is found that these two functions of TGU modulator can be separately performed by employing the scheme II as shown in Fig. 3.18b. A normal modulator is used for the energy modulation and the TGU is only used for transverse manipulation of electrons, which will be much more flexible for practical operation. The TGU in scheme II also can be replaced by other kinds of devices

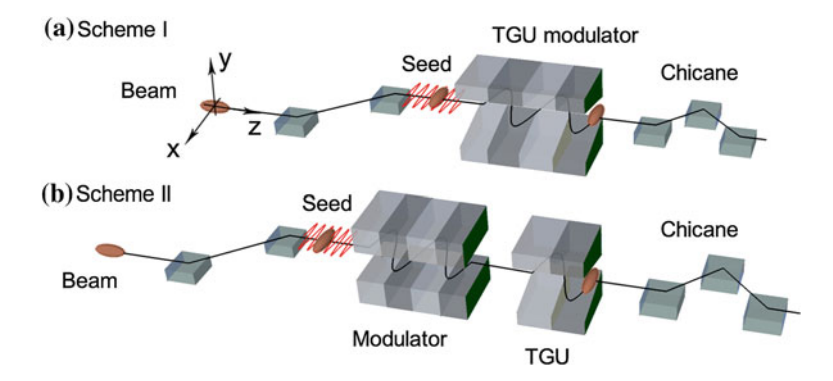


Fig. 3.18 a Original PEHG scheme with a TGU modulator for energy modulation and phase-merging simultaneously; **b** An PEHG variant with a normal modulator for energy modulation and a TGU for introducing the phase-merging effect. (Reprint from Ref. [12]. Copyright with kind permission from IOPscience)

with transverse gradient magnet field, e.g. particularly designed wigglers or small chicanes. For the convenience of theoretical analysis, we consider the scheme II first, and then promote the conclusions to scheme I.

Here we also assume an initial Gaussian beam energy distribution. Assuming the initial horizontal rms beam size is σ_x and use $\chi = (x - x_0)/\sigma_x$ for the dimensionless horizontal position of a particle, where x_0 is the central beam position in the horizontal direction. Then the horizontal electron beam distribution can be written as $g_0(\chi) = N_0 \exp(-\chi^2/2)/\sqrt{2\pi}$. After the dogleg, χ is changed to

$$\chi' = \chi + Dp, \tag{3.15}$$

where $D = \eta \sigma_{\gamma} / \sigma_{x} \gamma$ is the dimensionless strength of the dogleg, and the horizontal beam distribution becomes

$$g_1(p,\chi) = \frac{N_0}{\sqrt{2\pi}} \exp\left[-\frac{1}{2}(\chi - Dp)^2\right],$$
 (3.16)

After passage through the modulator, the electron beam is modulated with the amplitude A, and the dimensionless energy deviation of the electron beam becomes $p' = p + A \sin(k_s z)$, where k_s is the wave number of the seed laser. The two-dimensional distribution function after the interaction with the seed laser can be written as

$$h_1(\zeta, p, \chi) = \frac{N_0}{2\pi} \exp\left[-\frac{1}{2}(p - A\sin\zeta)^2\right] \exp\left\{-\frac{1}{2}[\chi - D(p - A\sin\zeta)]^2\right\}, \quad (3.17)$$

where $\zeta = k_s z$ is the phase of the electron beam. When sending the transversely dispersed electron beam through a TGU with transverse gradient α and central dimensionless parameter of K_0 , electrons with different horizontal positions will meet different K values, where $K(x) = K_0(1 + \alpha x)$. For a given beam energy, different K values result in different travel lengths according to the FEL basic functions, which converts the longitudinal coordinate z of electrons with different horizontal position into

$$z' = z + \frac{L_m K_0^2}{2\gamma^2} \left[\alpha \chi' \sigma_x + \frac{1}{2} \left(\alpha \chi' \sigma_x \right)^2 \right], \tag{3.18}$$

where L_m is the length of TGU. Considering that the horizontal electron beam size is usually quite small for FEL, Eq. (3.18) can be re-written as

$$z' = z + \frac{L_m K_0^2 \alpha \sigma_x}{2v^2} \chi', \tag{3.19}$$

and this makes the electron beam distribution after TGU become:

$$h_2(\zeta, p, \chi) = \frac{N_0}{2\pi} \exp\left\{-\frac{1}{2} [p - A \sin(\zeta - T\chi)]^2\right\} \exp\left[-\frac{1}{2} \{\chi - D[p - A \sin(\zeta - T\chi)]\}^2\right],$$
(3.20)

where

$$T = \frac{k_s L_m K_0^2 \alpha \sigma_x}{2\gamma^2} \tag{3.21}$$

is the dimensionless gradient parameter of the TGU. After passing through the DS with the dispersive strength of R_{56} , the longitudinal beam distribution evolves to

$$h_{PEHG}(\zeta, p, \chi) = \frac{N_0}{2\pi} \exp\left\{-\frac{1}{2}[p - A\sin(\zeta - T\chi - Bp)]^2\right\} \exp\left[-\frac{1}{2}\{\chi - D[p - A\sin(\zeta - T\chi - Bp)]\}^2\right],$$
(3.22)

where p now refers to the value at the entrance to the DS and $B = R_{56}k_s\sigma_\gamma/\gamma$ is the dimensionless strength of the DS. Integration of Eq. (3.22) over p and x gives the beam density N as a function of ζ , $N(\zeta) = \int\limits_{-\infty}^{\infty} dx \int\limits_{-\infty}^{\infty} dp h_{PEHG}(\zeta, p, x)$. And the bunching factor at kth harmonic can be written as

$$b_{k} = \frac{1}{N_{0}} \int_{-\infty}^{\infty} dp e^{-ikp(TD+B)-ikT\chi} f_{0}(p) g_{0}(\chi) \left\langle e^{-ik(\zeta+AB\sin\zeta)} \right\rangle$$

= $J_{n}[nAB] e^{-(1/2)[k(TD+B)]^{2}} e^{-(1/2)(kT)^{2}},$ (3.23)

For the case without TGU, i.e. T = 0, Eq. (3.23) reduces to the well-known formula for the bunching factor in a standard-HGHG FEL.

For the harmonic number k > 4, the maximal value of the Bessel function in Eq. (3.23) is about $0.67/k^{1/3}$ and is achieved when its argument is equal to $k + 0.81k^{1/3}$. For a given value of energy modulation amplitude A, the optimized strength of the DS should be

$$B = (k + 0.81k^{1/3})/kA. (3.24)$$

The maximal value of Eq. (3.23) will be achieved when TD = -B, which gives the optimized relation of α and η :

$$\alpha \eta = -\frac{2\gamma^3 (n + 0.81n^{1/3})}{nAk_{\nu}L_m K_0^2 \sigma_{\nu}}$$
(3.25)

Noticing that the third term in the right hand of Eq. (3.23) can be quite close to one when adopting a large A and η or a small horizontal beam size σ_x , so the maximal value of the nth harmonic bunching factor for PEHG will approach

$$b_n \approx 0.67/n^{1/3},\tag{3.26}$$

which is much larger than that of a standard-HGHG.

For the scheme I as shown in Fig. 3.18a, the energy modulation process and the phase-merging process are accomplished simultaneously when the electron beam passes through the TGU modulator. The electron relative phase advance caused by the gradient of the TGU is the same for scheme I and scheme II. However, a factor of 1/2 should be introduced in the right hand of Eq. (3.21), because the energy modulation approximately increase linearly with the modulator period number N_m thus the phase advance obtained by integration over the modulator length contributes a factor of 1/2. So we get the optimized dimensionless gradient parameter of TGU should become TD = -2B, and the relation between α and η for scheme I becomes:

$$\alpha \eta = -\frac{4\gamma^3 (n + 0.81n^{1/3})}{nAk_s L_m K_0^2 \sigma_{\gamma}}$$
 (3.27)

The physical mechanism behind the PEHG is the transverse-longitudinal phase space coupling. The evolution of beam longitudinal phase space is illustrated in Fig. 3.19 for the scheme II. For simplicity, here we assume the horizontal beam size $\sigma_x = 0$ and only show the phase space within one seed wavelength region. The energy modulation amplitude is chosen to be A = 3 here, and the optimized condition for the 50th harmonic bunching is $B = -TD \approx 0.35$.

The initial longitudinal phase space after passage through the dogleg is shown in Fig. 3.19a, where different colors represent for different regions of beam energy and so also represent for different horizontal positions of the electrons with respect to the reference electrons with central beam energy. After interaction with the seed laser in the conventional modulator, the longitudinal phase space of the beam evolves to that shown in Fig. 3.19b. The strong optical field induces a rapid coherent growth of the electron beam energy spread. When the beam travels through the TGU, electrons with different colors (different transverse position) will meet different undulator K values, thus result in the different travel path lengths in TGU. By properly choosing the gradient of TGU according, the phase space will evaluate to that in Fig. 3.19c. The electron energy is unchanged during this process. However, the electrons with the same energy will merge into a same longitudinal phase around the zero-crossing of the seed laser due to the relative phase shift of the electrons in TGU. This phenomenon is what we called the "phase-merging effect". After passage through TGU, electrons enter the dispersion section where the beam phase space is rotated and the bunching at the desired harmonic is optimized, as shown in Fig. 3.19d. One can find that most of the electrons are compressed into a

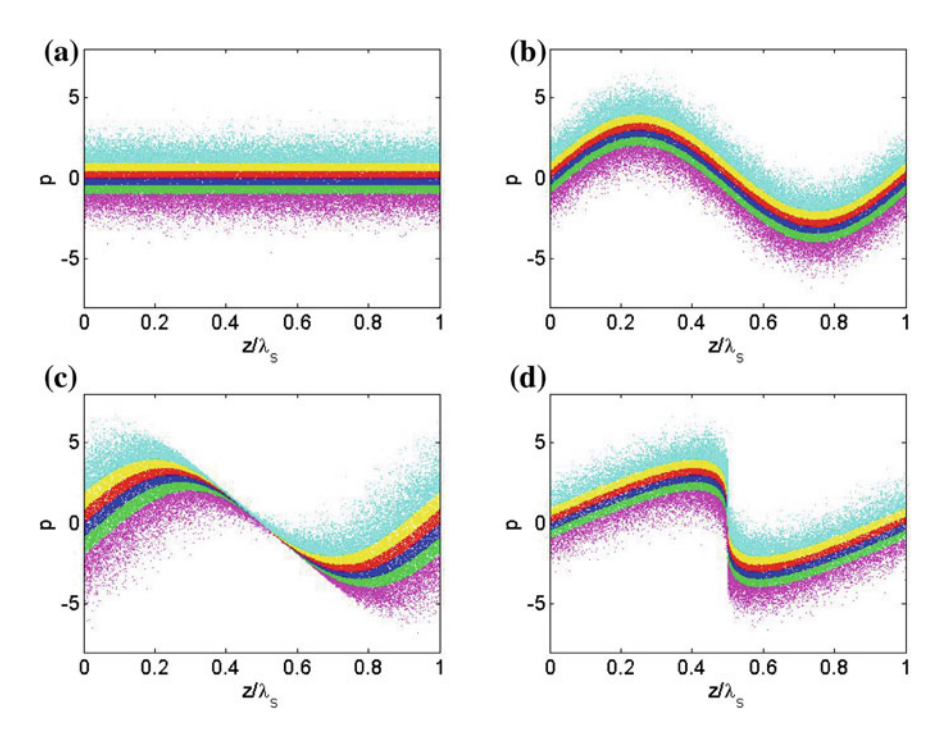


Fig. 3.19 Longitudinal phase space evolution in scheme II: **a** initial phase space after passing through the dogleg; **b** phase space at the exit of the conventional modulator; **c** phase space at the exit of the TGU; **d** phase space at the exit of the DS. (Reprint from Ref. [12]. Copyright with kind permission from IOPscience)

small region around the zero-phase, which indicates that the density modulation has been significantly enhanced for high harmonics.

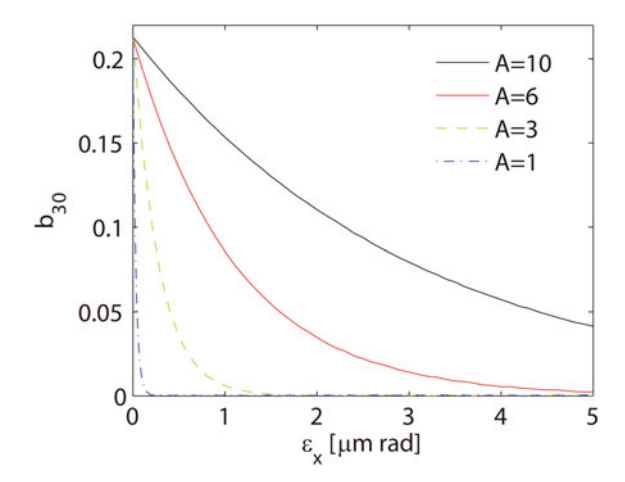
It can be deduced form Eq. (3.23) that the maximal bunching factor of PEHG is mainly determined by the Bessel function term and has little dependence on the absolute value of A when σ_x is small or η is quite large. However, the intrinsic horizontal beam size σ_x cannot be neglected for a realistic electron beam. It will induce an effective energy spread into the electron beam because of the transverse field gradient of TGU. The effective energy spread can be written as

$$\sigma_{eff} = \sigma_x/\eta. \tag{3.28}$$

Using the optimized condition of PEHG: $T\eta\sigma_{\gamma}/\sigma_{x}\gamma = -B$, plug Eq. (3.28) into Eq. (3.23), and we arrive

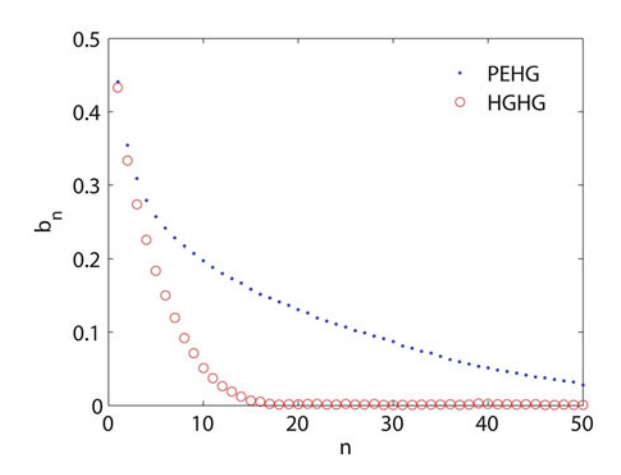
$$b_n = J_n[nAB]e^{-(1/2)(nk_sR_{56}\sigma_{eff})^2}.$$
 (3.29)

Fig. 3.20 The 30th harmonic bunching factor of PEHG as a function of the horizontal emittance for different energy modulation amplitudes. (Reprint from Ref. [12]. Copyright with kind permission from IOPscience)



One may found that the bunching factor formula of Eq. (3.29) is reduced to the bunching factor form of a standard HGHG. The only difference is that the initial beam energy spread has been replaced by σ_{eff} . Here we define an energy spread compression factor $C = \eta \sigma_v / \gamma \sigma_x$, which can be used to measure the phase-merging effect. The intrinsic beam size is determined by the normalized horizontal emittance ε_x and the beta function β . For a relatively short modulator of length L_m , it is reasonable to take $\beta \approx L_m/2$, and hence $\sigma_x = \sqrt{\varepsilon_x L_m/2\gamma}$. By using the realistic parameters of the SXFEL, Fig. 3.20 shows the 30th harmonic bunching factor as a function of the initial horizontal emittance. The beam energy is 840 MeV with energy spread of about 100 keV, the dispersion of the dogleg is $\eta = 1 \, \text{m}$, the gradient of the TGU is $\alpha = 20 \,\mathrm{m}^{-1}$, and the average beta function in the short modulator is $\beta = 0.5$ m. The energy modulation amplitude has been changed from 1 to 10, and the strength of the DS has been turned accordingly to optimize the 30th harmonic bunching factor. The wavelength of the seed laser is 264 nm. One can found from Fig. 3.20 that the bunching factor decreases quickly as the horizontal emittance increases when A is smaller than 3. However, the bunching factor is still acceptable for $\varepsilon_x = 1 \, \mu \text{m}$ rad when A is larger than 6. For the case of $\varepsilon_x = 1 \, \mu \text{m}$ rad and A = 6, the comparison of the bunching factor of PEHG and HGHG is shown in Fig. 3.21. The energy spread compression factor is calculated to be $C \approx 5.74$ for this case, which approximately makes the harmonic number increase 6 times with the same bunching factor for high harmonics.

Fig. 3.21 Comparison of the bunching factor of PEHG and standard HGHG with realistic parameters. (Reprint from Ref. [12]. Copyright with kind permission from IOPscience)

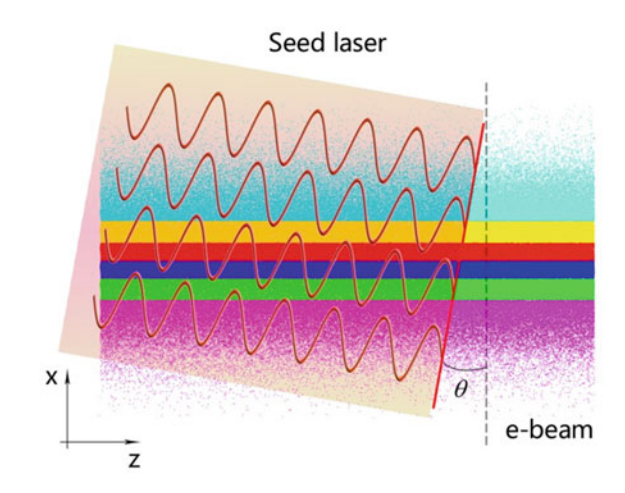


3.4.2 Three-Dimensional Manipulation for Realizing the Phase Merging Effect

The TGU in PEHG is mainly used for introducing different longitudinal phase for electrons with different transverse position (energy) to performs the phase merging effect. We found later that the phase difference can also be realized by using a wave-front tilted seed laser pulse.

The schematic of three-dimensional manipulation of the electron beam phase space is shown in Fig. 3.22, where the electron beam is transversely dispersed before entering the modulator. The wave-front tilt of the seed laser is realized by simply oblique incidence the seed laser beam with a small angle θ . Here we define a

Fig. 3.22 Schematic of three dimensional manipulation of the electron beam phase space with a transversely dispersed electron beam (x–z) and a wave-front tilted seed laser. (Reprinted with permission from Ref. [13]. Copyright 1998 by American Physical Society)



wave-front tilt gradient parameter of the seed laser as the relative phase change along the transverse direction:

$$\tau_s = \varphi/\sigma_s = k_s \tan(\theta), \tag{3.30}$$

where s represents for x or y, φ is the wave-front phase change over the transverse beam size of σ_s . After passing through the modulator, the dimensionless energy deviation of the electron beam becomes

$$p' = p + A\sin(k_s z + T_x X + T_y Y),$$
 (3.31)

where $T_x = \tau_x \sigma_x$ and $T_y = \tau_y \sigma_y$ are the dimensionless wave-front tilt gradient parameters in horizontal and vertical. The three-dimensional distribution function of the electron beam after interacting with the seed laser can be written as

$$h_{1}(\zeta, p, X, Y) = \frac{N_{0}}{\sqrt{8\pi^{3}}} \exp\left\{-\frac{1}{2}\left[p - A\sin(\zeta - T_{x}X - T_{y}Y)\right]^{2}\right\} \exp\left[-\frac{1}{2}\left\{X - D_{x}\left[p - A\sin(\zeta - T_{x}X - T_{y}Y)\right]\right\}^{2}\right] \times \exp\left[-\frac{1}{2}\left\{Y - D_{y}\left[p - A\sin(\zeta - T_{x}X - T_{y}Y)\right]\right\}^{2}\right],$$
(3.32)

After passing through the DS, the longitudinal beam distribution evolves to

$$h_{2}(\zeta, p, X, Y) = \frac{N_{0}}{\sqrt{8\pi^{3}}} \exp\left\{-\frac{1}{2}\left[p - A\sin(\zeta - T_{x}X - T_{y}Y - Bp)\right]^{2}\right\} \exp\left[-\frac{1}{2}\left\{X - D_{x}\left[p - A\sin(\zeta - T_{x}X - T_{y}Y - Bp)\right]\right\}^{2}\right],$$

$$\times \exp\left[-\frac{1}{2}\left\{Y - D_{y}\left[p - A\sin(\zeta - T_{x}X - T_{y}Y - Bp)\right]\right\}^{2}\right]$$
(3.33)

And the bunching factor at kth harmonic can be written as

$$b_{k} = \frac{1}{N_{0}} \int_{-\infty}^{\infty} dp e^{-ikp(T_{x}D_{x} + T_{y}D_{y} + B) - ik(T_{x}X + T_{y}Y)} f_{0}(p) g_{0}(X, Y) \left\langle e^{-ik(\zeta + AB\sin\zeta)} \right\rangle$$

$$= J_{k}[kAB] e^{-(1/2)[k(T_{x}D_{x} + T_{y}D_{y} + B)]^{2}} e^{-(1/2)(kT_{x} + kT_{y})^{2}},$$
(3.34)

which is similar with Eq. (3.23). The maximal value of b_k will be achieved when $T_xD_x + T_yD_y = -B$, which gives the optimized relation of τ and η :

$$\tau_x \eta_x + \tau_y \eta_y = -(n + 0.81n^{1/3})\gamma / nA\sigma_\gamma. \tag{3.35}$$

And the maximal value of the *k*th harmonic bunching factor will also approach $b_n \approx 0.67/n^{1/3}$.

3.4.3 Generation of Soft X-Ray Radiation Based on a Single Stage PEHG

To illustrate a possible application of the PEHG technique with realistic parameters, we take the nominal parameters of the SXFEL. The SXFEL aims at generating 8.8 nm FEL from a 264 nm seed laser through an initial designed double-stage cascaded HGHG. However, by using the proposed method, this goal could be achieved by a single stage configuration. A dogleg is added before the modulator for the generation of transverse dispersion in the electron beam, and a wave-front tilted seed laser pulse is utilized to interact with the electron beam in the modulator. Quadruples are placed at both upstream and downstream of the dogleg for matching the transverse beam size and cancel the correlation between particle energy and transverse divergence. The required electron beam energy is 840 MeV at the end of the linac. The bunch charge is about 0.5 nC. With these parameters, start-to-end simulations have been carried out. The electron beam dynamics in photo-injector was simulated with ASTRA [14] to take into account space-charge effects. ELEGENT [15] was used for the simulation in the remainder of the linac, while tracking in the undulators was performed with GENESIS. The beam energy and current distributions along the electron bunch are summarized in Fig. 3.23a. After horizontally dispersing the electron beam by the dogleg dispersion $\eta_x = 0.5$ m, the average value of the horizontal beam size σ_x is increased from about 60–70 µm, as shown in Fig. 3.23b, which will not significantly affect the FEL performance.

The three-dimensional phase space manipulation process and the FEL performance were simulated with GENESIS based on the output of ELEGENT. For comparison purpose, simulations for double-stage cascaded HGHG have also been carried out. A 264 nm seed pulse with longitudinal pulse length of about 8 ps (FWHM) is adopted for single stage case and a much shorter pulse length of about 100 fs is adopted for the cascaded HGHG case. The peak power and the Rayleigh length of the seed laser are chosen to be 400 MW and 7.5 m for both these two

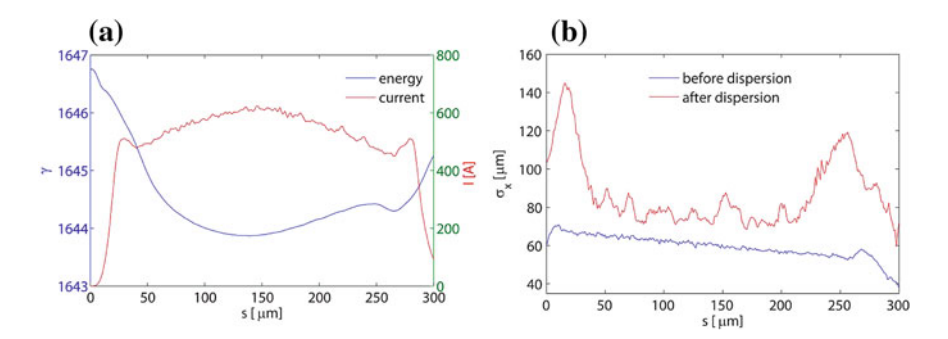


Fig. 3.23 Simulated parameters at the exit of the linac. **a** Beam energy and current distribution along the electron beam. **b** horizontal beam size before and after the dipsersion. (Reprinted with permission from Ref. [13]. Copyright 1998 by American Physical Society)

cases for maintaining a sufficient temporal superposition between electron and laser beams. The length of the modulator is about 1 m with period length of 80 mm. To maximize the bunching factor at 30th harmonic of the seed laser, the parameters for the single stage HGHG case are set to be A = 5, B = 0.2 and $\tau_x \approx 3.6$ rad/mm, where the $\tau_{\rm r}$ is generated by directly tilt the wave-front of the seed laser in the simulation. The bunching factor at the entrance of the radiator is about 5 %. The period length of the radiator is 25 mm with K value of about 1.3. The electron beams are both well matched in the radiator, which makes the average horizontal beta functions are $\overline{\beta}_x \approx 5 \, \text{m}$ for the cascaded HGHG case and $\overline{\beta}_x \approx 8 \, \text{m}$ for the single stage case. The evolution of the radiation pulse energy is shown in Fig. 3.24a, where the large bunching factor at the entrance to the radiator offered by the three-dimensional phase space manipulation is responsible for the initial steep quadratic growth of the power. The significant output pulse energy enhancement is clearly seen. The pulse energy of the 30th harmonic radiation approaches 100 µJ at saturation, which is one order of magnitude higher than that of the original design of SXFEL with double-stage cascaded HGHG. Moreover, the 8.8 nm radiation saturates within 15 m long undulator, which is in the range of original design of SXFEL. The single-shot radiation spectra for these two cases at saturation are shown in Fig. 3.24b. The spectral bandwidth at saturation for the single stage HGHG with three-dimensional phase space manipulation (blue solid line) is about 0.08 %, which is quite close to transform limit. However, the bandwidth of the cascaded HGHG (red dashed line) is about 0.6 %, which is 1.7 times wider than the transform limit. The bandwidths broadening and spectral noises in the spectrum of cascaded HGHG are mainly induced by the initial energy curvature of the electron beam, which is unavoidable in the FEL linacs due to the radio frequency curvature and wake field effects. However, the dependence of output spectrum in seeded FEL on the residual beam energy chirp can be canceled when using the PEHG technique. Here we assume an initial linear energy chirp h in the electron beam. After

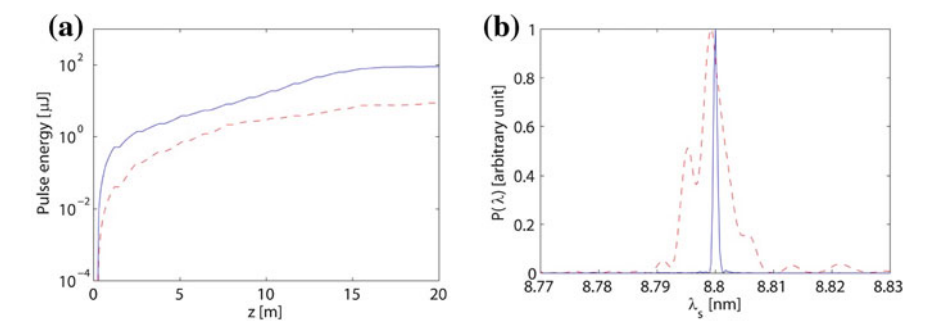


Fig. 3.24 Comparison of the FEL simulation results for double-stage cascaded HGHG (*red dashed line*) and a single stage PEHG: **a** evolution of the soft x-ray FEL pulse energy along the radiator; **b** spectra at saturation. (Reprinted with permission from Ref. [13]. Copyright 1998 by American Physical Society)

transversely dispersing the electron beam with D_x , the longitudinal energy chirp results in a similar scaled chirp in the electron beam transverse distribution:

$$X' = X + D_x(p + h\zeta). \tag{3.36}$$

It has been point out that the electrons with different transverse positions will get different energy modulation phases in the modulator when the seed laser wave-front is tilted by T_x . Here we plug Eq. (3.36) into Eqs. (3.31–3.34) and get the bunching factor for an electron beam with linear chirp as

$$b_{k} = \frac{1}{N_{0}} \int_{-\infty}^{\infty} dp e^{-ikp(T_{x}D_{x}+B)-ikT_{x}X} f_{0}(p) g_{0}(X,Y) \left\langle e^{-ik\zeta[1+h(T_{x}D_{x}+B)]} e^{-ikAB\sin\zeta} \right\rangle. \quad (3.37)$$

So the optimized output frequency can be written as

$$k_k = \frac{nk_s}{1 + h(T_x D_x + B)},$$
(3.38)

As the optimized condition for the bunching factor is $T_xD_x = -B$, one can easily find in Eq. (3.38) that the output radiation wavelength and bandwidth is naturally immune to the beam energy chirp for the single-stage PEHG.

3.5 Generating Stable Attosecond X-Ray Pulse Trains with a Mode-Locked Seeded FEL

Besides pushing the output of a high-gain FEL to shorter wavelengthes, generation of ultra-short radiation pulses is also highly desirable in FEL user community. Reducing x-ray FEL pulse durations to the attosecond regime will provide spatiotemporal resolution and potential control of atomic processes, which will open up many new ultrafast science.

Attosecond Pulse Trains (APTs) have proven a valuable tool in atomic and molecular science [16–18]. It has been proposed that the APTs can also been generated by the SASE FEL using a mode-locked amplifier [19], which consists of a system of undulator-chicane modules. In this amplifier, a comb of longitudinal modes can be synthesized by the optics-free technique applying a series of temporal shifts between the co-propagating radiation and electron bunch. The neighboring modes may be locked in phase by introducing an interaction modulation at the mode spacing, for example, an energy modulation induced by a seed laser interacting with the electron beam in a modulator. With the conventional atomic laser, this mode locking modifies the temporal envelop of the output field from continuous wave to a train of short pulses, periodically spaced by the wavelength of the seed laser. However, as the radiation originates from the shot noise of the electron beam, this scheme may still have large shot-to-shot output power fluctuations and

usually needs a large number of undulator-chicane modules to produce a clean series of short pulses. Moreover, the spacing between the attosecond pulses is limited by the wavelength of the seed laser.

In this section, we propose a scheme that combines the EEHG technique with the mode-locked technique to generate coherent, stable attosecond x-ray pulse trains with GW level peak power directly from ultraviolet seed lasers.

3.5.1 Mode-Locking of a Seeded FEL

The proposed scheme consists of three modulators, two DSs and a mode-locked radiator, as shown in Fig. 3.25. Compared to the standard EEHG scheme, one more seed laser and modulator are added for tuning the spacing of the APT. The modulators and DSs are used for generation of density modulation at high harmonics with a relatively small initial energy modulation of the electron beam, which benefits from the beam echo effect. The electron beam is first energy modulated by a seed laser (seed1) with wave number k_1 in the first modulator (M1) and then sent through a strong dispersion section (DS1), which makes the energy modulation induced in M1 macroscopically smeared out, but many well-structured beamlets appear in the phase space. This electron beam then interacts with two seed lasers (seed2 & seed3) with different wave numbers k_2 and k_3 to obtain sufficient energy modulations in M2 and M3, respectively. Meanwhile, the beating frequency k = $k_2 - k_3$ occurs in the phase space of the electron beam. When k is the sub-harmonic frequency of both k_2 and k_3 (i.e. $k = k_2/m_1 = k_3/m_2$, where m_1 and m_2 are integer numbers), the phase space will be periodic with a new energy modulation envelope period $\lambda s = 2\pi/k$, which can be tuned to be much longer than the wavelengths of the seed lasers. After the electron beam passing through the second dispersive section (DS2), the energy modulation will be converted into density modulation and the echo signal occurs at some high harmonics of the seed lasers.

The distribution function of the electron beam after DS1 can be written as

$$f_2(\zeta, p) = \frac{N_0}{\sqrt{2\pi}} \exp\left\{-\frac{1}{2}[p - A_1 \sin(\zeta - B_1 p)]^2\right\}$$
(3.39)

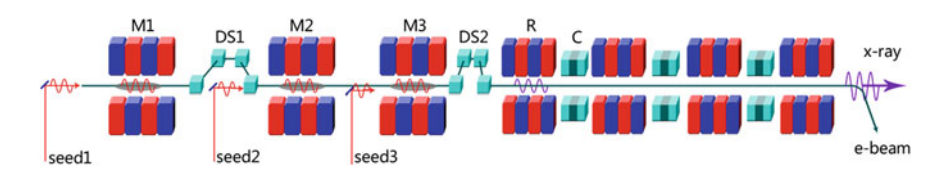


Fig. 3.25 Schematic of the proposed scheme for generation of attosecond x-ray pulse trains. (*M* modulator, *DS* dispersive section, *R* radiator, *C* chicane) (Reprinted with permission from Ref. [20]. Copyright 1998 by American Physical Society)

Assume that the electron beam is energy modulated in M2 and M3 with the same dimensionless amplitude $A_2 = A_3$. After passing through DS2 with the dispersive strength B_2 , the longitudinal beam distribution evolves to

$$f_3(\zeta, p) = \frac{N_0}{\sqrt{2\pi}} \exp\left[-\frac{1}{2} \{p - A_2 \sin(K_1 \zeta - K_1 B_2 p + \phi) - A_2 \sin(K_2 \zeta - K_2 B_2 p + \phi') - A_1 \sin[\zeta - (B_1 + B_2)p + A_2 B_1 \sin(K_1 \zeta - K_1 B_2 p + \phi) + A_2 B_1 \sin(K_2 \zeta - K_2 B_2 p + \phi')]\}^2\right]$$

$$(3.40)$$

 ϕ and ϕ' are the phases of seed2 and seed3, $K_1 = k_2/k_1$ and $K_2 = k_3/k_1$. Integration of this formula over p gives the beam density distribution function. And the bunching factor at nth harmonic can be written as

$$b_{k} = \left| \sum_{n_{1}=-\infty}^{\infty} \sum_{n_{2}=-\infty}^{\infty} J_{n2} \{-nA_{2}B_{2}\} J_{n3} [-nA_{2}B_{2}] J_{n1} \{-A_{1}[n_{1}B_{1}+nB_{2}]\} e^{-1/2[n_{1}B_{1}+nB_{2}]^{2}} e^{i(n_{2}\phi+n_{3}\phi')} \right|$$

$$(3.41)$$

where n_1, n_2 and n_3 are integer numbers, and the harmonic number $n = n_1 + K_1n_2 + K_2n_3$. n_1 is chosen to be -1 to make B_1 and B_2 have the same sign. For given A_1 and A_2 , the maximal bunching factor is achieved when

$$\begin{cases}
B_2 = (n_2 + 0.81n_2^{1/3})/kA_2 \\
A_1\{J_0[A_1(kB_2 - B_1)] - J_2[A_1(kB_2 - B_1)]\} = 2(kB_2 - B_1)J_1[A_1(kB_2 - B_1)] \\
(3.42)
\end{cases}$$

FEL radiation is highly relevant to the longitudinal distribution of the electron beam, especially the beam current and the bunching parameter. After the DS2, attosecond scale micro-structures come out over one seed wavelength in the electron beam. This kind of electron beam will generate coherence APTs at the very beginning of the radiator. However, the ultra-short radiation structure will be quickly smeared out by the slippage effect in the long radiator when the period number is larger than the harmonic number. It is found that the radiation trains can be maintained and amplified by taking advantage of the mode-locked technique, as shown in Fig. 3.26. A series of spatiotemporal shifts are introduced between the radiation and the co-propagating electron bunch by delaying the electron bunch using magnetic chicanes inserted between undulator modules. These small chicanes also act as dispersion sections, but the strength of each chicane $(R_{56} \sim 10^{-6} \,\mathrm{m})$ is much smaller than the strengths of the DSs ($R_{56} \sim 10^{-3}$ m). The total slippage per module is $\bar{s} = \bar{l} + \bar{\delta}$, where \bar{l} is the slippage due to the undulator and $\bar{\delta}$ is the slippage due to the chicane. In each module, the radiation wavefront will propagate ahead and interact with the electrons within \bar{l} in the undulator. After passing through a small chicane, the radiation will be shifted ahead by $\bar{\delta}$ and interact with another part of the electron beam in the following undulator. When the total

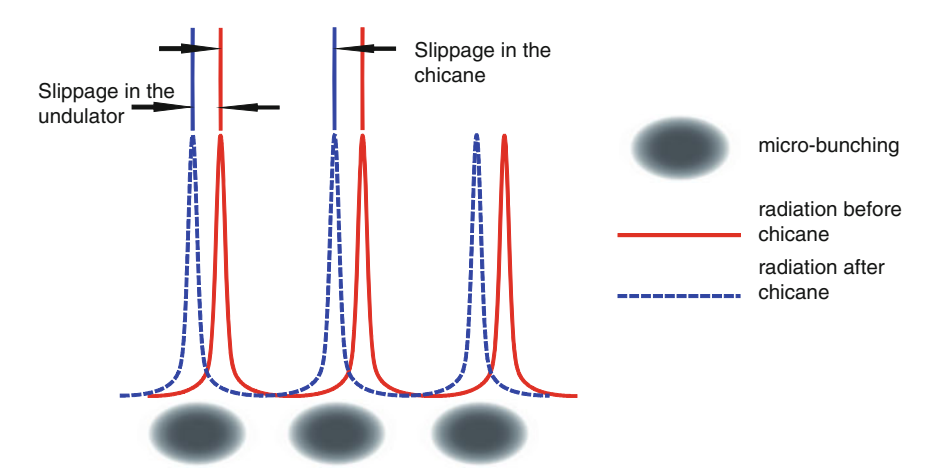


Fig. 3.26 Principle of the mode-locked amplification for a seeded FEL. (Reprinted with permission from Ref. [20]. Copyright 1998 by American Physical Society)

slippage length \bar{s} is equal to the wavelength of the energy modulation envelope λ_s , the radiation would take over the next high current spike at the beginning of the next undulator section. The FEL interaction at different longitudinal positions along the beam will be periodically suppressed or enhanced, so the train of evenly spaced pulses will develop aligned with the regions of high beam current and large bunching factor.

For the kth harmonic radiation, the electrons in $[0, 2\pi]$ in the modulator are transformed to $[0, 2k\pi]$ in the radiator, and the bunching parameter corresponding to the radiation wavelength $\lambda_r = \lambda_{seed1}/k$ in the radiator is no more uniform over the distance of one seed laser wavelength λ_{seed1} . As the radiation only interacts with electrons within \bar{l} in each module, the electrons over the distance λ_{seed1} should be uniformly divided into slices with length \bar{l} and the electrons in each slice are independent with other slices. The local current I_k and the local bunching factor B_k at position z along the electron beam should be defined as:

$$\begin{cases}
I_{k}(z) = \int_{z-\bar{l}/2}^{z+\bar{l}/2} N(z') dz' / \bar{l} \\
B_{k}(z) = \int_{z-\bar{l}/2}^{z+\bar{l}/2} N(z') e^{-ikz'} dz' / \int_{z-\bar{l}/2}^{z+\bar{l}/2} N(z') dz'
\end{cases}$$
(3.43)

As $K_2 = 3/4$, the phase space of the electron beam will be periodic with $\lambda_s = 4\lambda_{seed1}$. The phase space in one period of energy modulation envelope is shown in Fig. 3.27a, which is calculated by Eq. (3.40). The beam local current and local bunching factor distributions are calculated by Eq. (3.43), and illustrated by Fig. 3.27b. The local bunching factor in the central part of each period is around

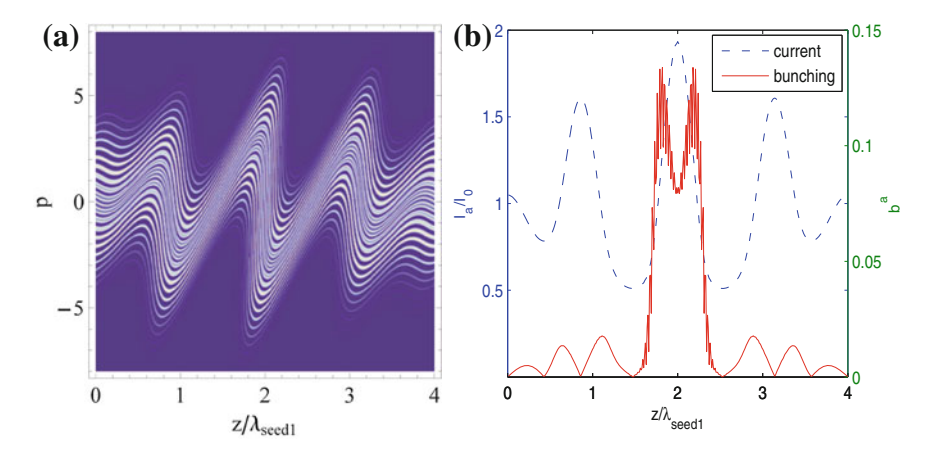


Fig. 3.27 Phase space (a) and corresponding local current factor and local bunching factor distributions (b) at the exit of DS2. (Reprinted with permission from Ref. [20]. Copyright 1998 by American Physical Society)

0.12; while in other parts are around 0.01. The peak value of the local current is nearly two times larger than the initial one.

3.5.2 Generation of Intense APTs

To illustrate a possible application of the proposed scheme with realistic parameters, we take the nominal parameters of the upgraded SXFEL project. The main parameters of the upgraded SXFEL are presented in Table 3.2. For comparison purpose, three cases are considered, including the conventional EEHG and triple-modulator scheme proposed here with seed3 off and on. We assume that the wavelengths of the seed1 and seed2 are 266 nm in these three cases, and the wavelength of the seed3 is chosen to be 355 nm for the third case. To maximize the bunching factor at 34th harmonic of seed1, the optimized parameters are $A_1 =$ $2, A_2 = 3, B_1 = 13.2, B_2 = 0.37$ for the first two cases, and chosen to be the same as that used in Fig. 3.20 for the third case. The corresponding peak powers of the seed lasers used in the simulations are $P_1 = 15$ MW, $P_2 = 32$ MW for the first two cases and $P_1 = 15 \,\mathrm{MW}, P_2 = 8 \,\mathrm{MW}, P_3 = 5 \,\mathrm{MW}$ for the third case. The resonant wavelengths of radiators are $\lambda_r = 7.8$ nm. For the second case, undulator periods in each modules are chosen to be $N_u = 8$ so that $\bar{l} = 8\lambda_r$, and the relative electron beam over radiation slippage induced by the dispersive effect of each chicane placed between the undulator modules is set to be $\bar{\delta} = 26\lambda_r$, with total slippage due to undulator and delay section $\bar{s} = \lambda_{seed2}$. When seed3 is used to generate the energy modulation envelope, the chicane delay is changed to $\bar{\delta} = 128 \, \lambda_r$ which makes $\bar{s} = 4 \lambda_{seed2}$. The length of each chicane is 0.5 m with adjustable dispersion strength from 0 to 18 μm.

Table 3.2 Simulation parameters for the mode-locked EEHG

Electron beam					
Beam energy [GeV]	1.3				
Slice energy spread [keV]	65				
Peak current [A]	1500				
Slice emittance [mm-mrad]	1				
Pulse length (FWHM) [ps]	~0.5				
Seed laser	1 2 3				
Wavelength [nm]	266 266 355				
Pulse length (FWHM) [ps]	8 8				
Modulator	1 2 3				
Period length [cm]	8 8 8				
Period number	10 10 10				
Resonant wavelength [nm]	266 266 355				
Radiator					
Period length [cm]	3				
Resonant wavelength [nm]	7.8				
Undulator parameter K	1.535				

Reprinted with permission from Ref. [20]. Copyright 1998 by American Physical Society

After passing through DS2, the electron beam will be bunched at various harmonics of seed2 as Fig. 3.28 shows, which indicates bunching at different modes. The bunching spectrums for the first two cases are the same with the maximal value

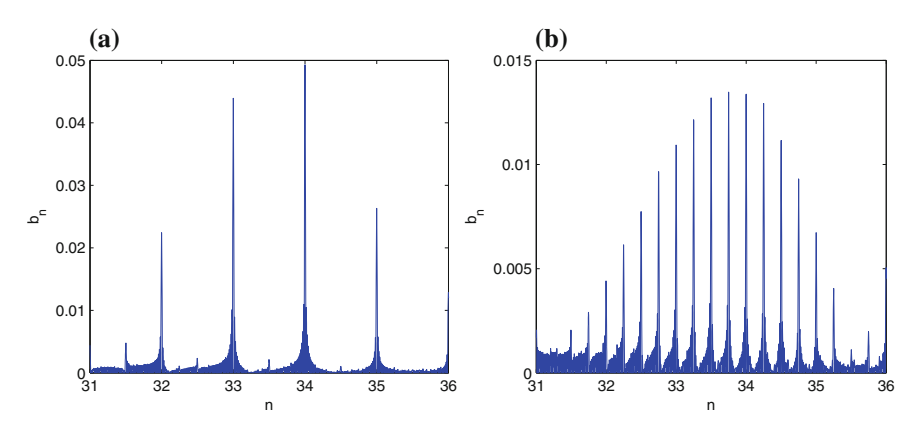


Fig. 3.28 Average bunching factor as a function of the harmonic number at the entrance of the radiator: **a** Conventional EEHG and triple-modulator scheme with seed3 off. **b** Triple-modulator scheme with seed3 on. (Reprinted with permission from Ref. [20]. Copyright 1998 by American Physical Society)

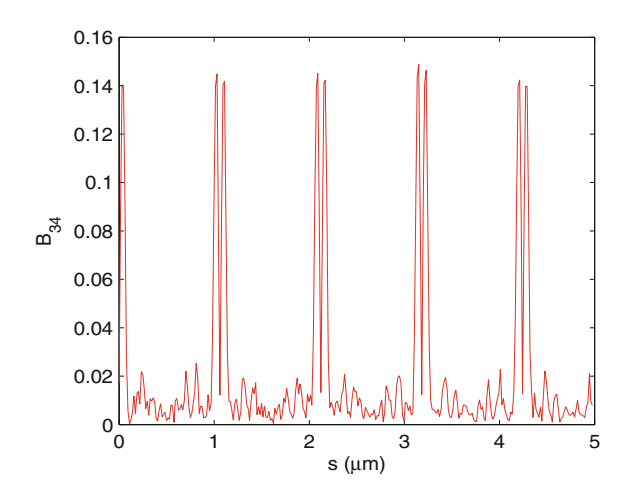
of about 0.05 at 34th harmonic (Fig. 3.28a). The bunching spectrum of the third case contains more harmonics but a lower maximal value of about 0.015 (Fig. 3.28b). By properly setting the parameters of the mode-locked radiator, some of these harmonics (modes) can be phase-locked and amplified to saturation.

The local bunching factor distribution calculated by GENESIS for the third case is shown in Fig. 3.29. One can find that the maximal local bunching factor is nearly one order of magnitude larger than the average one, which is also much larger than the average bunching factor of the conventional EEHG.

The output radiation pulses and corresponding spectrums close to saturation for these three cases are shown in Fig. 3.30. For the conventional EEHG case, as shown in Fig. 3.30a, the radiation power is constant along the chosen part of the electron beam with a spectrum centered at the resonant wavelength of Fourier transform limited bandwidth (Fig. 3.30b), results typical of the seed FEL regime. In Fig. 3.30c, mode-locking occurs in the radiator, and stable separated pulse trains with width of about 200 as evenly spaced by about 800 as is generated. The spectrum (Fig. 3.30d) has sideband modes with separation of about 0.22 nm. For the third case, when the third modulator is used to generate the energy modulation envelope, the separation between the radiation pulses will become 4 times larger than the second case as Fig. 3.30e shows. The 200 as radiation pulses are separated by about 3.3 fs, which can be tuned even larger by changing the wavelength of seed3 and the strengths of the chicanes in the radiator. The spectrum has more sideband modes with separation of about 0.055 nm (Fig. 3.30f).

Figure 3.31 shows the radiation peak powers as a function of the undulator length for these three cases. In order to illustrate the difference in FEL gain length, radiation power variations in the chicanes are not included in these curves. It is calculated from these curves that the gain length for the conventional EEHG is 1.36 m, which is reduced to 0.62 m when using the mode-locked radiators. The dispersion induced by the small chicanes will also accelerate the FEL saturation process and result in a shorter saturation length but a lower saturation power.

Fig. 3.29 Local bunching factor distribution along the electron beam at the entrance of the radiator for the third case. (Reprinted with permission from Ref. [20]. Copyright 1998 by American Physical Society)



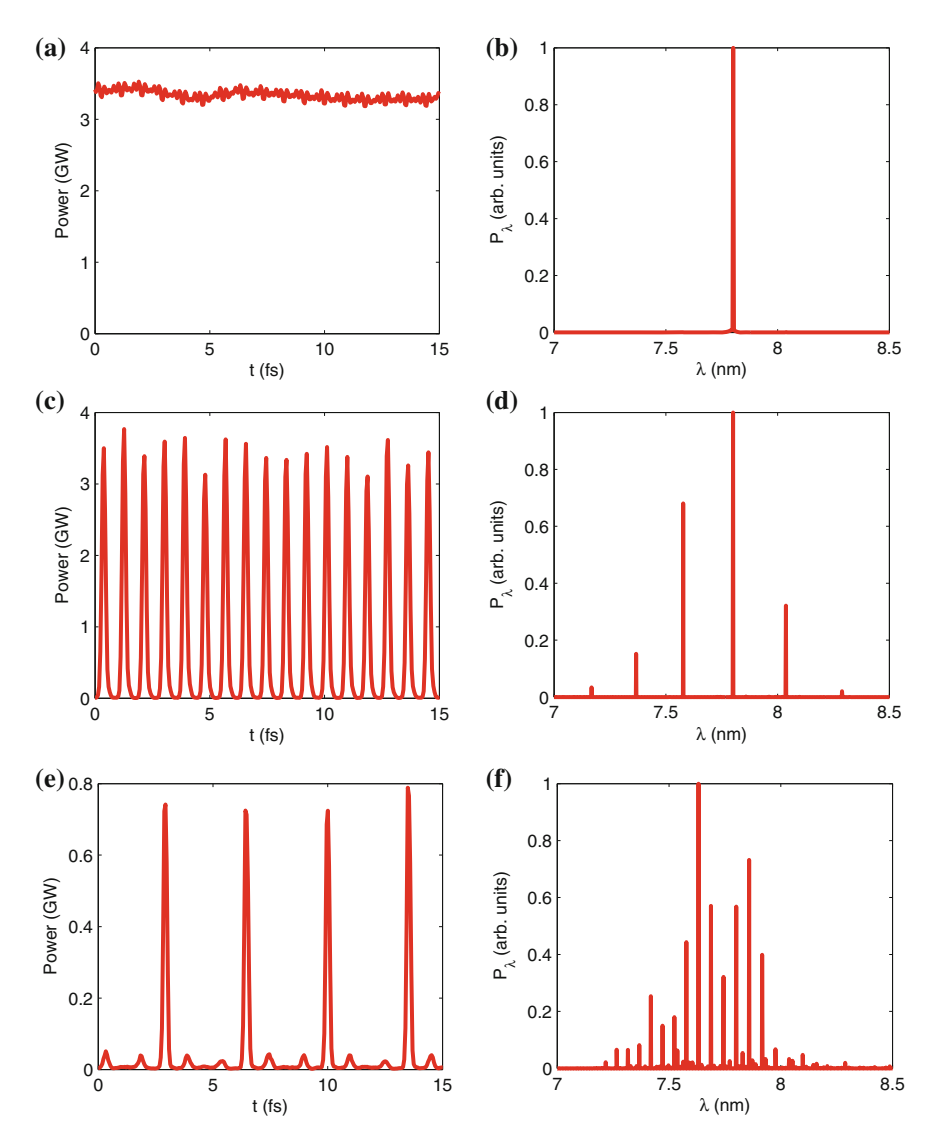


Fig. 3.30 Radiation pulses close to saturation and the corresponding radiation spectrums for three cases. a radiation pulse of conventional EEHG, $\bf b$ spectrum of conventional EEHG, $\bf c$ radiation pulse of triple-modulator scheme with seed3 off, $\bf d$ spectrum of triple-modulator scheme with seed3 off, $\bf c$ radiation pulse of triple-modulator scheme with seed3 on and $\bf f$ spectrum of triple-modulator scheme with seed3 on. (Reprinted with permission from Ref. [20]. Copyright 1998 by American Physical Society)

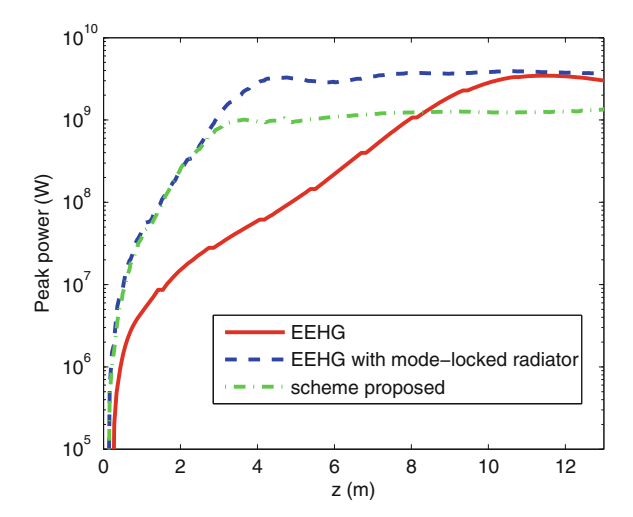


Fig. 3.31 Radiation peak power as a function of undulator length (radiation power variations in the chicanes of each module is not drawn) for the three cases: EEHG without a mode-locked radiator (*red solid curve*), triple-modulator scheme with seed3 off (*blue dashed curve*) and triple-modulator scheme with seed3 on (*green dot-dashed curve*). (Reprinted with permission from Ref. [20]. Copyright 1998 by American Physical Society)

The FEL reaches saturation after about 15 modules with the saturation peak power of about 3.5 GW for the second case. By increasing the strengths of the chicanes for the third case, an even shorter saturation length of about 3 m of undulator (11 modules) is expected, with the saturation peak power of about 0.8 GW.

3.6 Chirped Pulse Amplification of a Seeded FEL

In the previous section, we borrow the idea of mode-locking from the solid-state lasers for the generation of coherent APTs via a seeded FEL. Another well-known technique at optical frequencies in laser physics that can be used to generate extremely high power ultra-short pulses is so called the Chirped pulse amplification (CPA) [21]. The CPA technique holds the capability for producing laser pulses with peak power well above 100 TW, which has enabled many important areas of scientific research such as strong-field physics. However, there are technical challenges to extend the wavelength to below 200 nm in standard CPA lasers, because of the strong absorption of the materials used in conventional laser amplifiers.

Note that the high-gain free-electron lasers (FELs) have shown the capability to produce high-power radiation down to the x-ray wavelengths. It is then natural to apply the CPA technique in high-gain FELs to generate intense pulses with ultra-short durations at shorter wavelengths not accessible with standard lasers. Specifically, the electron beam with a nonzero energy chirp (correlation between

beam's energy and longitudinal position) generates a chirped electro-magnetic radiation pulse in an FEL, which may be further compressed in time by a compressor.

Properties of frequency-chirped FEL generated by SASE configuration have been studied both theoretically and experimentally [22, 23]. It was observed that the spikes in the SASE output had an intrinsic positive frequency chirp even if the energy chirp in the electron beam was absent, in agreement with the analytical calculation and simulation. It was also shown that an electron energy chirp directly led to a frequency chirp in the FEL output. However, to create a chirped output radiation pulse that can be compressed to a short pulse, the frequency must be very accurately chirped, i.e., from the head to the tail of the pulse the optical phase relationship should be as coherent as if it had been originally stretched from a compressed short pulse. It is difficult to generate such coherence starting from noise, as occurs in SASE schemes. Hence, from the standpoint of phase coherence, the choice of a seeded single pass FEL amplifier seems a more promising configuration to integrate CPA technique, since the property of a seeded FEL output is a direct map of the seed laser's attributes. Applying CPA techniques in a seeded FEL for femtosecond level pulses generation at VUV region has been proposed in Ref. [24]. A preliminary CPA experiment at 800 nm with direct seeding scheme has been carried out at BNL [25], where the bandwidth of the radiation pulse was measured to be larger than the seed and the radiation pulse is compressed to duration shorter than the seed pulse. The CPA experiment has also been carried out in HGHG process at 266 nm, but properties of the FEL output such as frequency chirp has not been characterized [26]. Here we study CPA operation of HGHG for generation of high peak power ultra-short UV pulses and discuss the possibility of carrying out a proof-of-principle experiment at SDUV-FEL facility.

3.6.1 Chirped Pulse Amplification in a Seeded FEL

A schematic layout of the SDUV-FEL with CPA-HGHG setup is shown in Fig. 3.32. To produce a frequency chirped seed pulse, the seed laser pulse with a bandwidth of a few percent is optically stretched with a pair of gratings. The FEL power growth in the radiator of HGHG can be divided into three stages: the CHG,

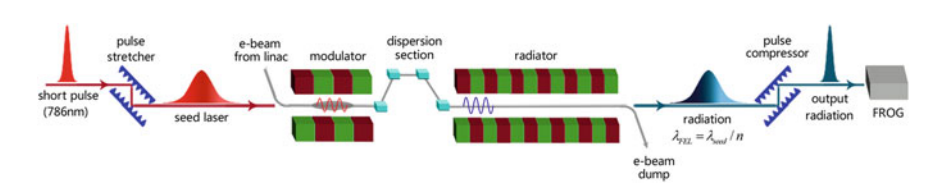


Fig. 3.32 Schematic layout of the SDUV-FEL with CPA-HGHG setup. (Reprinted from Ref. [27], Copyright 2012, with permission from Elsevier)

the exponential growth and saturation. In the first two gain lengths of the radiator, the FEL works in the CHG regime, where the harmonic field grows linearly with the distance traversed in the radiator z, and the peak power grows as z^2 . Then, the radiation field is fully coupled with the longitudinal dynamics of the electron beam, and the radiation power will be exponentially amplified along the radiator until saturation.

Typically the modulator works at the small-gain regime with a bandwidth of about $1/N_m$, where N_m is the period number of the modulator. Similarly, in the CHG scheme, the radiator is relatively short and no exponential growth is expected, therefore the electron beam behaves as a collection of rigid microbunches and the FEL also works in the small-gain region. Accordingly, the relative FEL gain bandwidth is $1/N_c$, where N_c is the period number in the radiator used for CHG. For CPA-CHG scheme with the bandwidth of the seed laser comparable to the gain bandwidths of the modulator and the radiator, the frequency chirped pulse can be directly generated through the CHG process and there will be no need for an initial energy chirp in the electron beam.

For a high-gain FEL with a long radiator, the FEL gain bandwidth is close to the Pierce parameter ρ , which is in the range of 10^{-3} for an ultraviolet FEL. In order to amplify a chirped pulse with a few percent bandwidth, the electron beam need to be prepared with an energy chirp to match the resonance condition:

$$\gamma(s) = \sqrt{\frac{n\lambda_r}{2\lambda_s(s)}(1 + K^2/2)}$$
(3.44)

where $\lambda_s(s)$ is the wavelength distribution along the seed laser pulse, n is the harmonic number, λ_r is the period length of the radiator and K is the strength of the radiator, s is used to denote the longitudinal position along the electron bunch.

The output radiation pulses generated by CPA-CHG and CPA-HGHG inherit the properties of the seed and therefore can be compressed by a system with nonzero group delay dispersion, i.e., a grazing-incidence double-grating device as shown in Fig. 3.25. The minimal pulse duration after compression corresponds to a transform-limited pulse, which can be expressed as [28]

$$\tau = \frac{\lambda_r}{2cb_w} = \frac{\lambda_s}{2cb_w k} \tag{3.45}$$

where b_w is the bandwidth of the seed laser. From this equation, one may easily find that the transform-limited pulse duration is mainly determined by the wavelength and bandwidth of the seed laser. For kth harmonic radiation, the transform-limited pulse duration would be k times shorter than the seed.

To fully characterize the longitudinal properties of the chirped laser pulse in both the time and frequency domains, the Wigner distribution function is routinely used [29, 30],

$$W(t, \omega, s) = \int E(t - \tau/2, s) E^*(t + \tau/2, s) e^{-i\omega\tau} d\tau, \qquad (3.46)$$

where * denotes the complex conjugate, E(t,s) is the electric field of the laser pulse and ω is the laser frequency. The Wigner distribution can be measured by several recently developed techniques, such as frequency-resolved optical gating (FROG) [31] and spectral phase interferometry for direct electric-field reconstruction (SPIDER) [32].

3.6.2 Start-to-End Simulations Based on the SDUV-FEL

The layout and parameters of the SDUV-FEL with CPA-HGHG setup are shown in Table 3.3. A 786 nm laser pulse, which is stretched from 82 fs to 4.7 ps (FWHM) with a longitudinal Gaussian profile and peak power of 20 MW, is used as the seed laser. The bandwidth of the seed laser is about 2 %. The modulator, a 16×40 mm permanent magnet undulator, is set to fulfill the resonant conditions with beam

Table 3.3 Main simulation parameters for the CPA-HGHG

Electron beam	
Beam energy [MeV]	160
Charge [pC]	250
Peak current [A]	40
Emittance [mm-mrad]	1.5
bunch length (FWHM) [ps]	6.3
Seed laser	
Peak power [MW]	20
Pulse length (FWHM) [ps]	4.7
Central wavelength [nm]	786
Bandwidth	2 %
Modulator	·
Period length [cm]	4
Resonant wavelength [nm]	786
Length [m]	0.64
Dispersion section	
Strength R ₅₆ [mm]	0.25
Radiator	
Period length [cm]	2.5
Resonant wavelength [nm]	262
K	1.45
Length [m]	9

Reprinted from Ref. [27], Copyright 2012, with permission from Elsevier

energy and laser seed. The strength of the chicane can be easily tuned with a maximal momentum compaction of about 10 mm. The radiator consisting of six 60-period permanent magnet undulators with 25 mm period length is set in such a way that the FEL wavelength is the 3rd harmonic of laser seed.

With the parameters shown in Table 3.3, start-to-end tracking of the electron beam has been carried out for the CPA-HGHG experiment. The energy and current distributions along the electron beam at the exit of the linac are summarized in Fig. 3.33. For comparison purpose, two cases have been studied here: one is using a normal electron beam as that used in conventional HGHG. The average beam energy is around 160 MeV and the peak currents is about 40 A when the electron beam is compressed by a factor of about 2. Another case is adjusting the rf phase of the linac to imprint considerable negative energy chirp on the electron beam to match the resonance condition of the chirped seed laser. It is found in Fig. 3.33b that the energy chirp is nearly linear with quadratic component due to the radio frequency curvature in the accelerator. This quadratic component will not affect the interaction between the electron beam and chirp seed laser in the modulator, as the gain bandwidth of the modulator is quite broad. However, the output radiation bandwidth will be broadened due to the nonlinear effect caused by this quadratic component, which will degrade the quality of the radiation pulse and affect the performance of the CPA.

For the normal electron beam case, the bandwidth of the seed is much narrower than the gain bandwidth of the modulator (about 6.25 %), which means that all parts of the seed spectrum effectively contribute to the energy modulation of the electron beam. The evolutions of pulse energies along the radiator undulator and the spectra of the radiation pulses at saturation are illustrated in Fig. 3.34. Three FEL gain stages in the radiator are clearly shown in Fig. 3.34a: rapid coherent emission at 3rd harmonic of the seed is produced within the first undulator segment. Further exponential amplification begins from the second undulator segment and ultimate saturation is achieved after about 6 m with saturation pulse energies of 13.8 μ J for

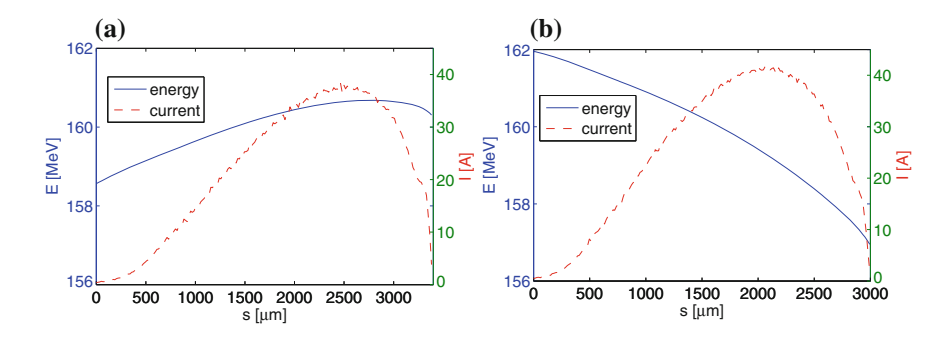


Fig. 3.33 Beam energy and current distributions along the electron beam (bunch head is to the right) at the exit of the linac for two cases: **a** normal electron beam used in conventional HGHG. **b** Electron beam with considerable energy chirp to match the seed laser frequency chirp in CPA-HGHG. (Reprinted from Ref. [27], Copyright 2012, with permission from Elsevier)

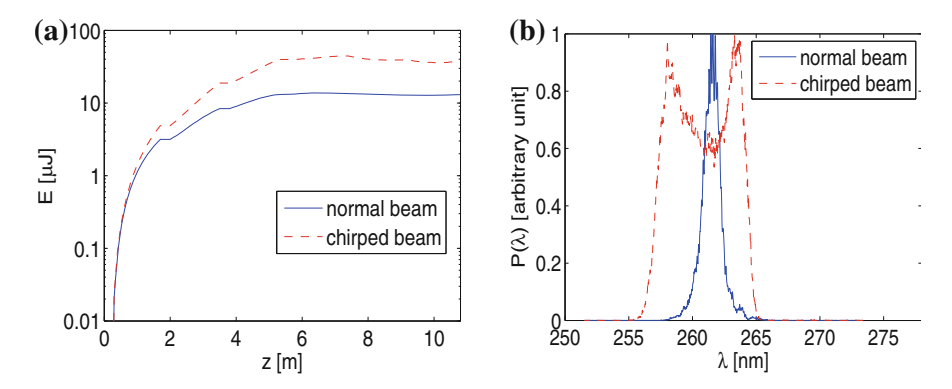


Fig. 3.34 FEL performance for normal electron beam and chirped electron beam: **a** Radiation energy as a function of the radiator undulator length; **b** spectra at saturation. (Reprinted from Ref. [27], Copyright 2012, with permission from Elsevier)

the normal beam case and about 44.3 µJ for the chirped beam case. The difference of the output pulse energies is mainly caused by the different gain bandwidths of the radiator for these two cases: the gain bandwidth of the radiator for the normal beam case is much narrower than that of the chirped beam case. As shown in Fig. 3.34b, the spectrum bandwidth of the radiation pulse generated by the normal electron beam is about 0.53 %, which means that only the FEL frequency within the gain bandwidth of the radiator can be amplified to saturation. For the chirped electron beam case, the bandwidth of the radiation pulse is about 2.7 %, which is even broader than that of the seed laser. So nearly the whole electron beam can be used for FEL generation. In particular, there is a pronounced dip near the center of the FEL output spectrum. This is mainly caused by the large energy spread in the central part of the electron bunch from laser modulation. As a result, the FEL emission from the central part is significantly attenuated, creating a dip in the spectrum due to the linear chirp (the spectrum correlates with time). The Wigner distribution of the radiation pulse at saturation is shown in Fig. 3.35a. The linear frequency chirp in the seed laser is well maintained and this kind of laser pulse can be easily compressed by the optical pulse compressor, as Fig. 3.35b shows.

Figure 3.36 gives a comparison of the radiation pulse temporal profiles before and after the compressor without energy loss. The compressed pulse has a tail in the left part which is mainly cause by the quadratic component of the beam energy chirp. The pulse length is compressed by about 110 times, from 3.5 ps to 31 fs, and the peak power is accordingly enhanced by about 100 times, from 12 MW to 1.2 GW. Assuming that the diffraction efficiency of one reflective grating is around 70 %, which is commercially available, the transfer efficiency of the compressor will be around 24 %. So we can estimate that the output peak power of CPA-HGHG at 262 nm is about 280 MW. As the pulse duration of the seed laser before stretch is 82 fs, the minimal pulse duration of the 3rd harmonic radiation is about 2.6 times

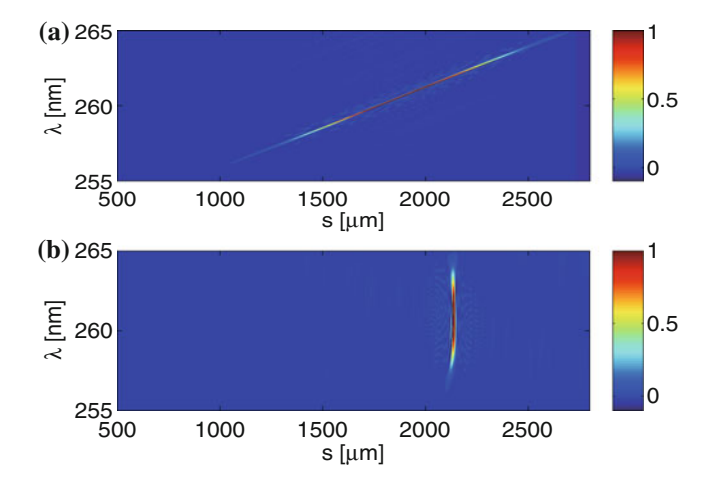


Fig. 3.35 Wigner distributions of the output radiation pulses before (a) and after (b) the optical compressor. (Reprinted from Ref. [27], Copyright 2012, with permission from Elsevier)

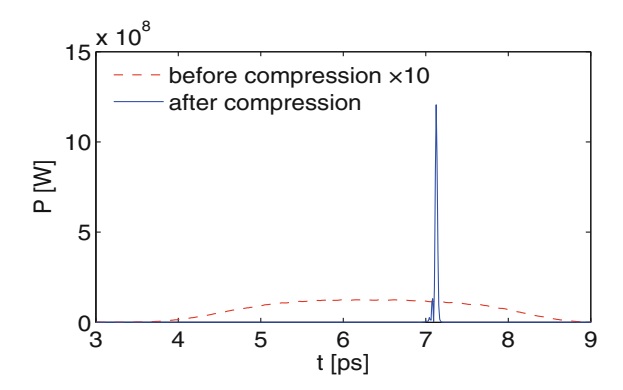
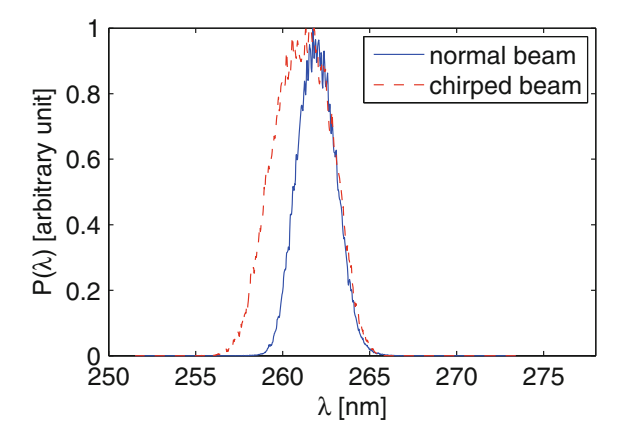


Fig. 3.36 A comparison of the output radiation pulses before and after compressor. The power of the radiation pulse before compression is multiplied by a factor of 10. (Reprinted from Ref. [27], Copyright 2012, with permission from Elsevier)

shorter than that of the seed laser, which is close to the theoretical prediction of Eq. (3.45).

When the FEL works in the CHG regime, the gain bandwidth of the radiator is much broader. For our case, we take the first undulator segment of radiator for the CHG experiment. The gain bandwidth is about 1/60, which is a little narrower than the bandwidth of the seed laser. The spectra of the radiation pulses generated by the CHG process for the two cases (normal beam with flat energy and the beam with energy chirp) are shown in Fig. 3.37. The shift of the central wavelength for the chirped beam case is caused by the negative energy chirp that compresses the laser

Fig. 3.37 Spectra of the radiation pulses generated by CHG for normal electron beam case and chirped electron beam case. (Reprinted from Ref. [27], Copyright 2012, with permission from Elsevier)



modulation after beam goes through the chicane. The spectrum bandwidth of the radiation pulse generated by the normal electron beam and the chirped beam is about 1 % and 1.5 %, respectively. The Wigner distributions of the output radiation pulses generated by the normal electron beam before and after compression are shown in Fig. 3.38a, b. Figure 3.38c shows a comparison of the longitudinal profiles of these two pulses. The peak power of the radiation pulse is increased from 1.8 MW to about 67 MW. Considering the transfer efficiency of the grating, the output peak power of CPA-CHG will approach 16 MW when the pulse compressor has a 76 % loss. The pulse duration is compressed by about 35 times, from 3.3 ps to 94 fs.

It is worth mentioning that the CHG scheme has been widely adopted in storage ring (SR) for the generation of femtosecond coherent radiation pulses in the ultraviolet region [33]. It has been proposed that the CHG scheme also has the potential of generating coherent x-ray radiation [34]. However, the radiation power of a CHG device is relatively low due to the low current of the electron beam used in SR. The CPA technique may be an effective way to enhance the output power of a CHG and can be used to generate ultra-short XUV radiation pulses based on SR.

3.7 Slippage Effect on Energy Modulation in Seeded FELs

Several seeded FEL operation schemes have been proposed in previous sections for various purposes. It is anticipated that the output radiation from a seeded FEL should inherit the properties of the seed laser with its bandwidth close to the Fourier transform-limit. However, there are several challenges in implementing seeding schemes at extremely high harmonics. For example, too large initial energy spread will constrain the possibility of working at high harmonic number for a single stage. The jitter of the central beam energy will result in a large fluctuation of the shot-to-shot output pulse energy. The non-uniform distributions of the local

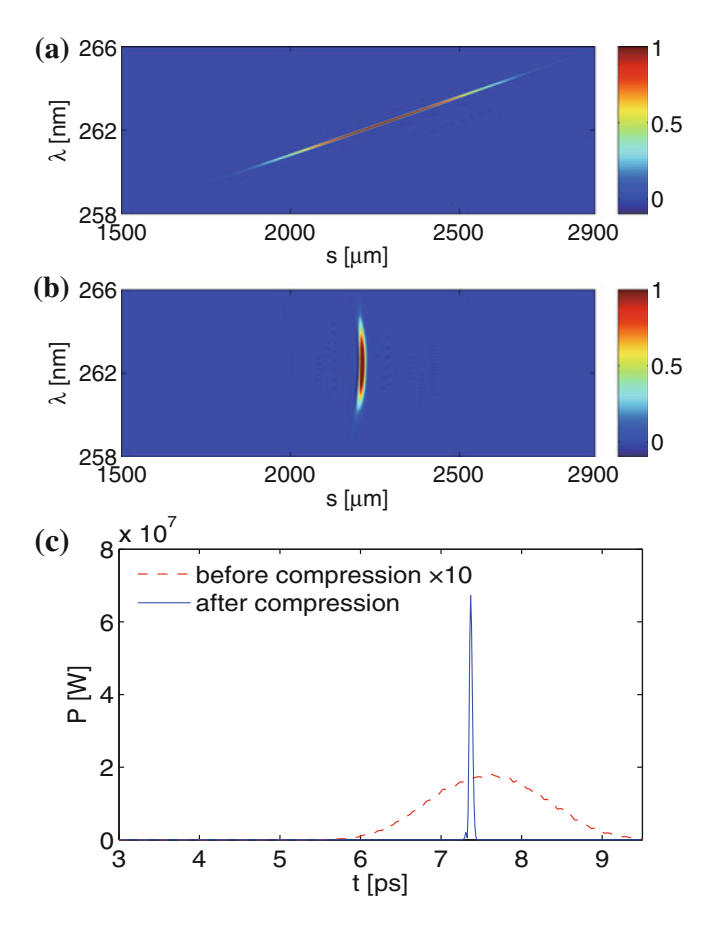


Fig. 3.38 Wigner distributions of the output radiation pulses generated by CHG before (a) and after (b) the optical compressor. **c** A comparison of the output radiation pulses before and after compressor. The power of the radiation pulse before compression is multiplied by a factor of 10. (Reprinted from Ref. [27], Copyright 2012, with permission from Elsevier)

parameters will affect the longitudinal profile of the radiation pulse, which may degrade the coherence of the output radiation. In particular, the initial insignificant errors compared to the seed wavelength may be amplified by the harmonic up-conversion process and will become large relative to a much shorter wavelength. For example, the electron beam shot noise will be amplified by n^2 , which may overwhelm the external seeding source [35]. More recently, attentions have been turned to errors from the imperfection of the seed laser. It has been pointed out that if there is a frequency chirp in the seed pulse, the chirp in the electron micro-bunching turns out to be roughly multiplied by the harmonic number n [36]. As a result, generation of nearly transform-limited radiation at 1 nm wavelength from a commercial 800 nm Ti:sapphire seed laser requires that the extra

time-bandwidth product contributed by the seed phase chirp should be no more than one in a million of the ideal seed pulse, which is well beyond the state-of-the-art laser technology.

The conclusions in Ref. [36] were drawn under the assumption that the phase of the energy modulation directly copies the phase of the seed laser after the modulator. The seed power and frequency variations as a function of time due to the slippage effect in the modulator were neglected. This assumption is reasonable in the case of using an ideal seed laser with infinite pulse length and flat spectral phase distribution. However, for a realistic seed laser pulse with finite duration, the slippage effect on the energy modulation should be considered, especially for the case when the laser pulse width is comparable to the slippage length in the modulator.

As the continuous progress in laser technologies have made ultra-short and high intensity laser pulses available, many seeded FEL facilities now adopt short seed laser pulses. For instance, the seed pulse duration of the FERMI seeded FEL is around 150 fs (FWHM) [37], and the Shanghai deep ultraviolet FEL uses an ultra-short seed pulse of about 80 fs (FWHM). However, the temporal and spatial quality of the laser beam will be degraded due to the propagation process, non-linear effects or inhomogeneous doping concentration in the amplifying media of the CPA system. In this section, a new model that considers the slippage effect in the modulator is developed to describe the energy modulation with a frequency chirped seed laser pulse. It is found that the frequency chirp induced by the seed laser can be smoothed by the slippage effect, when the slippage length in the modulator is comparable to the pulse length of the seed laser. For ultra-short UV seed lasers with FWHM pulse length around 16 fs, this condition is generally met with a modulator with ~ 30 undulator periods. For longer seed laser pulses with FWHM pulse length around 80 fs, we propose using a modulator tuned at the sub-harmonic of the UV seed laser to boost the slippage length to a similar level as the laser width. Three-dimensional simulations have been carried out for a soft x-ray facility based on seeded FEL schemes to illustrate how the sensitivity of the FEL bandwidth to the initial frequency chirp can be significantly reduced by a proper design of the modulator. Our studies show that the tolerance on laser frequency chirp for generating nearly transform-limited soft x-ray pulses in seeded FELs is much looser than that suggested in [36] and fully coherent radiation at nanometer wavelength may be reached with current technologies.

3.7.1 Energy Modulation with Slippage Effect

Here we consider a planar undulator with a sinusoidal magnetic field in the vertical direction and a period length λ_u . In the laboratory frame, the undulator magnetic field of the modulator is

$$\vec{B}_{y} = B_0 \sin(k_u z) \vec{y} \tag{3.47}$$

The orbit of a relativistic electron in such a field is approximately a sine wave, and the velocity of the electron is given by

$$\vec{v}(t) = v_z(t)\vec{z} - \frac{Kc}{\gamma}\cos(\omega_u t)\vec{x}$$
 (3.48)

The electron's transverse velocity induced by the undulator magnet is

$$v_x(t) = -\frac{Kc}{\gamma}\cos(\omega_u t) \tag{3.49}$$

Since the average velocity of the electron is approximately constant, v_z can be calculated by

$$v_z(t) = c\sqrt{1 - 1/\gamma^2 - K^2 \cos^2(\omega_u t)/\gamma^2} \approx c - \frac{1 + K^2/2}{2\gamma^2}c - \frac{K^2 c}{4\gamma^2}\cos(2\omega_u t)$$
(3.50)

and the average electron longitudinal velocity is

$$\bar{v}_z \approx c \left(1 - \frac{1 + K^2/2}{2\gamma^2} \right) \tag{3.51}$$

Assuming a seed laser pulse with a Gaussian power distribution of rms width σ_s , central wavelength at λ_s and a linear frequency chirp α . The electric field distribution along the electron beam can be represented as

$$E(s) = E_0 e^{-s^2/4\sigma_s^2} e^{i(k_s s + \alpha s^2 + \phi_0)}$$
(3.52)

where s is the position along the electron bunch, E_0 is the peak electric field of the seed laser, $k_s = 2\pi/\lambda_s$ is the wave number of the seed laser and ϕ_0 is the initial carrier envelope phase of the laser. According to the resonant condition, the radiation overtakes the electron beam by one radiation wavelength per undulator period, which is called the slippage effect. Considering the slippage effect, the electric field and frequency distribution of the seed laser will vary with time, and Eq. (3.52) should be re-written as

$$E(s,t) = E_0 e^{-[s-p(t)]^2/4\sigma_s^2} e^{i\{k_s[s-p(t)] + \alpha[s-p(t)]^2 + \phi_0\}}$$
(3.53)

where $p(t) = (c - \bar{v}_z)t$ is the relative position of the seed pulse with respect to the electron beam. In a planar undulator, the electron has transverse wiggling motion and the longitudinal "figure-eight" oscillation. Such a trajectory gives rise to energy

exchange between the electron and the laser electric field. The energy change of the electron can be calculated by

$$\gamma(s,t) = \frac{e}{mc^2}E(s,t) \cdot v_x(t)$$
 (3.54)

Integrating Eq. (3.54) with respect to t, we arrive at an expression for the energy modulation along the electron bunch after passing through the modulator:

$$\gamma(s) = \int_{0}^{L_{\text{mod}}/c} \frac{e}{mc^2} E(s, t) \cdot v_x(t) dt$$
 (3.55)

where L_{mod} is the length of the modulator.

When using of an ultra-short seed pulse with the pulse length σ_s comparable with the slippage length $N\lambda_s$ in the modulator, where N is the period number of the modulator, part of the electron beam will be slipped over by the whole seed pulse and interacts with each cycle of the seed laser. So the energy modulation amplitude and the phase of the energy modulation will be averaged by the whole seed laser instead of directly copying the seed pulse.

Figure 3.39 shows the energy modulation properties when using an ultra-short seed laser with FWHM pulse length of $3\lambda_s$ and a relatively large frequency chirp $\alpha = 0.16/\lambda_s^2$. The period number of the modulator is N = 20. For comparison of different models, we use Eq. (3.55) to calculate energy modulation with and without slippage effect, respectively. It is found that the slippage effect creates a uniform region (UR) in the energy modulation, where the energy modulation amplitude and phase distributions are nearly flat. Figure 3.39b gives the phase distributions of the seed laser and energy modulations along the electron bunch. When the slippage effect is neglected, the energy modulation has quadratic phase that directly copies

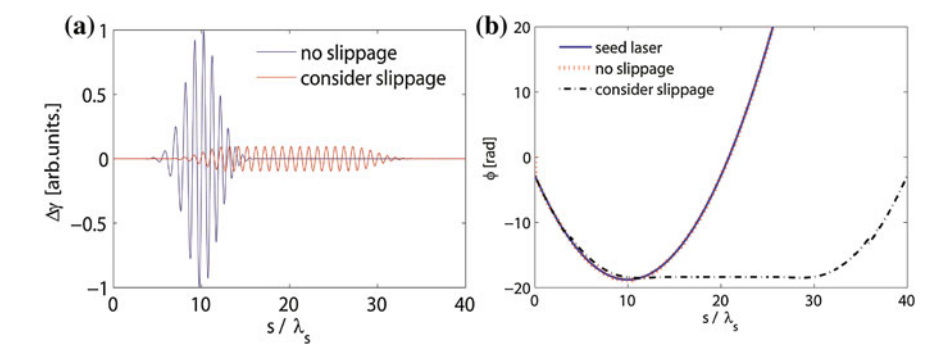


Fig. 3.39 Comparation of the energy modulations with and without slippage effects: **a** The beam energy distributions. **b** The longitudinal phase distributions of the energy modulations. (Reprinted with permission from Ref. [38]. Copyright 1998 by American Physical Society)

the spectral phase of the linear chirped in the seed laser. With the slippage effect taken into account, the spectral phase distribution is nearly flat in the central part.

To fully characterize the energy modulation in both the time and frequency domains and compare it with the seed laser pulse, we show the Wigner distributions of the seed laser pulse and the energy modulations with different N in Fig. 3.40. Figure 3.40a gives the Wigner distribution of the seed laser pulse, where a considerable linear frequency chirp is clearly seen. When N=1, a linear chirp appears in the energy modulation as shown in Fig. 3.40b. This chirp is significantly reduced in the central part when N=10 (Fig. 3.40c). Meanwhile, the duration of the energy modulation with constant frequency begins to increase as the modulator length increases (Fig. 3.40d), which creates a UR with quite flat spectral phase. From Fig. 3.40c, d, one can find that with the slippage length longer than or comparable to the laser pulse width, the initial seed laser frequency chirp only leads to chirp in the lateral parts of the energy modulation. Note, with the modulation amplitudes in the lateral parts much smaller than that of the central part, the bunching at high

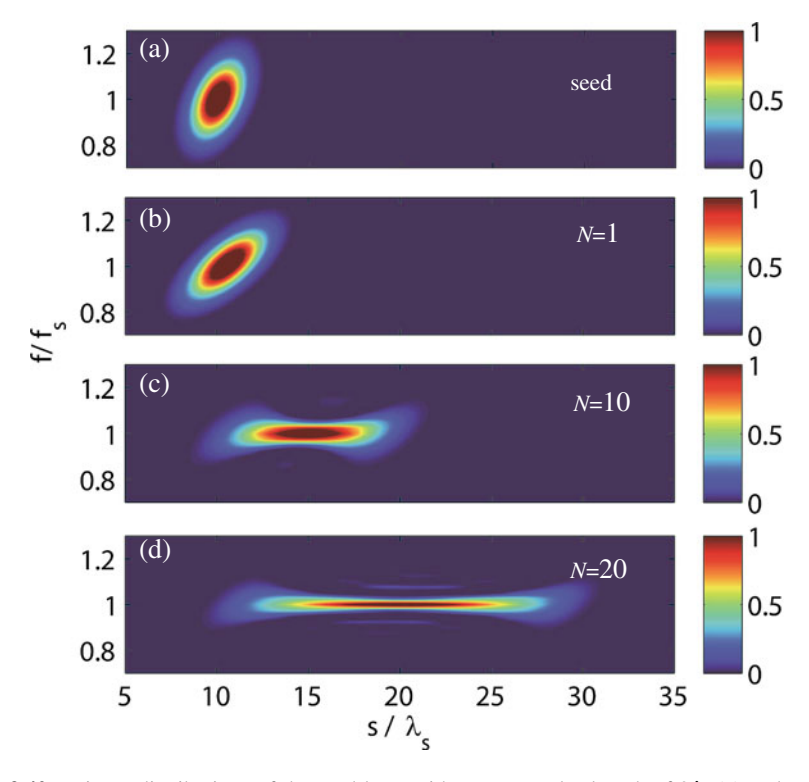


Fig. 3.40 Wigner distributions of the seed laser with FWHM pulse length of $3\lambda_s$ (a) and energy modulations (b-d) for different period numbers of the modulator (N=1,10,20). The frequency chirp in the seed laser pulse is $\alpha=0.16/\lambda_s^2$. (Reprinted with permission from Ref. [38]. Copyright 1998 by American Physical Society)

harmonics would be negligible at these lateral regions. Therefore, the frequency chirp in the lateral parts will not significantly affect the final radiation bandwidth.

3.7.2 HGHG and EEHG with Short Seed Laser Pulses

For the HGHG scheme, here we consider an ideal beam with constant energy and current, assuming an initial Gaussian beam energy distribution with an average energy of γ_0 and rms energy spread σ_{γ} , the initial longitudinal phase space distribution can be written as

$$f_0(p) = \frac{N_0}{\sqrt{2\pi}} e^{-\frac{p^2}{2}} \tag{3.56}$$

After interacting with the seed laser pulse, the electron energy is changed to p + A(s), where $A(s) = \gamma(s)/\sigma_{\gamma}$ is the energy modulation amplitude, and the distribution function becomes

$$f_1(p,s) = \frac{N_0}{\sqrt{2\pi}} \exp\{-[p - A(s)]^2/2\}$$
 (3.57)

Sending then the electron beam through the DS with normalized strength $B = k_s R_{56} \sigma_{\gamma}/\gamma_0$ converts the longitudinal coordinate to $s + Bp/k_s$, and makes the final distribution function

$$f_{HGHG}(p,s) = \frac{N_0}{\sqrt{2\pi}} \exp\{-[p - A(k_s s - Bp)]^2/2\}$$
 (3.58)

Then the kth local bunching factor at position s can be written as

$$b(s,k) = \frac{1}{\sqrt{2\pi}} \int_{s-l/2}^{s+l/2} ds \int_{-\infty}^{\infty} \exp(-ikk_s s) \exp\{-[p - A(k_s s - Bp)]^2 / 2\} dp / l$$
(3.59)

where l is the length of the chosen part of the electron beam.

Figure 3.41 shows the Wigner distributions of the seed laser, bunching factors at fundamental and 10th harmonic of the seed. The fundamental bunching inherits the frequency distribution of the energy modulation and has frequency chirps at lateral parts of the bunching pulse, where the bunching factor is much smaller than the central part. For the 10th harmonic, sufficient bunching only appears in the region with relatively large energy modulation amplitude, where the phase distribution is

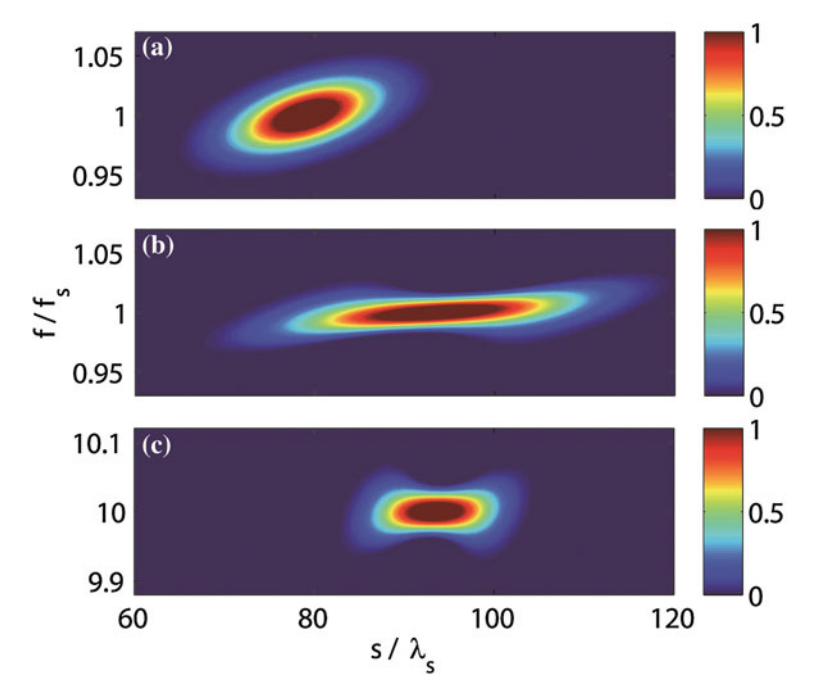


Fig. 3.41 Wigner distributions of the seed laser with FWHM pulse length of $17\lambda_s$ (a) and local bunching factor at fundamental (b) and 10th harmonic (c) of the seed. The frequency chirp in the seed laser pulse is $\alpha = 0.006/\lambda_s^2$. (Reprinted with permission from Ref. [38]. Copyright 1998 by American Physical Society)

quite flat. So this slippage effect prevents the initial seed laser frequency chirp from broadening the final bandwidth of the high harmonic radiation.

Generally, the coherence property of the radiation could be quantified by the time-bandwidth product (TBP) factor, which can be simply defined as

$$T = \Delta k \Delta \tau \tag{3.60}$$

T has minimal value T_L for a transform-limited pulse and will grow as the phase error increases. Figure 3.42 gives the spectra of the electron bunching factors at 10th harmonic of the seed. The period number of the modulator is chosen to be N=30 to make the TBP reach its minimal value. For convenience of comparison, four cases have been considered: flat phase and quadratic phase with and without slippage effect. It is found that the bandwidth of the spectral bunching for the quadratic phase case is about $3\times$ broader than that of the flat phase case when the slippage effect is neglected. However, the spectra are nearly the same for the flat and quadratic phase cases when the slippage effect is considered, which implies that the frequency chirp in an ultra-short seed pulse may not significantly impact the

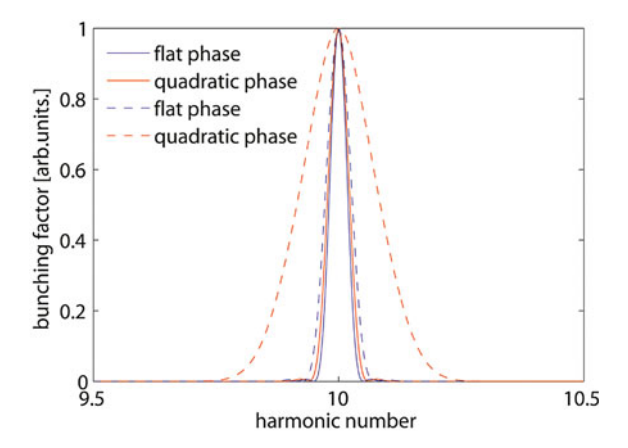


Fig. 3.42 Bunching factor spectra for different cases: seed laser with flat phase and considering the slippage effect (*blue solid line*); seed laser with quadratic phase and considering the slippage effect (*red solid line*); seed laser with flat phase and ignoring the slippage effect (*blue dashed line*); seed laser with quadratic phase and ignoring the slippage effect (*red dashed line*). (Reprinted with permission from Ref. [38]. Copyright 1998 by American Physical Society)

electron bunching for HGHG with properly chosen period number of the modulator.

The EEHG seeding mechanism shares many similarities with HGHG. The final electron beam distribution function after the second DS of the EEHG can be written as

$$f_{EEHG}(p,s) = \frac{N_0}{\sqrt{2\pi}} \exp\{-[p - A_2(k_s s - B_2 p) - A_1 \sin[(k_s s - B_1 p - B_2 p) + B_1 A_2(k_s s - B_2 p)]^2 / 2\}$$
(3.61)

where $A_2(s) = \gamma(s)/\sigma_{\gamma}$, and the local bunching factor distribution for EEHG is

$$b(k,s) = \frac{1}{\sqrt{2\pi}} \int_{s-l/2}^{s+l/2} ds \int_{-\infty}^{\infty} \exp(-ikk_s s) \exp\{-[p - A_2(k_s s - B_2 p) - A_1 \sin(k_s s - B_1 p - B_2 p) + B_1 A_2(k_s s - B_2 p)]^2 / 2 dp / l$$
(3.62)

We assume that the energy modulation amplitudes for the two stages are $A_1 = 3$, $A_{2m} = 2$, where A_{2m} is the maximal value of A_2 , and the length of each slice is equal to the seed wavelength, $l = \lambda_s$. The properties of the second seed pulse are the same as that used in the HGHG case. Figure 3.43 shows the local bunching factor distribution along the electron bunch for different harmonic numbers. As the

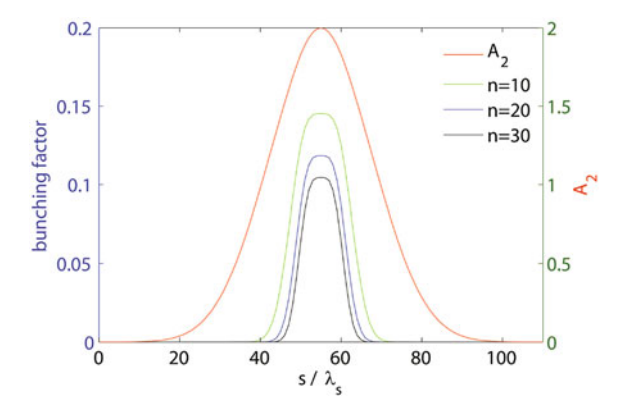


Fig. 3.43 Local bunching factor distributions along the electron beam for different harmonics of the seed (n = 10, 20 and 30). (Reprinted with permission from Ref. [38]. Copyright 1998 by American Physical Society)

bunching factor is very sensitive to the energy modulation amplitude at high harmonics, the bunching distributions has sharp edges at lateral parts of the energy modulation.

3.7.3 3D Simulations for SXFEL

To verify the theoretical results in previous sections, we have carried out 3D simulations using GENESIS based on the nominal parameters of the SXFEL project. The SXFEL test facility aims at generating 8.8 nm FEL from a 264 nm conventional seed laser through a two-stage cascaded HGHG or a single stage EEHG configuration. The electron beam energy is 840 MeV with emittance of 1 mm-mrad and slice energy spread of about 84 keV. The beam peak current is 600 A.

For cascaded HGHG operation, the test facility converts the seed laser at wavelength $\lambda_{seed}=264\,\mathrm{nm}$ to the FEL at 44 nm with the first stage HGHG, and it is followed by the second HGHG stage to produce the 8.8 nm soft x-ray radiation. Here we only consider the first stage HGHG with harmonic up-conversion number of 6. We assume the pulse length of the seed laser is 16 fs (FWHM), and the period number of the modulator is 30. For comparison purpose, seed lasers with flat and quadratic spectral phase (linear chirp) distributions have been considered. For the quadratic phase case, we set $\alpha=0.006/\lambda_s^2$, which makes TBP of the seed pulse 1.6 times larger than that of a transform-limited pulse with the same pulse length. According to Ref. [36], the TBPs of the output radiations should be 2.4 and 4.7 times larger than that of transform-limited pulses for 6th and 30th harmonics when ignoring the slippage effect.

The resonant wavelength of the radiator in the first stage of SXFEL is flexible, so we can make the radiator resonant at the fundamental and 6th harmonic of the seed. The Wigner distributions of the fundamental (264 nm) and 6th harmonic (44 nm) radiations at the very beginning of the radiator for the quadratic phase case are shown in Fig. 3.44. As the FEL works in the CHG regime, the radiation power is proportional to the square of the bunching factor. One can clearly see that the frequency chirps occur in the lateral parts of the radiation pulses. As the central part of the radiation pulse with large power has flat phase distribution, the spectrum of the radiation for the quadratic phase case will have little difference from the flat phase case. Figure 3.45 shows the FEL performance of the 6th harmonic radiation. It is found that the gain curves and spectra for these two cases are nearly the same. The bandwidths of the radiation pulses at saturation are both around 0.2 %, which indicates that the initial frequency chirp in the seed laser does not lead to broadening of the bandwidth of the harmonic radiation of HGHG.

For EEHG operation, we assume that the first seed laser pulse is longer than the electron bunch. The properties of the second seed laser are chosen to be the same as that used in HGHG simulations. The period numbers of the two modulators are both 30. The energy modulation amplitudes and dispersion strengths in our simulation are set to be $A_1 = 3.5, A_2 = 4, B_1 = 8.86, B_2 = 0.28$ to maximize the bunching factor at 30th harmonic of the seed. The corresponding seed laser peak powers are 40 MW and 80 MW, respectively. The performance of the radiation also has a very weak dependence on the chirp in the seed laser, as shown in Fig. 3.46. The bandwidths of the radiation pulses at saturation are also around 0.2 %.

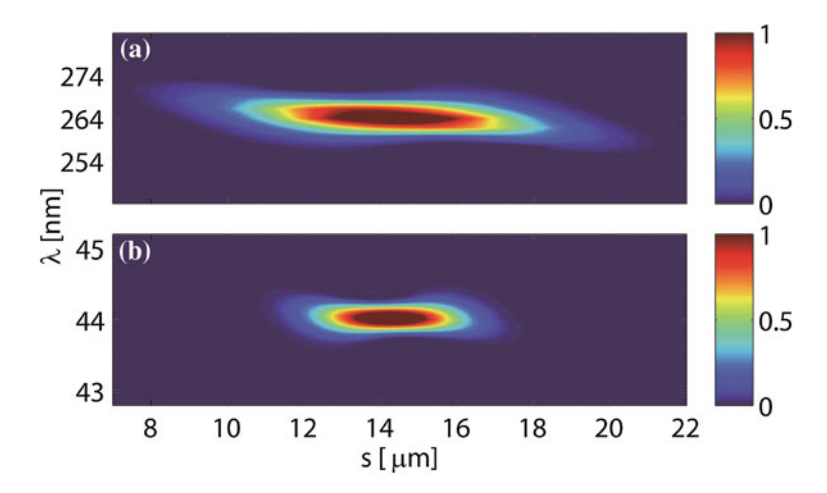


Fig. 3.44 Wigner distributions of coherent harmonic radiation at fundamental (a) and 6th harmonic (b) of the seed. The FWHM pulse length of the seed laser is 16 fs. The frequency chirp in the seed laser pulse is $\alpha = 0.006/\lambda_s^2$. (Reprinted with permission from Ref. [38]. Copyright 1998 by American Physical Society)

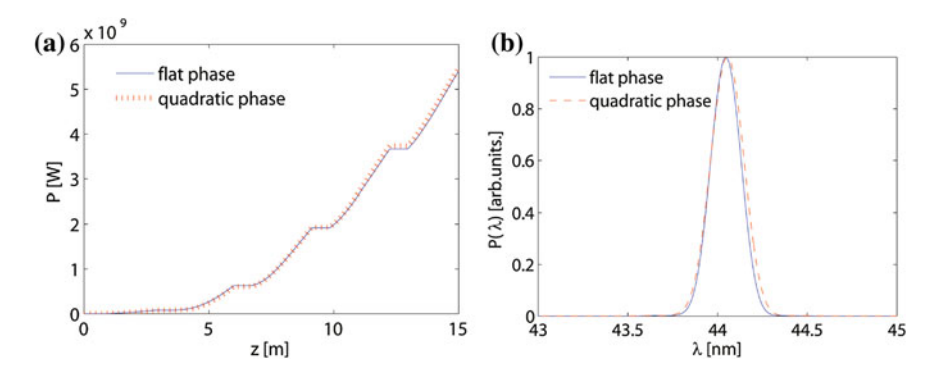


Fig. 3.45 6th harmonic radiation performances of HGHG for the 16 fs seed laser pulses with flat phase (*blue line*) and quadratic phase (*red dashed line*): a FEL gain curves; b spectra at saturation. (Reprinted with permission from Ref. [38]. Copyright 1998 by American Physical Society)

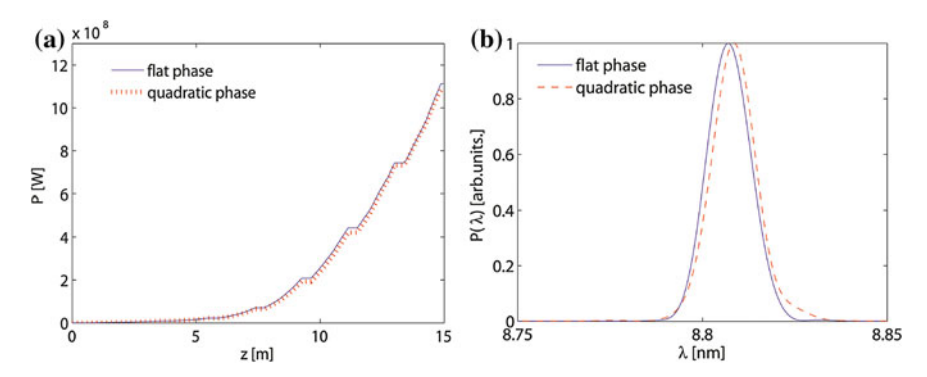


Fig. 3.46 30th harmonic radiation performances of EEHG for the 16 fs seed laser pulses with flat phase (*blue line*) and quadratic phase (*red dashed line*): **a** FEL gain curves; **b** spectra at saturation. (Reprinted with permission from Ref. [38]. Copyright 1998 by American Physical Society)

3.7.4 Slippage-Boosted by a Sub-harmonic Modulator

In the previous simulations, we have shown that nearly transform-limited high harmonic radiation pulses can be generated via seeded FELs, when the slippage length in the modulator is comparable to the pulse length of the seed laser. For a 16 fs seed laser pulse at 264 nm, the optimized period number is about 30, which is a reasonable value for modulators design. However, when using a longer seed laser pulse for the generation of narrower bandwidth radiation, this period number is not large enough to compensate the initial frequency chirp induced by the seed. Figure 3.47 shows the simulated spectra of the 30th harmonic radiations of EEHG with 80 fs (FWHM) seed laser pulses. The frequency chirp in the seed laser pulse is $\alpha = 0.0006/\lambda_e^2$ for the quadratic phase case, which makes TBP of the seed

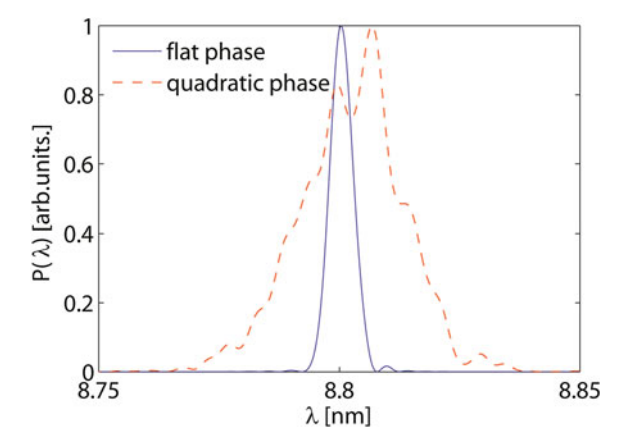


Fig. 3.47 Spectra of 30th harmonic radiation pulses of EEHG for the 80 fs seed laser pulses with flat phase (*blue solid line*) and quadratic phase (*red dashed line*). (Reprinted with permission from Ref. [38]. Copyright 1998 by American Physical Society)

pulse $3\times$ larger than that of a transform-limited pulse with the same pulse length. The period number of the modulator is set to be 22 here. Other parameters are the same as that used in the previous section. It is found from Fig. 3.47 that the bandwidth of the 30th harmonic radiation for the quadratic phase case is about 4.5 times broader than that of the flat phase case. Although the TBP of the radiation pulse has already been reduced by the modulator with 22 periods, the period number still needs to be further increased by about 5 times to fully compensate the frequency chirp induced by the seed laser. However, when the period number is too large, e.g. larger than 50 for SXFEL, the modulator will no longer work in the small-gain regime. In this case, the FEL interaction tends to wash out the fine structures in energy space and will lead to a significant degradation to the quality of the electron bunch.

Here, we propose using a sub-harmonic modulator to boost the slippage effect. Instead of resonant at the fundamental of the seed, the modulator is tuned to an odd sub-harmonic: $\lambda_m = m\lambda_s$, $m = 3, 5, 7, \ldots$, which will increase the slippage length by m times in the modulator while simultaneously keeping the FEL interaction in the small-gain regime.

Here we make the second modulator of EEHG resonant at 1320 nm, which is 5 times longer than the seed wavelength. The peak power of the second seed laser is increased to 180 MW to generate the same energy modulation amplitude ($A_2 = 4$) as we have used in the last section. Figure 3.48 shows Wigner distributions of 30th harmonic radiation pulses at very beginning of the radiator for flat and quadratic phase cases. One can find that there are no chirps in the radiation for both these two cases, which implies that the initial chirp in the seed laser has been compensated by the sub-harmonic modulator. Figure 3.49 gives the FEL performance for these two cases. The output peak powers are at the same level. The bandwidths of the radiation pulses at saturation are both around 0.05 %, which is about 4 times narrower than the output bandwidth of the normal EEHG with a 16 fs seed laser pulse

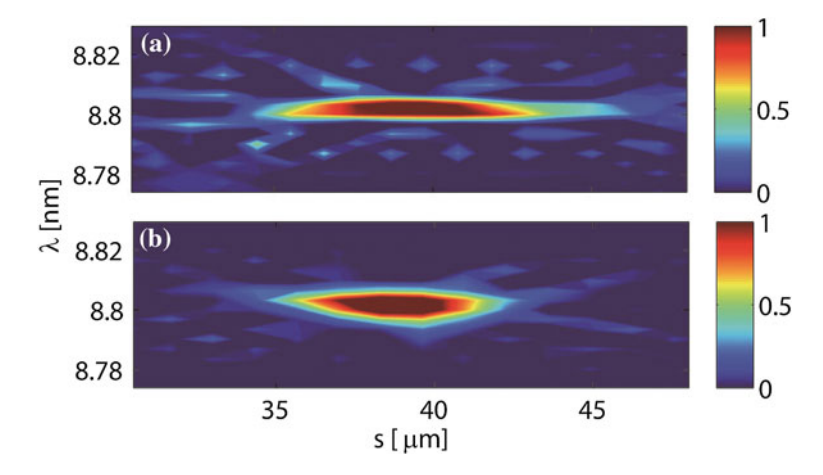


Fig. 3.48 Wigner distributions of 30th harmonic radiation pulses at the very beginning of the radiator of EEHG for the 80 fs seed laser pulses with flat phase (**a**) and quadratic phase (**b**). (Reprinted with permission from Ref. [38]. Copyright 1998 by American Physical Society)

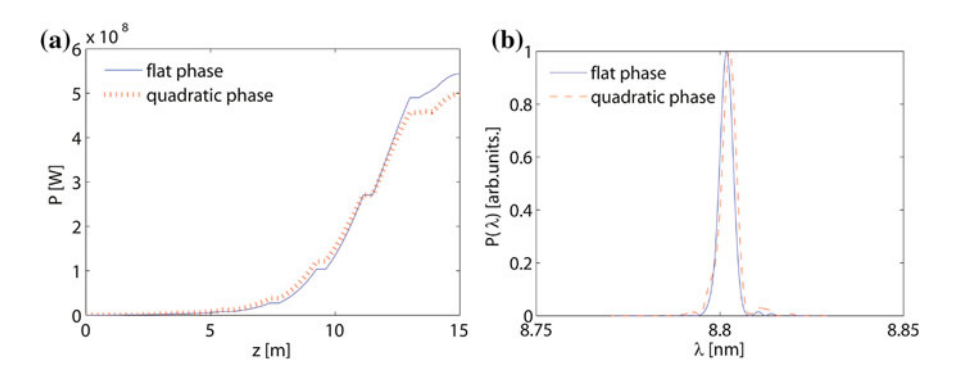


Fig. 3.49 30th harmonic radiation performances of EEHG with sub-harmonic modulator resonant at 1320 nm for the 80 fs seed laser pulses with flat phase (*blue line*) and quadratic phase (*red dashed line*): **a** FEL gain curves; **b** spectra at saturation. (Reprinted with permission from Ref. [38]. Copyright 1998 by American Physical Society)

References

- Deng HX, Dai ZM (2010) Ultra-high order harmonic generation via a free electron laser mechanism. Chin Phys C 34(8):1140
- McNeil BWJ, Robb GRM, Poole MW (2005) Proceedings of 2005 particle accelerator conference (PAC2005), Knoxville, Tennessee, May 2005, p 1718
- 3. Allaria E, De Ninno G (2007) Soft-X-ray coherent radiation using a single-cascade free-electron laser. Phys Rev Lett 99(1):014801
- Jia Q (2008) Enhanced high-gain harmonic generation for x-ray free-electron laser. Appl Phys Lett 93(14):141102

References 75

 Xiang D, Stupakov G (2011) Triple modulator-chicane scheme for seeding sub-nanometer x-ray free-electron lasers. New J Phys 13(9):093028

- Feng C, Zhao Z (2010) Hard X-ray free-electron laser based on echo-enabled staged harmonic generation scheme. Chin Sci Bull 55(3):221–227
- 7. Yu LH (1991) Generation of intense UV radiation by subharmonically seeded single-pass free-electron lasers. Phys Rev A 44(8):5178–5193
- 8. Coisson R, MartiniF D (1982) Free electron coherent relativistic scatterer for U.V. generation. Phys Quant Electron 9:939–960
- Reiche S (1999) GENESIS 1.3: a fully 3D time-dependent FEL simulation code. Nucl Instr Methods Phys Res Sect A: Accel Spectrom Detect Assoc Equip 429(1): 243.248
- Huang Z, Ding Y, Schroeder CB (2012) Compact X-ray free-electron laser from a laser-plasma accelerator using a transverse-gradient undulator. Phys Rev Lett 109(20):204801
- 11. Deng H, Feng C (2013) Using off-resonance laser modulation for beam-energy-spread cooling in generation of short-wavelength radiation. Phys Rev Lett 111(8):084801
- 12. Feng C, Deng H, Wang D, Zhao Z (2014) Phase-merging enhanced harmonic generation free-electron laser. New J Phys 16(4):043021
- Feng C, Zhang T, Deng H, Zhao Z (2014) Three-dimensional manipulation of electron beam phase space for seeding soft x-ray free-electron lasers. Phys Rev Spec Top-Accel Beams 17(7):070701
- Floettmann K (1999) ASTRA User's Manual. http://www.desy.de/mpyflo/ Astra_dokumentation
- 15. Borland M (2001) Simple method for particle tracking with coherent synchrotron radiation. Phys Rev Spec Top-Accel Beams 4(7):070701
- Johnsson P, López-Martens R, Kazamias S et al (2005) Attosecond electron wave packet dynamics in strong laser fields. Phys Rev Lett 95(1):013001
- 17. Remetter T, Johnsson P, Mauritsson J et al (2006) Attosecond electron wave packet interferometry. Nat Phys 2(5):323.326
- 18. Swoboda M, Fordell T, Klünder K et al (2010) Phase measurement of resonant two-photon ionization in helium. Phys Rev Lett 104(10):103003
- Thompson NR, McNeil BWJ (2008) Mode locking in a free-electron laser amplifier. Phys Rev Lett 100(20):203901
- Feng C, Chen J, Zhao Z (2012) Generating stable attosecond x-ray pulse trains with a mode-locked seeded free-electron laser. Phys Rev Spec Top-Accel Beams 15(8):080703
- 21. Maine P, Strickland D, Bado P et al (1988) Generation of ultrahigh peak power pulses by chirped pulse amplification. IEEE J Quantum Electron 24(2):398–403
- 22. Wu J, Murphy JB, Emma P et al (2007) Interplay of the chirps and chirped pulse compression in a high-gain seeded free-electron laser. JOSA B 24(3):484–495
- 23. Li Y, Lewellen J, Huang Z et al (2002) Time-resolved phase measurement of a self-amplified free-electron laser. Phys Rev Lett 89(23):234801
- Yu LH, Johnson E, Li D et al (1994) Femtosecond free-electron laser by chirped pulse amplification. Phys Rev E 49(5):4480–4486
- Yu LH, Shaftan T, Liu D et al (2006) Chirped pulse amplification experiment at 800 nm. In: The 28th International free electron laser conference (FEL 2006), Berlin, Germany, Aug 2006, JACoW, p 194
- Doyuran A, DiMauro L, Graves W et al (2004) Chirped pulse amplification of HGHG-FEL at DUV-FEL facility at BNL. Nucl Instrum Methods Phys Res, Sect A 528(1):467–470
- Feng C, Shen L, Zhang M, Wang D, Zhao Z, Xiang D (2013) Chirped pulse amplification in a seeded free-electron laser for generating high-power ultra-short radiation. Nucl Instrum Methods Phys Res, Sect A 712(113):119
- 28. Born M, Wolf E (1999) Principles of optics: electromagnetic theory of propagation, interference and diffraction of light. Cambridge university press, New York, p 486
- 29. Wigner E (1932) On the quantum correction for thermodynamic equilibrium. Phys Rev 40(5):749–759

- 30. Bastiaans MJ (1989) Propagation laws for the second-order moments of the Wigner distribution function in first-order optical systems. Optik 82(4):173–181
- 31. Kohler B, Squier J, DeLong K W et al (1995) Phase and intensity characterization of femtosecond pulses from a chirped-pulse amplifier by frequency-resolved optical gating. Opt Lett 20(5): 483–485
- 32. Dorrer C, De Beauvoir B, Le Blanc C et al (1999) Single-shot real-time characterization of chirped-pulse amplification systems by spectral phase interferometry for direct electric-field reconstruction. Opt Lett 24(22):1644–1646
- 33. De Ninno G, Allaria E, Coreno M et al (2008) Generation of ultrashort coherent vacuum ultraviolet pulses using electron storage rings: a new bright light source for experiments. Phys Rev Lett 101(5):053902
- 34. Xiang D, Wan W (2010) Generating ultrashort coherent soft x-ray radiation in storage rings using angular-modulated electron beams. Phys Rev Lett 104(8):084803
- 35. Saldin EL, Schneidmiller EA, Yurkov MV (2002) Study of a noise degradation of amplification process in a multistage HGHG FEL. Opt Commun 202(1):169–187
- 36. Ratner D, Fry A, Stupakov G et al (2012) Laser phase errors in seeded free electron lasers. Phys Rev Spec Top-Accel Beams 15(3):030702
- 37. Allaria E, Appio R, Badano L et al (2012) Highly coherent and stable pulses from the FERMI seeded free-electron laser in the extreme ultraviolet. Nat Photonics 6(10):699–704
- 38. Feng C, Deng H, Wang G et al (2013) Slippage effect on energy modulation in seeded free-electron lasers with frequency chirped seed laser pulses. Phys Rev Spec Top-Accel Beams 16(6):060705

Chapter 4 Experimental Studies on Novel High-Gain Seeded FEL Schemes

Abstract This chapter summarizes several novel seeded FEL experiments that have been recently carried out at the Shanghai deep ultraviolet FEL test facility (SDUV-FEL). A simple method for accurately measuring the slice energy spread of the electron beam has been proposed and experimentally demonstrated at SDUV-FEL. This method has been used in the following EEHG and cascaded HGHG experiments. To distinguish the FEL signal of EEHG from HGHG at low harmonics, we study the electron beam energy chirp effects on different seeded FEL schemes, and found that the output spectrum of an optimized EEHG can be nearly immune to the beam energy chirp. The proof-of-principle experiment for the EEHG has been successfully performed in the ultraviolet region. Design studies for the cascaded HGHG experiment has been given and a novel method based on the energy spectrum of the electron beam has been proposed to demonstrate the "fresh bunch" technique. The first try of cascaded HGHG with a fresh-bunch technique has been also made at SDUV-FEL. The coherent signal from the cascaded HGHG at the fourth harmonic of the seed has been observed.

Keywords Slice energy spread • Energy chirp effects • EEHG • Cascaded HGHG

As we have shown in the previous chapters, numbers of novel high-gain seeded FEL schemes have been proposed in recently years for improving the performances of SASE and HGHG. However, most of these novel FEL schemes have their own uncertainties and limites which are in urgent need of experimental demonstrations. In this chapter, we will show the experimental studies on some novel FEL schemes based on the SDUV-FEL.

4.1 Introduction of the SDUV-FEL

The SDUV-FEL is a multipurpose test facility for FEL principle studies, capable of testing various novel high-gain FEL schemes by chaging the layout of the machine. The design and the relevant R&Ds of this facility have been under way since 2000.

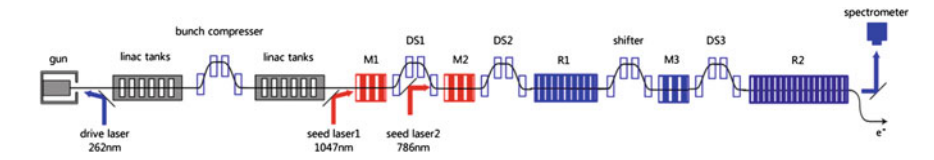


Fig. 4.1 Schematic laypout of the SDUV-FEL

The construction of this machine with a single stage HGHG setup began in 2009. The upgrade of this machine for the two-stage HGHG demonstration was finished in 2012. The schematic layout of this machine is shown in Fig. 4.1 and the main parameters are listed in Table 4.1.

The accelerator system of the SDUV-FEL test facility consists of a photoinjector and a linac. The gun is equipped with a Cu cathode surface, and electrons are extracted by illuminating the photocathode with an 8.7 ps (FWHM), 262 nm drive laser pulse. The energy of the electron bunch at the gun exit is around 4 MeV and the repetition rate is 2 Hz. This gun can provide 100-300 pC electron bunches with a normalized emittance of about 4 μ mrad. The linac provides 140 MeV beams, with a global energy spread of around 0.1 % and a pulse duration of 8.7 ps (FWHM) without compression. The electron bunch can be compressed by about 2 times by the bunch compressor.

There are two laser systems at the SDUV-FEL. The first one is a combined system which provides both the rf gun pulse and the long seed laser pulse at 1047 nm. A laser osicillator is placed in the gun hutch and locked to the 2856 MHz signal generated for the linac system. The pulse of the oscillator is stretched and split in three branches. One is used as the driven laser for the gun; the other two are

4

 L_r (m)

Table 4.1 Main parameters of the SDUV-FEL

$\sigma \gamma / \gamma = 0.14 \%, 1 - 2 \text{ ps rmslength}$				
	1st stage		2nd stage	
Seed laser	1	2	3	
$\tau(FWHM)$	8.7 ps	8.7 ps/80–100 fs	80–100 fs	
$\lambda_s(\text{nm})$	1047	1047/800-1600	400–800	
Modulator	1	2	3	
$\lambda_u(\text{mm})$	65	50	40	
B _{peak} (T)	0-1.2	0–1.1	0-0.9	
L_m (m)	0.65	0.5	0.64	
Dispersion	1	2	3	
R ₅₆ (mm)	0-40	0–10	0–10	
Radiator	1		2	
$\lambda_u \text{ (mm)}$	40		25	
Break (T)	0-0.9		0.6	

10

 $E = 120 - 190 \,\text{MeV}, Ip = 100A, \varepsilon = 4 \,\text{mm} \cdot \text{mrad},$

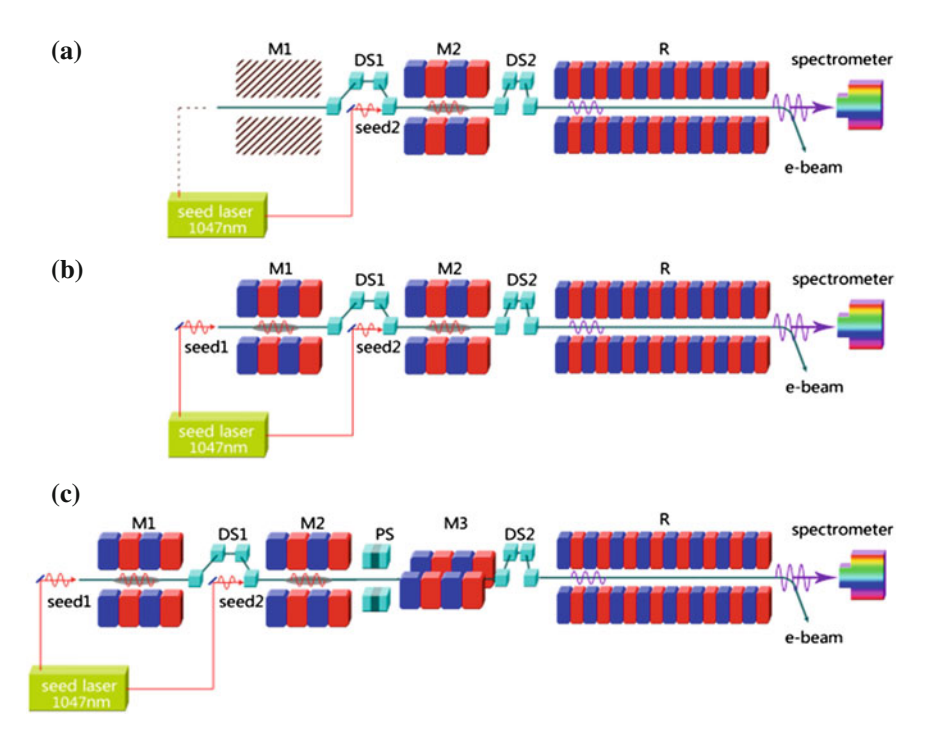


Fig. 4.2 Schematic layouts of the undulator systems of the first stage for different experiments: a HGHG, b EEHG and c polarization control

sent through a bow-tie polarization-maintaining optical fiber and delivered by a 40 m long beam transport system for the seeding purpose. The other laser system is used for providing the ultr-short seed laser pulse. The laser seed comes from the commercial coherent Ti:Sa system at 800 nm followed by a traveling wave optical parametric amplifying system (OPA), which can provide up to a few micro-Joules energy with about 80–100 fs pulse duration and wavelengths continuously tunable from 1160 to 1580 nm.

The undulator system of the SDUV-FEL is quite complex. The layout has been changed several times for different purposes, as shown in Fig. 4.2. The undulator system is originally designed for testing the HGHG (Fig. 4.2a). Initially, there is only one modulator (M2), one dispersion section (DS1) and one radiator (R). Then an addintional modulator (M1) is added before the HGHG configuration to performe the experiment for EEHG (Fig. 4.2b). After that, another short undulator (M3) is added between the M2 and R to demonstrate the polarization switching techinique using the crossed-planar undulator configuration (Fig. 4.2c). Now we have added another stage of HGHG after the first stage to configurate the layout for cascaded HGHG study (Fig. 4.1). With this undulator system, we can carry out the proof-of-principle experiments for nearly all kinds of seeded FEL schemes.

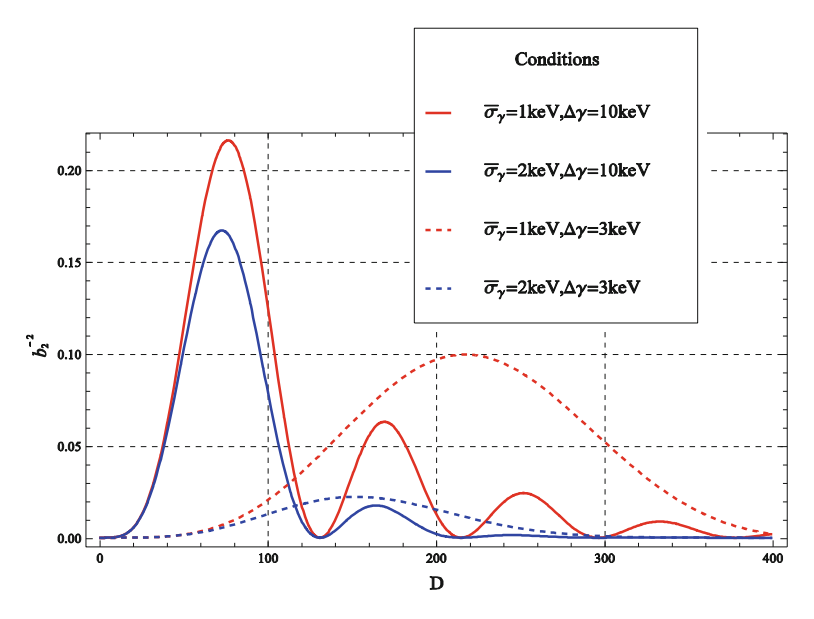


Fig. 4.3 Bunching factor squared as a function of DS strength for different conditions. *Solid line* $\overline{\sigma_{\gamma}} = 1 \text{ keV}$, $\Delta \gamma = 10 \text{ keV}$; *dot dashed line* $\overline{\sigma_{\gamma}} = 2 \text{ keV}$, $\Delta \gamma = 10 \text{ keV}$; *dashed line* $\overline{\sigma_{\gamma}} = 1 \text{ keV}$, $\Delta \gamma = 3 \text{ keV}$; *dotted line* $\overline{\sigma_{\gamma}} = 2 \text{ keV}$, $\Delta \gamma = 3 \text{ keV}$. (Reprinted with permission from Ref. [5]. Copyright 1998 by American Physical Society)

4.2 Measurement of the Slice Energy Spread of Electron Beam via CHG

Most present and future designs of linac driven high-gain FELs adopt high brightness photo injectors to meet the requirements on the transverse and longitudinal beam quality. One of the fundamental parameters in photo-injectors is the slice energy spread which has strong impact on the FEL performance. For seeded FEL schemes, the contradictory requirements of large energy modulation and small slice energy spread constrain the possibility of working at high harmonic number for a single stage. The study of slice energy spread allows to deeply investigate the details of energy spread compensation method and to design and tune the FEL machine for best performance.

Significant efforts have been devoted in past decades to measurement of the realistic electron beam. Since the electron bunches are much shorter than the temporal resolution of measurement devices, standard electron beam diagnostics are routinely used in measuring the projected parameters like the beam charge, emittance and energy spread of the full electron bunch. The slice energy spread of electron beam produced by a photo-injector is believed to be in the order of few keV. For accelerator research, it remains a challenge to measure the energy spread

with high accuracy across a wide range. Driven by the urgent need for measuring the local energy spread of the beam, various instrumentations and methods such as transverse deflecting radiofrequency cavity [1], FEL gain curve based method [2], optical klystron (OK) based method [3] or optical replica synthesizer (ORS) based method [4] have been developed. However, the resolution of these methods are still not high enough for accurate measuring the slice energy spread.

In this section, we propose a new method for characterizing the slice energy spread based on the CHG. Similar to the ORS based method, the information of the local energy spread is determined using the CHG. In contrary to the ORS based method, measurement of the current profile is not necessary and the energy modulation can be arbitrary with respect to the local energy spread. Instead, two measurements with different seed laser powers are needed. The energy modulation amplitudes induced by the seed lasers can be obtained at the same time.

4.2.1 CHG Based Energy Spread Measurement Method

The density modulation of the electron beam can be quantified by the bunching factor, which has a maximum value of unity. Analytically, the initial bunching factor of *n*th harmonic in the radiator is given by

$$b_k = J_k(kD\Delta\gamma)e^{-\frac{1}{2}(nD\sigma_\gamma)^2} \tag{4.1}$$

where $D = ksR56/\gamma$ is a dimensionless parameter related to the dispersive strength of the DS, and $\Delta \gamma$ is the energy modulation amplitude induced by the seed laser, which can be expressed as

$$\begin{cases} \Delta \gamma = k_s a_s a_{um} l_m [JJ]_1 / \gamma \\ a_s = \sqrt{\frac{Z_0 P_{seed}}{\pi k_s Z_R (mc^2/e)^2}} \end{cases}$$
(4.2)

where a_s and a_{um} are the dimensionless (rms) vector potentials of the spontaneous radiation and magnetic field of the modulator, respectively. l_m is the length of the modulator, $[JJ]_1$ is the polarization modification factor for a linearly polarized planar undulator, $Z_0 = 377 \, \Omega$ is the vacuum impedance and Z_R is the Rayleigh length of the seed laser. From Eq. (2.26), it is found that the energy modulation is in proportion to the square-root of the seed laser power: $\Delta \gamma \propto \sqrt{P_{seed}}$. In order to get sufficient bunching factor, $nD\sigma_{\gamma} < 1$ should be satisfied, and the nth Bessel function will reach its first and absolute maximum when $nD\Delta \gamma \approx n+1$ according to Eq. (4.1), which means that the energy modulation amplitude should be n times larger than the initial local energy spread.

For a longitudinally uniform distributed electron beam, the output power of a CHG can be simplified as

$$P = \frac{\left(Z_0 K [JJ]_1 l_r l b_k\right)^2}{32\pi \Sigma \gamma^2} \tag{4.3}$$

where l_r is the length of the radiator. For a realistic electron beam, when the slippage length is much shorter than the bunch length, the output radiation profile will be coupled strongly with the local beam current, bunching factor and transverse beam area. The output CHG energy should be the integration of the radiation power along electron beam,

$$E_{CHG} \approx \frac{\left(Z_0 K [JJ]_1 l_r\right)^2}{32\pi\gamma^2 c} \int_0^{l_b} \frac{I^2 b_k^2}{\Sigma} dz$$
 (4.4)

where l_b is the full length of the electron bunch. Considering the weight factor of the local beam current, transverse beam area and bunching factor, the average slice energy spread $\overline{\sigma \gamma}$ and the average energy modulation amplitude $\overline{\Delta \gamma}$ can be defined as

$$\overline{\sigma_{\gamma}} = \frac{1}{kD} \ln^{1/2} \left\{ \int_{0}^{l_b} \left[J_k(kD\Delta \gamma)I \right]^2 / \Sigma dz / / \int_{0}^{l_b} \left[J_k(kD\Delta \gamma)I \right]^2 / \Sigma e^{\left(kD\sigma_{\gamma}\right)^2} dz \right\}$$
(4.5)

$$J_{k}(kD\overline{\Delta\gamma}) = \int_{0}^{l_{b}} \left[J_{k}(kD\Delta\gamma)I\right]^{2} / \Sigma dz / \int_{0}^{l_{b}} I^{2} / \Sigma dz$$
 (4.6)

Following these expressions, the average bunching factor can be written as

$$\overline{b_k} = J_k (kD\overline{\Delta \gamma}) e^{-\frac{1}{2} (kD\overline{\sigma_{\gamma}})^2} \tag{4.7}$$

and Eq. (4.4) yields

$$E_{CHG} \approx \frac{\left(Z_0 K [JJ]_1 l \overline{b_k}\right)^2}{32\pi \gamma^2 c} \int_0^{l_b} \frac{I^2}{\overline{\Sigma}} dz \tag{4.8}$$

It is clear that $E_{CHG} \propto \overline{b_n}^2$. Given a seed laser power, one can find the optimized DS strength to maximize the E_{CHG} . Figure 4.3 shows the theoretical results of the 2nd harmonic bunching factor as a function of the DS strength for different local energy spreads and energy modulation amplitudes, it is clearly shown that the optimized values of D will be quite different under different conditions.

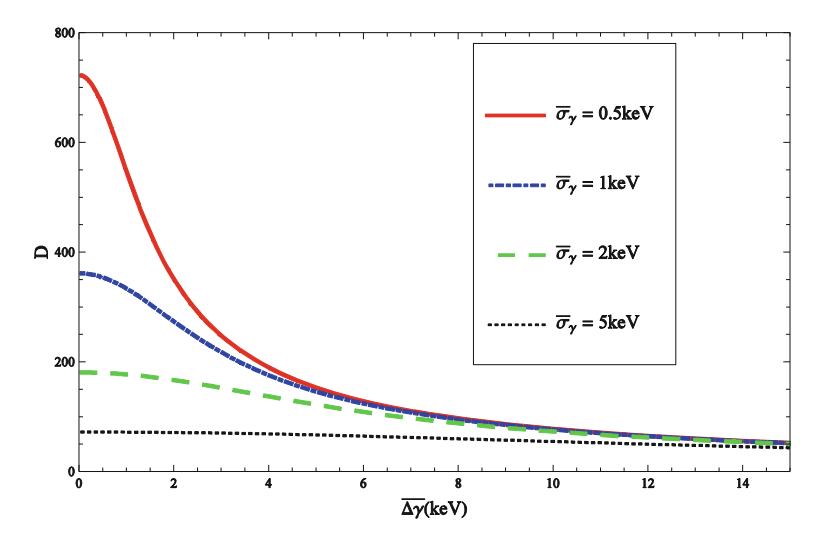


Fig. 4.4 Optimized DS strength as a function of energy modulation amplitude for various values of local energy spread. The $\overline{\sigma_{\gamma}}$ is changed from 0.5 to 5 keV and the optimized value of D is obtained by numerically solving the first root from Eq. (4.9). *Solid line* $\overline{\sigma_{\gamma}} = 0.5$ keV; *dot dashed line* $\overline{\sigma_{\gamma}} = 1$ keV; *dashed line* $\overline{\sigma_{\gamma}} = 2$ keV; *dotted line* $\overline{\sigma_{\gamma}} = 5$ keV. (Reprinted with permission from Ref. [5]. Copyright 1998 by American Physical Society)

To find the parameters that maximize the bunching factor, we differentiate Eq. (4.8) with respect to D, and set the derivative equal to zero,

$$J_{k-1}(k\overline{\Delta\gamma}D) - J_{k+1}(k\overline{\Delta\gamma}D) = \frac{2k\overline{\sigma_{\gamma}}^2D}{\overline{\Delta\gamma}}J_k(k\overline{\Delta\gamma}D)$$
(4.9)

It is easy to find that among the infinite number of roots of Eq. (4.9), only the first root maximize the expression of bunching factor. Figure 4.4 shows the optimized dispersive strength with respect to energy modulation amplitude for different slice energy spread. The optimized DS strengths tend to be a similar value when the energy modulation amplitude is much bigger than the initial slice energy spread but become quite different as the energy modulation amplitude decays for different slice energy spreads. There are two unknown parameters: $\overline{\Delta \gamma}$ and $\overline{\sigma_{\gamma}}$ in Eq. (4.9), it is necessary to change the condition once to solve them out. The energy modulation amplitude can be easily varied by changing the seed laser power. The ratio of the average energy modulation amplitudes can calculated by

$$C = \overline{\Delta \gamma_1} / \overline{\Delta \gamma_2} = \sqrt{P_1 / P_2} \tag{4.10}$$

where P_1 and P_2 are seed laser powers, $\overline{\Delta \gamma_1}$ and $\overline{\Delta \gamma_2}$ are the corresponding average energy modulation amplitudes. The best operating condition can be found by scanning the DS strength for different $\Delta \gamma$. It is worth to point out that the average

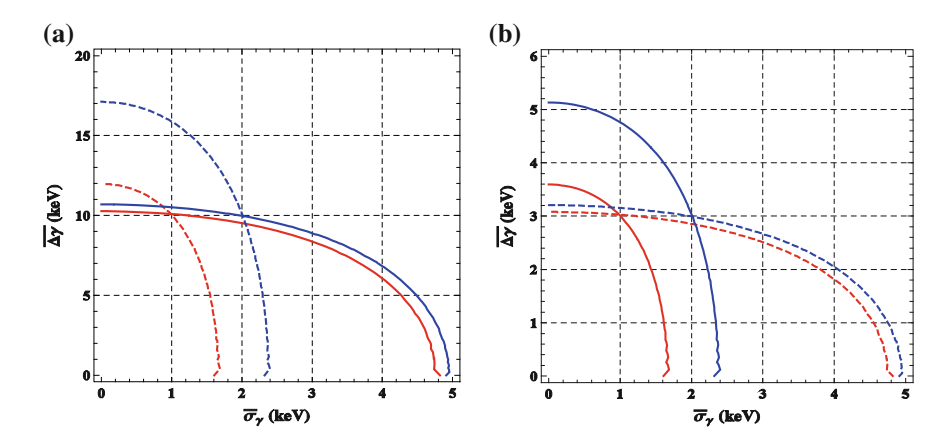


Fig. 4.5 Calculation results of average local energy spread and average energy modulation amplitude with different energy modulation amplitudes (**a**) and (**b**). (Reprinted with permission from ref. [5]. Copyright 1998 by American Physical Society)

local energy spread can also be solved out by scanning the seed laser power for different dispersion strengths. The simultaneous equations for solving $\overline{\sigma_{\gamma}}$ and $\overline{\Delta \gamma}$ are as follows

$$\begin{cases}
J_{k-1}(kD_1\overline{\Delta\gamma_1}) - J_{k+1}(kD_1\overline{\Delta\gamma_1}) = \frac{2k\overline{\sigma_{\gamma}}^2D_1}{\overline{\Delta\gamma_1}}J_k(kD_1\overline{\Delta\gamma_1}) \\
J_{k-1}(kD_2\overline{\Delta\gamma_1}/C) - J_{k+1}(kD_2\overline{\Delta\gamma_1}/C) = \frac{2k\overline{\sigma_{\gamma}}^2D_2}{\overline{\Delta\gamma_1}/C}J_k(kD_2\overline{\Delta\gamma_1}/C)
\end{cases} (4.11)$$

In the case of Fig. 4.3, the optimized conditions are $D_1=76$ for the solid line, $D_2=217$ for the dot dashed line, $D_1'=73$ for the dashed line and $D_2'=152$ for the dotted line. The ratios of the seed laser powers are C=C'=3/10. The solutions of Eq. (4.11) based on these parameters are the crossover points of the curves with the same type shown in Fig. 4.5. The results show that the $\overline{\sigma_{\gamma}}$ is 1 keV and $\overline{\sigma_{\gamma}}'$ is 2 keV, the $\overline{\Delta \gamma_1}$ and $\overline{\Delta \gamma_1}'$ are both 3 keV. These results coincide with the conditions shown in Fig. 4.3.

4.2.2 Experimental Results at the SDUV-FEL

Experiments has been carried to test the proposed method based on the SDUV-FEL. The layout of the experiment is shown in Fig. 4.6. Main parameters are listed in Table 4.2.

The resonant wavelength of the modulator was tuned to the seed laser wavelength by adjusting the gap and the radiator was set at its 2nd harmonic. One of the

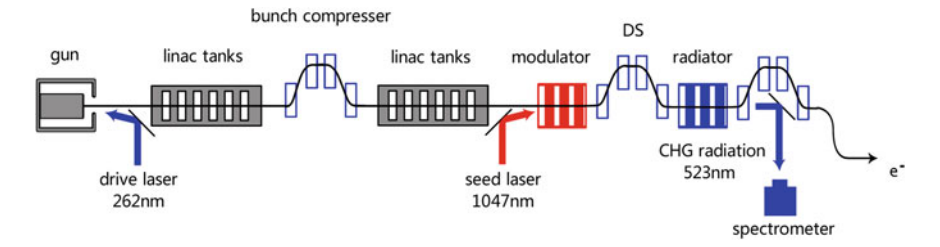


Fig. 4.6 SDUV Schematic layout of the SDUV-FEL scheme with CHG setup. (Reprinted with permission from Ref. [5]. Copyright 1998 by American Physical Society)

Table 4.2 Parameters of SDUV–FEL with CHG setup

Electron beam				
Energy [MeV]	136			
Energy spread [MeV]	0.2			
Charge [pC]	100			
Normalized emittance [µmrad]	4.5			
Bunch length (FWHM) [ps]	~8			
Seed laser				
Wavelength [nm]	1047			
Pulse energy [µJ]	0–150			
Pulse length (FWHM) [ps]	8.7			
Modulator				
Period [mm]	65			
Period number	10			
Radiator				
Period [mm]	50			
Period number	10			
Dispersion section				
R ₅₆ [mm]	0–40			

Reprinted with permission from Ref. [5]. Copyright 1998 by American Physical Society

key issues for the seed experiment is to achieve temporal and spatial overlap of the electron bunches and the seed laser pulses in the modulator. Figure 4.7 shows the method for realizing this overlap at the SDUV-FEL. The transverse overlap was achieved by observing the electron beam and the laser beam on the OTR screens located upstream and downstream of the modulator and placing both beams on the same transverse position. The transverse size of the laser spot was adjusted to be at least 5 times larger than the transverse size of the electron beam to keep the modulation amplitude the same along the electron bunch. The spontaneous emission from the electron beam passing through the modulator and the seed laser pulse were sent into a fast photodiode (2 GHz) to find the initial coarse temporal overlap. A high resolution oscilloscope with 6 GHz bandwidth was used to

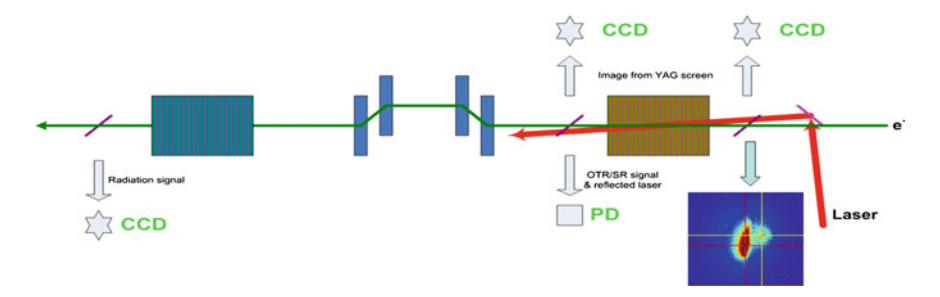
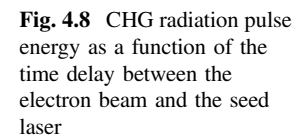
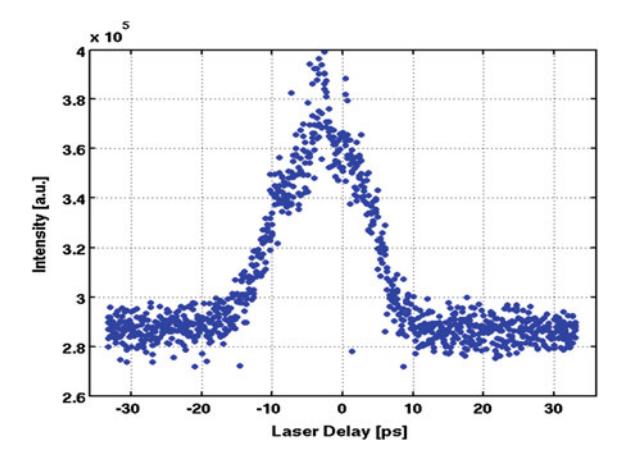


Fig. 4.7 Overlap of the seed laser pulse and the electron beam at the SDUV-FEL





synchronize the two signals with an accuracy of 30 ps. Then the exact temporal overlap can be obtained by fine tuning the delay line of the seed laser to optimize the output power of the CHG signal, as shown in Fig. 4.8. The time jitter of our system is smaller than 1 ps, which is much shorter than the pulse lengths of the seed laser and the electron beam.

The 2nd harmonic radiation produced by the radiator is reflected out by an OTR screen and recorded by a CCD with a 400–800 nm band pass filter, which is used to distinguish the CHG radiation from the intense seed laser pulse. The CHG image was clearly observed as shown in Fig. 4.9a. Figure 4.9b shows the spectrum of the radiation detected by a miniature fiber-optic spectrometer close to the window of OTR chamber. The CHG radiation is fully coherent and the center wavelength is about 521 nm.

To find the optimized working condition of the CHG, we need to scan the gap of the radiator and the strength of the dispersion section. Figure 4.10 shows the output pulse energy variation as a function of the peak magnetic field of the radiator. One can find that there are two peaks in the scan curve, appears at 0.23 and 0.58 T. The corresponding resonant wavelengths are 520 and 1560, respectively, which means that the second peak is the third harmonic radiation of the radiator.

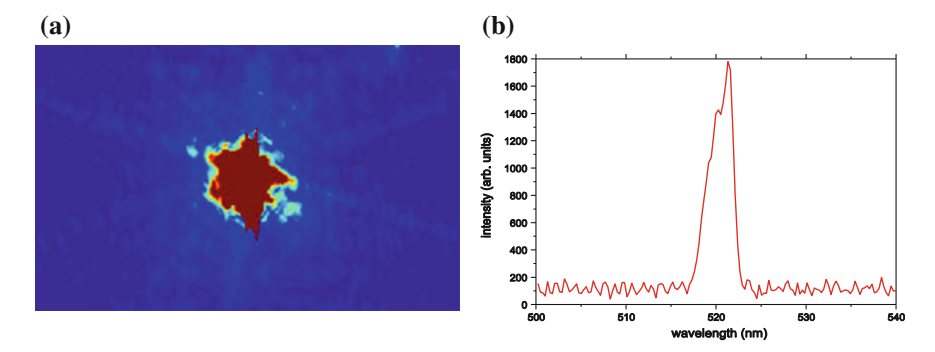
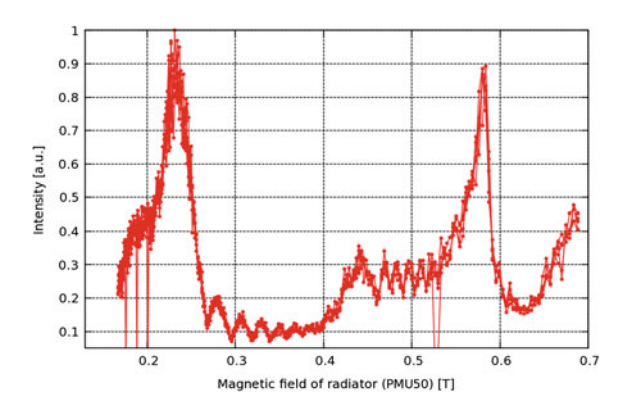


Fig. 4.9 a Radiation intensity on an OTR screen downstream of the radiator, the radiation was recorded by a CCD with a 400–800 nm band pass filter. **b** Single shot 2nd harmonic CHG spectrum detected by a miniature fiber-optic spectrometer. (Reprinted with permission from Ref. [5]. Copyright 1998 by American Physical Society)

Fig. 4.10 The output pulse energy of the CHG as a function of the peak magnetic field of the radiator



The R_{56} of the DS can be easily scanned from 1 to 40 mm. The experimental data of 2nd harmonic radiation intensity as a function of the R_{56} is shown in Fig. 4.11. To further reduce the affection of the time jitter to our measurement, five points of radiation pulse intensities was recorded for each R_{56} . The experimental data shown in Fig. 4.8 can be fitted well with several theoretical curves with quite different parameters, which means that the slice energy spread cannot be determined by one measured curve.

To get accurate value of the local energy spread and analyze the causes of measurement error of this method, numbers of experimental curves were measured. The seed laser energy was changed from 150 to 0.58 μJ and the strength of the DS was scanned from 1 to 16 mm for each laser energy. The measurement results and fitted curves are shown in Fig. 4.12. Every two curves can be used to obtain one value of average local energy spread and two values of energy modulation amplitudes for both seed laser energies. All these calculation results are summarized in Fig. 4.13.

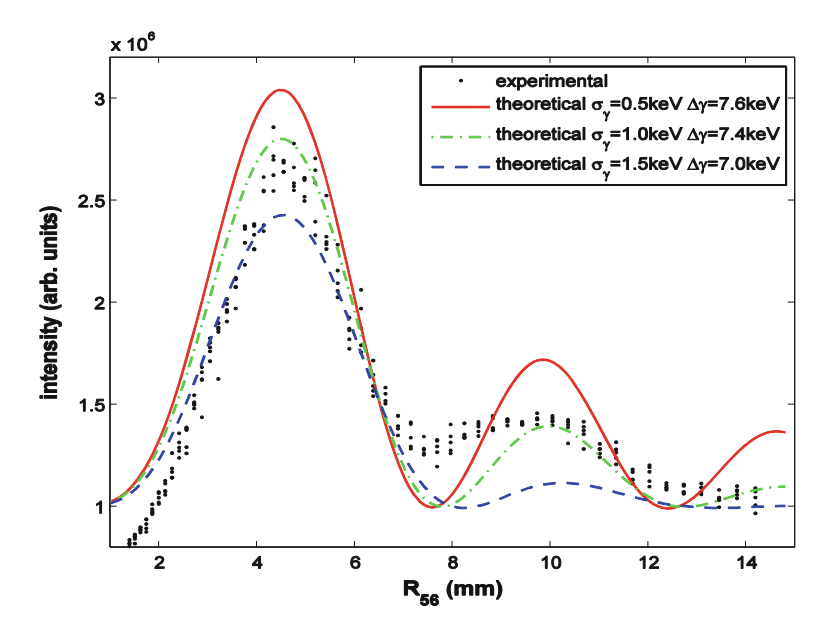


Fig. 4.11 Intensity of the 2nd harmonic radiation as a function of the DS strength. (Reprinted with permission from Ref. [5]. Copyright 1998 by American Physical Society)

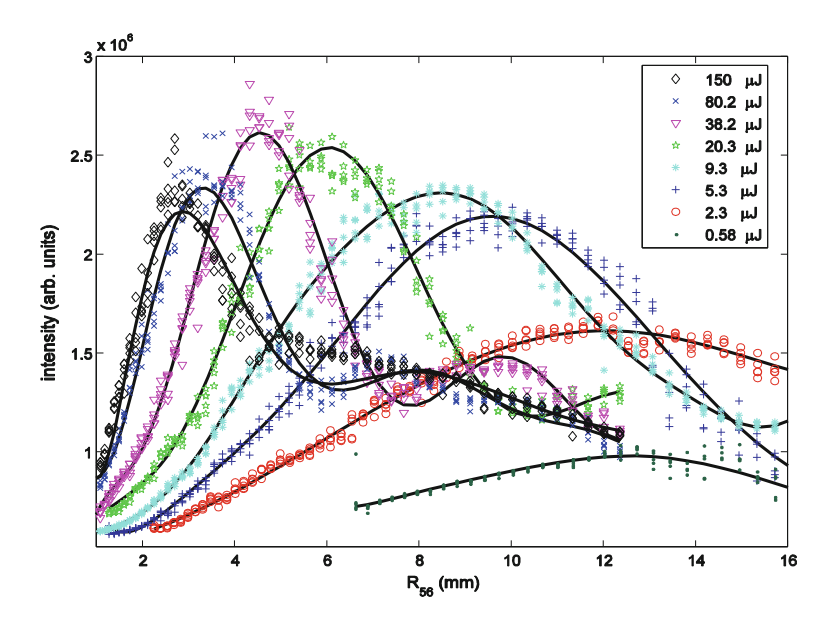


Fig. 4.12 Experimental data and fitted curves for various values of seed laser energy. The radiation intensity was recorded by a CCD when scanning the DS strength. (Reprinted with permission from Ref. [5]. Copyright 1998 by American Physical Society)

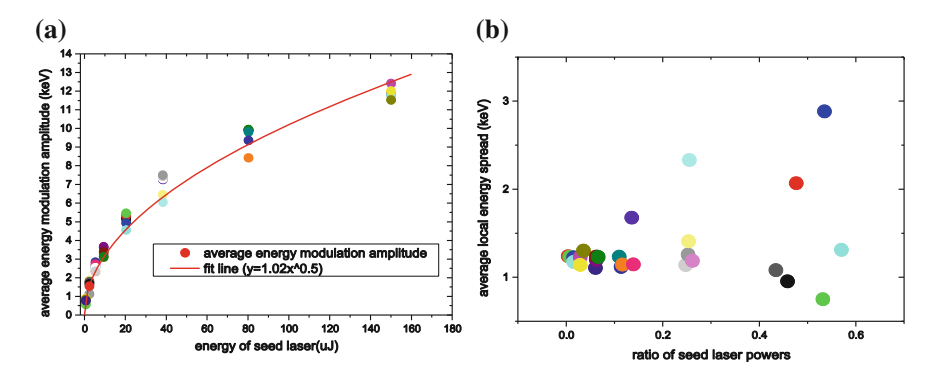


Fig. 4.13 Calculation results for all the combinations of experimental curves. **a** Average energy modulation amplitudes for various seed laser energies and the fitted curve of these points. **b** Average slice energy spreads for various ratios of seed laser powers. (Reprinted with permission from Ref. [5]. Copyright 1998 by American Physical Society)

The energy modulation amplitude shown in Fig. 4.13a is proportional to the square-root of the laser energy. The maximum energy modulation is over 12 keV and the minimum value is less than 1 keV. In Fig. 4.10b, the deviation of the measured local energy spread is small when the ratios of the two seed laser powers are less than 0.1 (or greater than 10). The scanning curves will be difficult to be clearly separated when the two seed laser powers are too close to each other. In order to separate these curves and minimize the observation error, the ratio of the seed laser powers should be large enough and one of the energy modulation amplitudes should be close to the slice energy spread. The data points that satisfy these criterions in Fig. 4.13b are shown in Fig. 4.14. Averaging over these points,

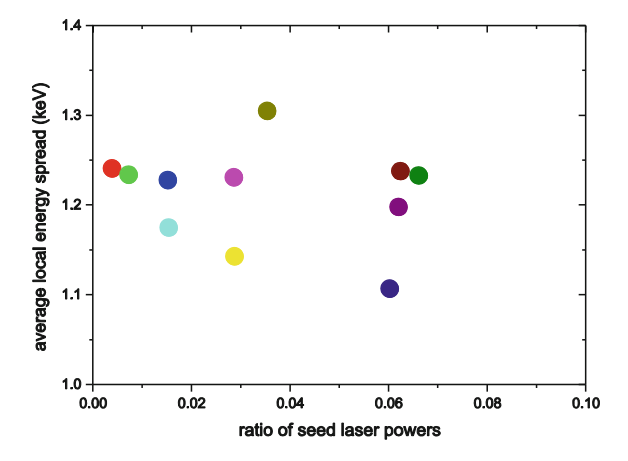


Fig. 4.14 Calculation results of the average local energy spread based on the measurement curves with the ratios of seed laser powers are less than 0.1 (or bigger than 10). (Reprinted with permission from Ref. [5]. Copyright 1998 by American Physical Society)

one can find that the average local energy spread is about 1.2 keV with the standard deviation of about 0.054 keV.

These experiment results show that the slice energy spread of the electron beam at the exit of the linac with beam energy of 136 MeV and beam charge about 100 pC is only about 1.2 keV, which is about one order of magnitude smaller than we expected. The proposed method can also be used to characterize the slice energy spread distribution along the electron beam by using a short pulse seed laser to scan the electron beam in the longitudinal direction. This kind of measurement provides a fairly important tool for quick machine tuning and optimization of seeded FELs. The information of the slice energy spread and the energy modulation amplitude will be very useful for the parameters setting of an EEHG experiment.

4.3 Experimental Studies of the EEHG

Analysis within the framework of idealized models promisingly indicate that EEHG can produce fully coherent soft x-ray radiation with a single stage set-up. Thus the EEHG scheme seems an attractive way for the soft X-ray light source. Experimental studies on the modulation mechanism for EEHG have been first performed at the Next LinearCollider Test Accelerator (NLCTA) at SLAC National Accelerator Laboratory [6] and the SDUV-FEL at SINAP [7].

4.3.1 Energy Chirp Effects on HGHG and EEHG

It is anticipated that seeded FEL schemes can be used for generation of transform-limited radiation pulse, which usually requires a uniform electron beam with constant current and energy. However, it is found that the energy profile of the electron bunch coming into the undulator usually has an initial energy chirp and an energy curvature due to the radio frequency curvature and wakefield effects in the accelerator. Sometimes this energy chirped electron beam may be useful to overcome the sensitivity of the output power to the electron beam energy jitters. However, the energy chirp in the electron beam will also impact the FEL process in the undulator and result in a broader output bandwidth.

According to the basic theory of EEHG, the central wavelength of the EEHG radiation should be

$$\lambda_{\text{EEHG}} = 1 / \left[\frac{n}{\lambda_{s1}} + \frac{m}{\lambda_{s2}} \right] \tag{4.12}$$

where m and n are integers, λ_{s1} and λ_{s1} are the wavelengths of the seed lasers. The central wavelengths of the HGHG and the EEHG have a quite different dependence on the energy chirp [8]:

$$\lambda'_{\text{HGHG}} = \lambda_s (1 + HB)/k \tag{4.13}$$

$$\lambda'_{\text{EEHG}} = \left[1 + H(B_1 + B_2)\right] / \left[\frac{n}{\lambda_{s1}} + (1 + HB_1)\frac{m}{\lambda_{s2}}\right]$$
(4.14)

where $H = hE_0\lambda_{s1}/2\pi\sigma_E$ is the dimensionless chirp factor, h is the energy chirp factor, $R_{56}^{(1)}$ and $R_{56}^{(2)}$ are strengths of DSs and k = n + mK is the harmonic number of HGHG, $K = \lambda_{s1}/\lambda_{s2}$. Here, we define the wavelength shift factor $a = \lambda'_{\rm EEHG}/\lambda_{\rm EEHG}$. From Eq. (4.14), one can get

$$a = 1 + CH, \tag{4.15}$$

where

$$C = B_1 + B_2 - \lambda'_{\text{EEHG}} m B_1 / \lambda_{s2}. \tag{4.16}$$

It is found from Eqs. (4.12) and (4.16) that the output wavelength will immune to the energy chirp (C = 0) when the relation between the two DS strengths satisfies

$$B_2 = -\frac{n}{k}B_1. (4.17)$$

The optimized relationship between the strengths of the two DSs for EEHG operation is

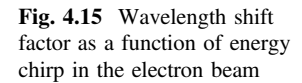
$$B_2 = -\frac{n}{k}B_1 + \frac{\xi}{k},\tag{4.18}$$

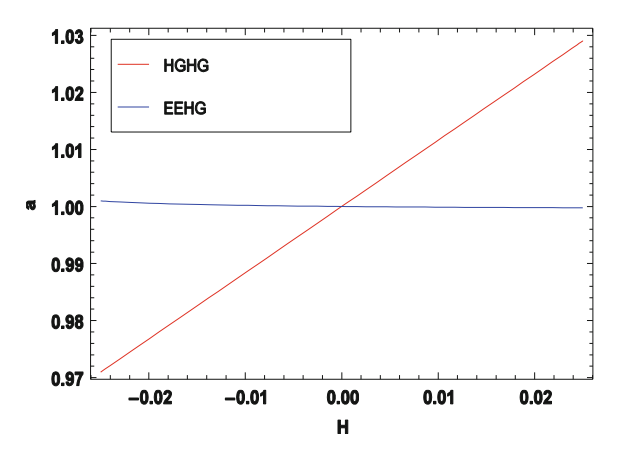
where ξ is the solution of

$$A_1[J_{n-1}(A_1\xi) - J_{n+1}(A_1\xi)] = 2\xi J_n(A_1\xi). \tag{4.19}$$

Generally, for a given B_1 , the difference between the optimized values calculated by Eqs. (4.17) and (4.18) can be turned to be much smaller than B_2 by increasing A_1 and k, which means that the EEHG scheme with optimized condition will be insensitive to the energy chirp at high harmonics.

Figure 4.15 shows wavelength shift factors as a function of the energy chirp for both HGHG and EEHG. The parameters of EEHG used here are $A_1 = 6$, $A_2 = 1$, $B_1 = 23.53$, $B_2 = 1.16$ and K = 1, which are optimized for the 20th harmonic of the seed. The strengths of the DSs are quite close to the requirement of Eq. (4.17). It is found in Fig. 4.15 that the wavelength shift factor of EEHG nearly has no response to the energy chirp.





4.3.2 Design Studies for the EEHG Experiment at the SDUV-FEL

The EEHG lasing experiments at the SDUV-FEL will be performed at the third harmonic of the laser seed, which is limited by the maximum achievable energy of the electron beam. In this case it is necessary to introduce energy chirp, which represents the energy-time correlation, into the electron beam to effectively distinguish the EEHG signal from the HGHG signal. As pointed out in the previous section, with an energy chirp in the electron beam, the central wavelength of HGHG will shift and the output bandwidth will be broaden. The effect of nonlinear energy chirp on the bandwidth of the EEHG FEL is much smaller than on that of the HGHG FEL. So the ouput spectra of the HGHG and EEHG will be different.

The output spectra of the HGHG and EEHG radiation are determined by the electron micro-bunching. Figure 4.16 shows the comparation of the electron beam phase space for HGHG and EEHG at the entrance to the radiator when an energy

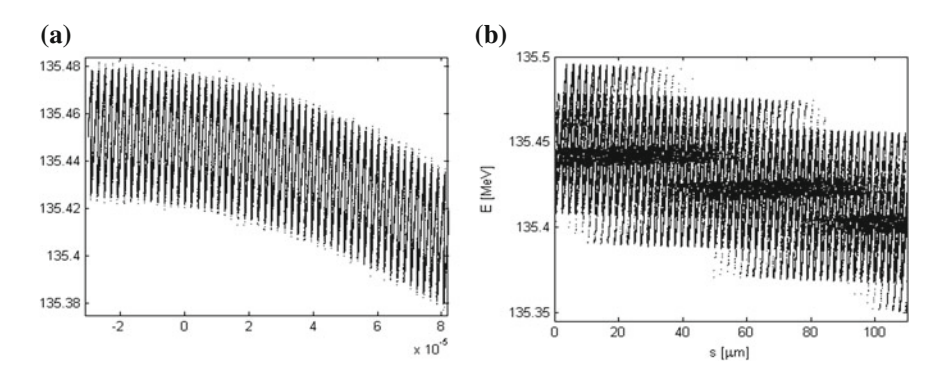
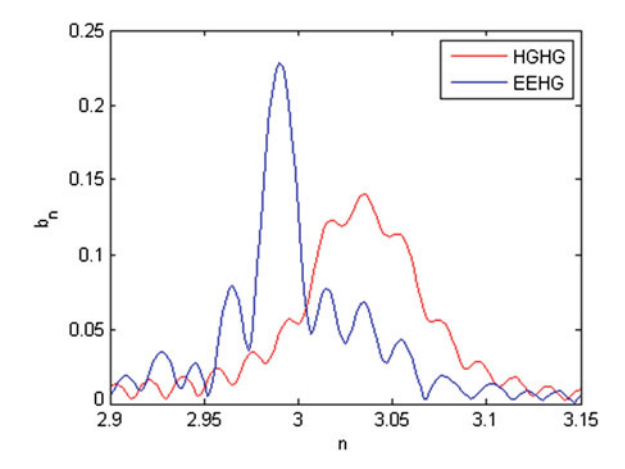


Fig. 4.16 phase space distributions of (a) HGHG and (b) EEHG at the entrance to the radiator

Fig. 4.17 Bunching factor distributions of HGHG and EEHG using electron beam with energy curve



curve is introduced into the electron beam. For the HGHG, the spaces between the micro-bunching varies along the longitudinal direction for different energy chirp, which will results in the spectrum bandwidth broaden. However, for the EEHG, One can find that the energy chirp is changed to "stair" configuration after the second dispersion section of EEHG. In each step the energy chirp is different from the initial energy chirp and can be turned to different values by changing the strengths of the chicanes. The central wavelength shift directions of HGHG and EEHG can be made opposite by tuning the strength of the first dispersion section of EEHG, as shown in Fig. 4.17.

4.3.3 Experimental Results of EEHG Lasing at the SDUV-FEL

The paramters used in the EEHG sxperiment are similar with that listed in Table 4.1. The electron beam central energy is about 135.4 MeV. The electron bunch length is compressed to about 3 ps by the bunch compressor. The layout of the EEHG FEL experiments is schematically shown in Fig. 4.2b. The main components include two modulators (M1 and M2), two dispersive sections (DS1 and DS2) and one radiator (R). The two laser seeds are both from the 1047 nm drive laser (8.7 ps FWHM pulse length), with a tunable pulse energy of 0–60 mJ. The radiation properties can be investigated with a spectrometer, a photodetector and a CCD. Critical parameters for seeded FEL experiments, such as slice energy spread and the energy modulation amplitudes induced by the laser seeds, can be precisely quantified using the CHG based method. The measured local energy spread is ~ 2.6 keV at the exit of the linac when the electron beam is compressed by a factor of ~ 2 . The maximum energy modulation amplitude induced by the first laser seed is ~ 25.6 keV, ~ 10 times larger than the slice energy spread. The energy modulation amplitude induced by the

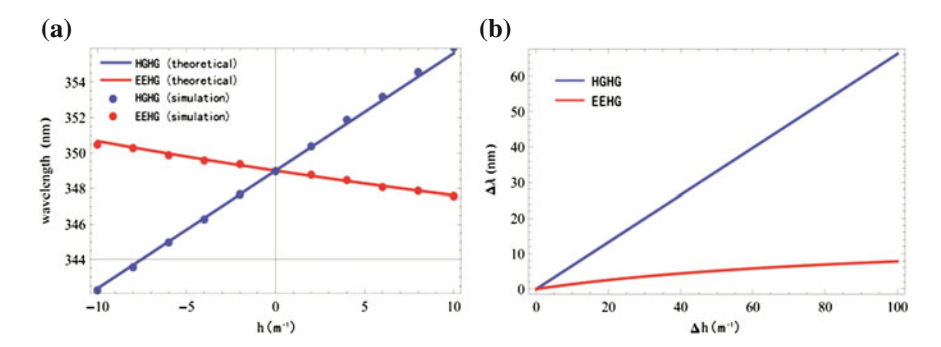


Fig. 4.18 Spectral response to the energy chirp. **a** Central wavelength as a function of energy chirp of the electron beam. **b** Spectral bandwidth as a function of total energy chirp in the electron beam. (Reprinted by permission from Macmillan Publishers Ltd: Ref. [7], copyright 1993)

second laser seed is measured to be ~ 21.4 keV. The strengths of the two dispersive sections are set to be R56(1) = 7 mm and R56(2) = 1.9 mm, respectively, to optimize EEHG performance.

Three-dimensional simulation results from GENESIS and theoretical predictions are shown in Fig. 4.18. It is clear that the central wavelengths of HGHG and EEHG present opposite trends with respect to the beam energy chirp under our experimental conditions, and the wavelength of HGHG is more sensitive to energy chirp than that of EEHG. The effect of nonlinear energy chirp on the bandwidth of the EEHG FEL is much smaller than on that of the HGHG FEL, as shown in Fig. 4.18b.

In the experiments, the laser seed was first introduced to interact with the electron beam in the second modulator (typical HGHG configuration). At this stage, a narrow-bandwidth HGHG signal was observed at 345 nm (Fig. 4.19a, red line) with the spectrometer. Finally, another synchronized laser seed was gradually

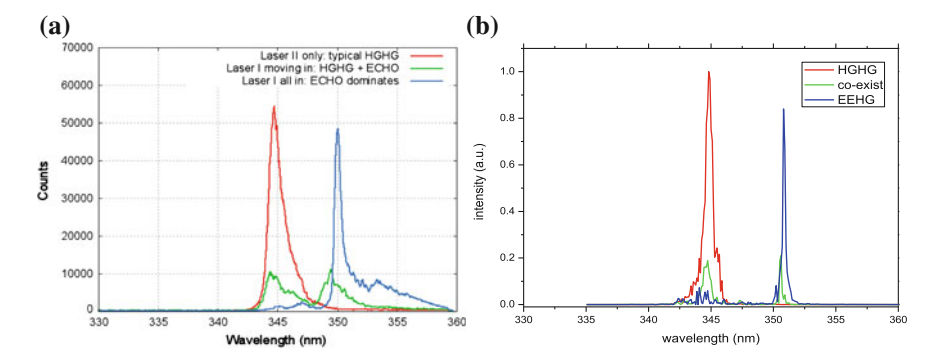
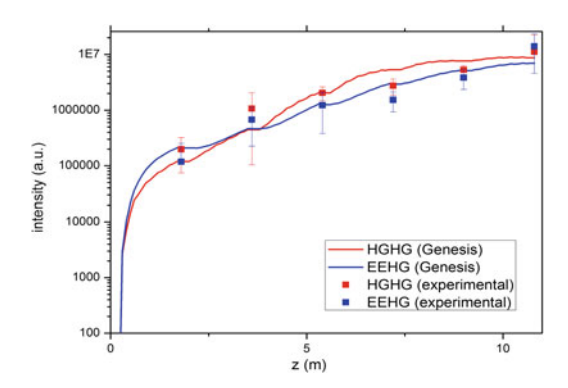


Fig. 4.19 Spectra for FEL radiation: (a) experimental results and (b) simulation results. (Reprinted by permission from Macmillan Publishers Ltd: Ref. [7], copyright 1993)

Fig. 4.20 Gain curves of the EEHG and HGHG FEL. (Reprinted by permission from Macmillan Publishers Ltd: Ref. [7], copyright 1993)



guided to interact with the electron beam in the first modulator to give the EEHG configuration, resulting in the appearance of a narrow-bandwidth signal at a longer wavelength (350 nm), with the existing HGHG signal fading away (Fig. 4.19a, green line); this is an intermediate state between HGHG and EEHG. Once the second laser seed was in its optimized position, the HGHG signal disappeared and the peak of the EEHG signal at 350 nm (Fig. 4.19a, blue line) grew to a level similar to that of the previous HGHG signal. This signal is identified as lased EEHG FEL radiation. From the wavelength shifts in these HGHG and EEHG FEL experiments, the energy chirp in the electron beam is inferred to be $h = -6 \, m^{-1}$. The spectral bandwidth of EEHG is narrower than that of HGHG due to the weaker dependence of nonlinear energy chirp in the electron beam, which is unavoidable in our case. The experimental data agree very well with the simulation results, as shown in Fig. 4.19b.

The gain curves of the EEHG and the HGHG schemes were measured, as shown in Fig. 4.20 together with simulation predictions. As the bunching factors of the electron beam at the entrance of the radiator undulators are almost the same for both schemes, the gain curves behave quite similarly. Meanwhile, as illustrated in Fig. 4.20, the FEL intensity of the EEHG scheme is as stable as that of the HGHG arrangement, and its fluctuation is mainly caused by jitters of the linac parameters. The exponential growth is clearly seen. The measured pulse energy of the EEHG FEL is ~ 1.0 mJ, in reasonable agreement with numerical simulations, which means that a gain larger than 100,000 is achieved compared with the spontaneous radiation from one undulator segment of the radiator. Thus we have successfully demonstrated the first FEL lasing using the novel EEHG scheme at the SDUV-FEL facility. The measurements show that the EEHG FEL scheme can achieve at least the same power level and, in favourable cases, a narrower bandwidth than the HGHG scheme due to its weaker dependence on the energy chirp in the electron beam.

4.4 Experimental Studies of the Cascaded HGHG

To further shorten the output wavelength, the cascaded HGHG FEL together with the fresh-bunch technique is considered as a promising candidate for coherent soft x-ray sources. In the cascaded HGHG scheme, the seed laser pulse is much shorter than the electron bunch length, which makes only a small fragment of the electron beam lased in each stage. The FEL pulse generated by intermediate radiator will be shifted and used as the seed laser for the following stage with the help of the "fresh bunch" technique. The cascaded HGHG scheme is promising for fully coherent soft x-ray generation. Several labs, including BESSY, ELETRRA and SINAP, proposed the development of deep ultraviolet or soft x-ray FEL based on the cascaded HGHG principle. Among them SDUV-FEL has first demonstrated the principle of cascade HGHG and the "fresh bunch" technique.

4.4.1 Design Studies for the Cascaded HGHG Experiment at the SDUV-FEL

The layout of the upgraded SDUV-FEL for the cascaded HGHG experiment is schematically shown in Fig. 4.21. The energy of the electron beam has be enhanced from 140 MeV to about 200 MeV when there is no bunch compression, and the operation beam energy will be about 185 MeV when the beam is compressed by a factor of about 2. The linac commissioning has been done after upgrade. Figure 4.22 shows measurement results of some main parameters. The energy and energy spread of the electron beam are inferred by measuring the beam central position and beam size on the OTR screen downstream a bending magnet. From Fig. 4.22a it is found that the beam energy is over 190 MeV after compression and the project energy spread is 1.41×10^{-3} . The normalized emittance of the electron beam is measured with the quadrupole scan technique using the quadrupole triplet and an OTR screen, the normalized emittance is measured to be 1.83 mm mrad when the bunch charge is about 300 pC.

Besides the upgrade of the linac, new elements have been added in the undulator system for the cascaded HGHG experiment, including one radiator (R1) in the first

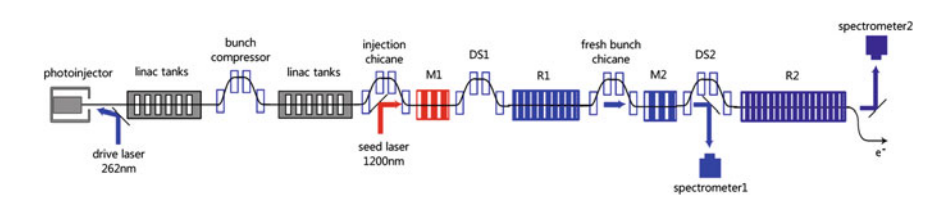


Fig. 4.21 Schematic layout of the cascaded HGHG at the SDUV-FEL. (Reprint from Ref. [9]. Copyright with kind permission from Springer Science+Business Media)

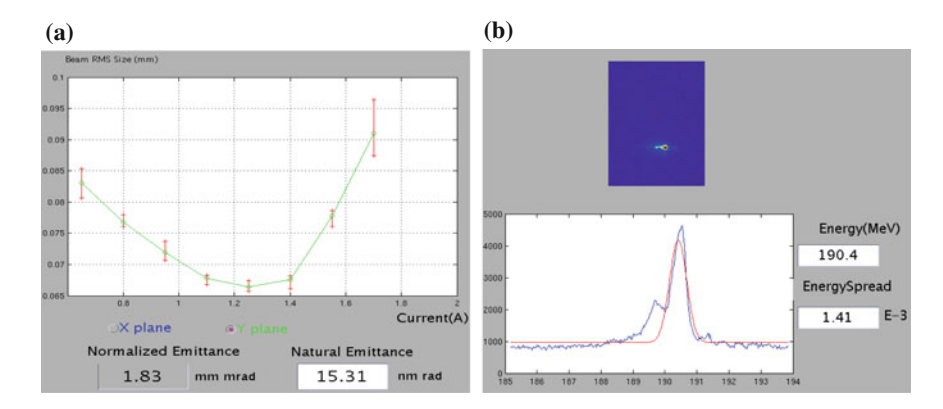


Fig. 4.22 Linac commissioning results after upgrade. **a** The normalized transverse emittance is measured with the quadrupole scan technique. **b** The beam energy and energy spread are measured by the beam energy spectrometer. (Reprint from Ref. [9]. Copyright with kind permission from Springer Science+Business Media)

stage, one modulator (M2) and one dispersion section (DS2) in the second stage and one shifter between two stages. The first stage HGHG expects to generate 393 nm radiation from the 786 nm seed laser. The FWHM length of the seed laser pulse is about 130 fs which is much shorter than the electron bunch length after compression. In the first stage, only a small part of the electron beam is modulated in M1 and generates coherent radiation in R1. This radiation will be shifted to a fresh part of the electron by the shifter and serves as the seed laser for the second stage. A short undulator (M2) with the type of the R1 is employed as the modulator of the second stage and a small chicane (DS2) is used as the dispersion section in the second stage. Finally, the 196.5 nm radiation will be generated by the fresh part of the electron beam in R2.

4.4.1.1 Theoretical Optimization of the Cascaded HGHG

In comparison with the SASE, cascaded HGHG is a multi-dimensional parameter scheme. According to the HGHG theories, the power of the seed laser and the DS strength are crucial to the HGHG process. A large seed laser power is necessary for sufficient energy modulation, but at the same time it acts as an additional energy spread that degrades the quality of the electron beam. When the total energy spread is too large, the amplification process of the FEL will be saturated. The seed laser of the second stage is produced by the first stage, so how to choose the the initial seed laser power will be very important.

According to Eqs. (4.1) and (4.2), the maximal bunching factor b_k is decided by the energy modulation amplitude A, the electron beam energy spread at the entrance to the radiator can be written as

$$\sigma_{\gamma^2} = \sigma_{\gamma} \sqrt{1 + \frac{A^2}{2}}.\tag{4.20}$$

In the first two gain lengths of the radiator, the FEL works in the CHG regime, where the harmonic field grows linearly with the distance traversed in the radiator z, and the peak power grows as z^2 . The output peak power of the CHG after two gain lengths is

$$P_{coh} = \frac{Z_0 I_p^2 K^2 b_k^2 [JJ]^2}{32\pi \Sigma_A \gamma^2} (2L_{G3D})^2$$
 (4.21)

where $L_{G3D} = L_{G1D}(1 + \Lambda)$ is the 3D gain length. After about two gain lengths, the longitudinal dynamic of the electron beam induced by the radiated fields become important, and the radiation power will be exponentially amplified along the radiator:

$$P \approx \frac{3.71}{12} P_{\text{coh}} e^{z/L_{G3D}} \tag{4.22}$$

The saturation power of HGHG should be

$$P_{sat} = 1.6\rho \times \left(\frac{1}{1+\Lambda}\right)^2 \frac{\gamma m_e c^2 I_p}{e} \tag{4.23}$$

From (4.22) and (4.23), we can estimate the saturation length of HGHG:

$$L_{sat} = L_{G3D} \left[\ln \left(\frac{P_{sat}}{P_{coh}} \right) + 2 \right] \tag{4.24}$$

Figure 4.23 shows the theoretical results of the saturation length and saturation power as a function of the initial seed laser power for both two stages. It is found

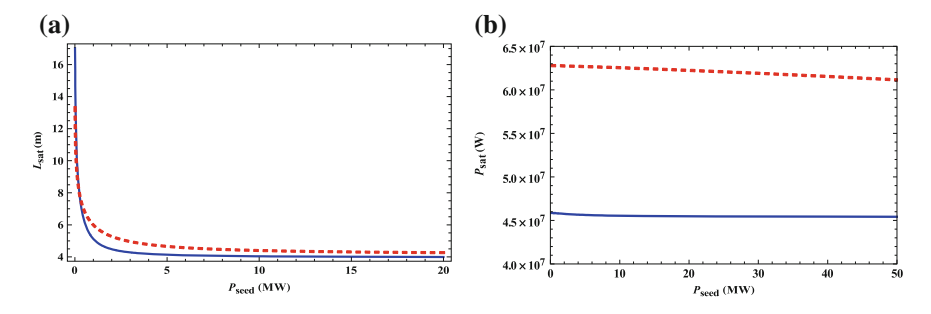


Fig. 4.23 Saturation length (a) and saturation power (b) of the first stage (*red dashed line*) and the second stages (*blue solid line*) as a function of the seed laser power used in the first stage. (Reprint from Ref. [9]. Copyright with kind permission from Springer Science+Business Media)

that the saturation length and saturation power of the second stage will not change much when the power of the initial seed laser is larger than 10 MW for our experiment condition. Thus, the power of the seed laser is chosen to be 10 MW for the first stage.

4.4.1.2 Start-to-End Simulation Results for the Cascaded HGHG Experiment

On the basis of the parameters of the experiment, start-to-end tracking of the electron beam, including all components in Fig. 4.21 has been carried out. The slice parameters at the exit of the linac are summarized in Fig. 4.24. The beam energy in the central part of the electron beam is around 185 MeV and the peak current is about 95 A. A constant profile is maintained in the approximately 1 ps wide and over 80 A region which will be used in the HGHG cascade. The project energy spread of 1.2×10^{-3} are predicted from the beam energy curve. A normalized emittance of approximately 1.6 mm mrad and slice energy spread of about 2.5×10^{-5} are observed in Fig. 4.24b. These simulation results are fit well with the measurement results shown in Fig. 4.22.

The FEL performance was simulated by GENESIS based on the output of ELEGENT. A 786 nm seed pulse with longitudinal Gaussian profile, 10 MW peak power and 130 fs pulse length is adopted as the seed laser of the first stage. The whole electron beam was tracked through the two stages. The simulation results are illustrated in Fig. 4.25. The electron beam is well bunched at the exit of the DS in the first stage. The maximal bunching factor at 2nd harmonic of the seed laser is over 0.4. The first stage HGHG generates 393 nm radiation pulse with the output peak power of about 20 MW. The length of the seed laser pulse is maintained. For the second stage, the 2nd harmonic bunching factor of the fresh bunch is around 0.4. The radiation generated by the fresh part saturates after 4 m with a peak power

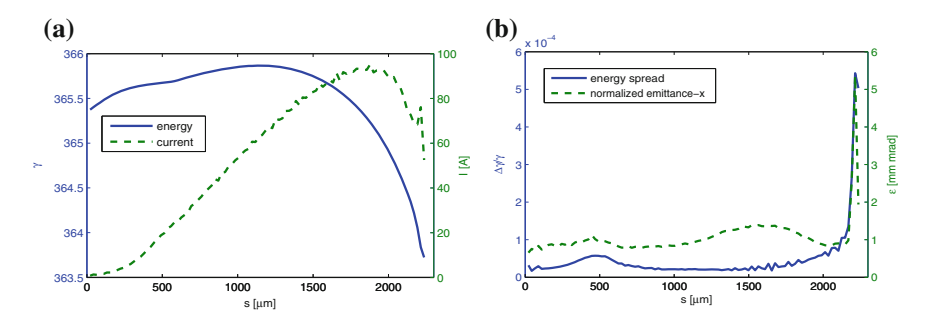


Fig. 4.24 Simulated parameters at the exit of the linac (a) beam energy and current distribution along the electron beam; (b) slice energy spread and slice emittance distribution along the electron beam. (Reprint from Ref. [9]. Copyright with kind permission from Springer Science+Business Media)

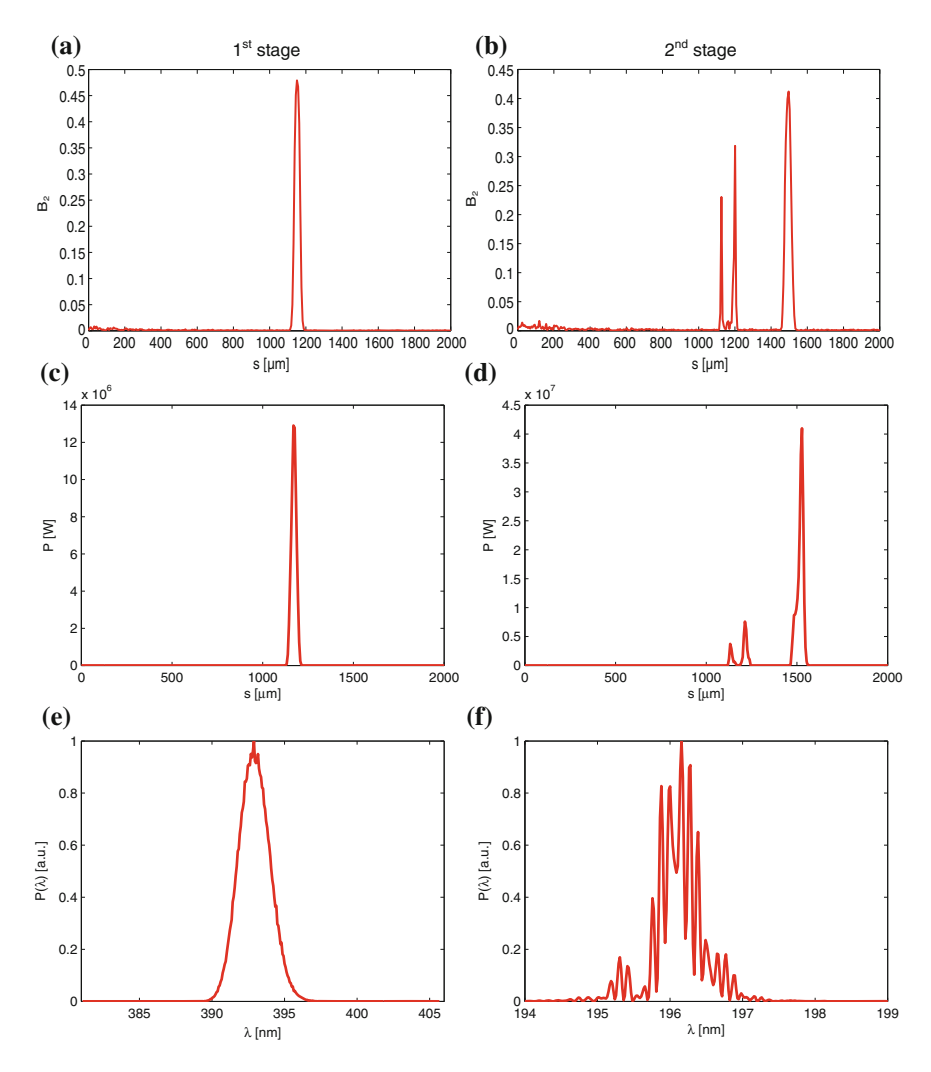


Fig. 4.25 FEL performance in two stages: (a-b) bunching distributions along the electron beam, (b-c) Output radiation pulses and (e-f) spectra of the radiation pulses. (Reprint from Ref. [9]. Copyright with kind permission from Springer Science+Business Media)

of 13 MW. One can find in Fig. 4.25d that there are two 196 nm radiation pulses at saturation. The higher one is generated by the fresh part of the electron beam, and the lower one, about 20 % of the higher pulse energy, is generated by the disturbed part of the electron beam which has been strongly bunched in the radiator of the first stage. It is necessary to change the strength of the shifter to distinguish the 4th harmonic signal produced by the fresh part from that produced by the disturbed

part: the final radiation will be produced only by the disturbed part when the shifter is off, and final radiation will be significantly enhanced when the radiation form the first stage is shifted to a fresh part of the electron beam. The temporal coherence of the final radiation is degraded by the radiation pulse produced by the disturbed part as shown in Fig. 4.25f.

The energy of the radiation pulse produced by the disturbed part in R2 can be depressed by shifting the disturbed part to a low-current region of the electron beam. This can be achieved by shifting the initial seed laser pulse to the tail part of the electron beam in M1. The radiation power generated by the first stage HGHG will also decrease at the same time. We shifted the seed laser pulse by about $800~\mu m$ where the beam current is around 30~A. The simulation results are shown in Fig. 4.26. The output power of the first stage decreases to about 3~MW, which is still sufficient for the energy modulation in the second stage. It is found in Fig. 4.26b that only a single spike is generated by the second stage. The temporal coherence of the final radiation pulse is also improved.

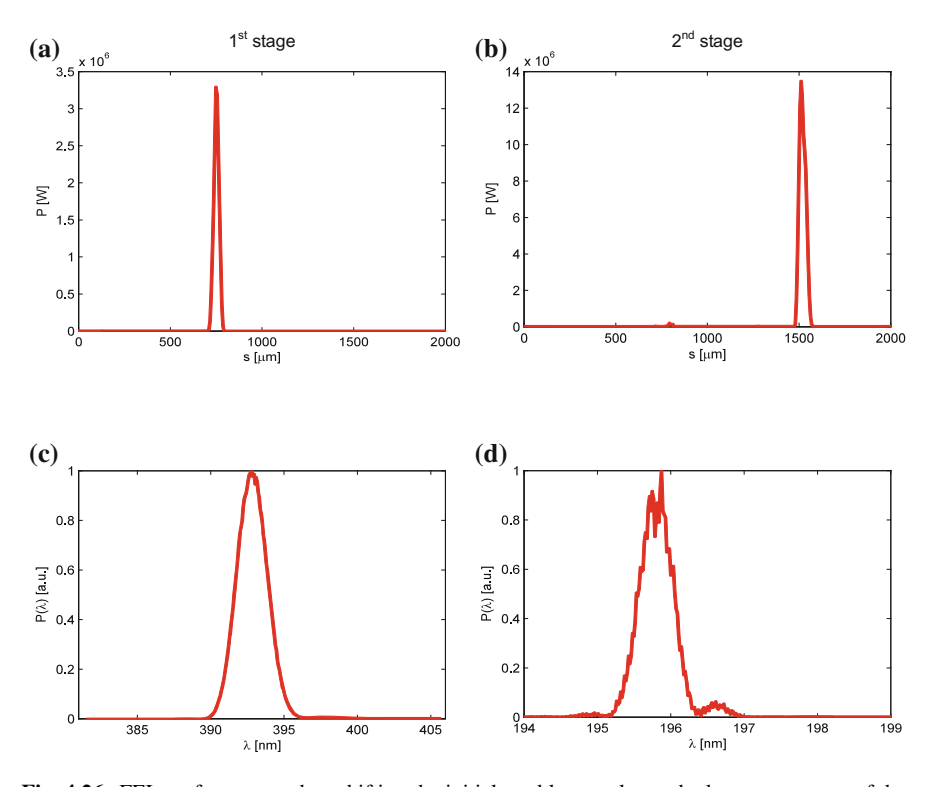


Fig. 4.26 FEL performance when shifting the initial seed laser pulse to the low current part of the electron beam: (**a**–**b**) output radiation pulses and (**c**–**d**) spectra of the radiation pulses. (Reprint from Ref. [9]. Copyright with kind permission from Springer Science+Business Media)

4.4.1.3 Demonstration of the "Fresh Bunch" Technique

Although the radiation generated by the disturbed part of the electron beam in the radiator of the second stage can be depressed by properly choosing the parameters in the simulation, it will be very challenging to find this condition during the experiment. An alternate way to intuitively demonstrate the principle of the fresh bunch technique is to characterize the energy modulation along the electron bunch. As the lasing part of the electron bunch will have an energy spread much larger than other parts of the electron beam. One will get the peak-to-trough-to-peak structures in the energy spectrum for a chirped electron bunch, corresponding to variations of the beam energy along the electron bunch.

There are 5 accelerating tanks and 3 energy spectrometers in our facility. We adjusted the phase of S4 to imprint considerable positive energy chirp on the electron beam in the simulation. If there is no energy modulation in the electron beam, the energy spectrum of the chirped beam exactly represents longitudinal density distribution. The energy spectrum can be scaled in the units of time in the beam rest frame. The phase space and energy spectrum of the electron beam at exit of the accelerator is shown in Fig. 4.27.

Figure 4.28 shows the longitudinal phase space distributions and corresponding energy sprectra of the electron beam at the exit of the two stages. After the radiator of the first stage, the lasing part is energy modulated, which will results in a valley and two peaks in the energy spectrum. The electron beam will be separated into two parts on the YAG screen after the dipole. After passing through the second stage radiator, the electron will be separated into three parts, which clearly demonstrates the fresh bunch technique (Fig. 4.29).

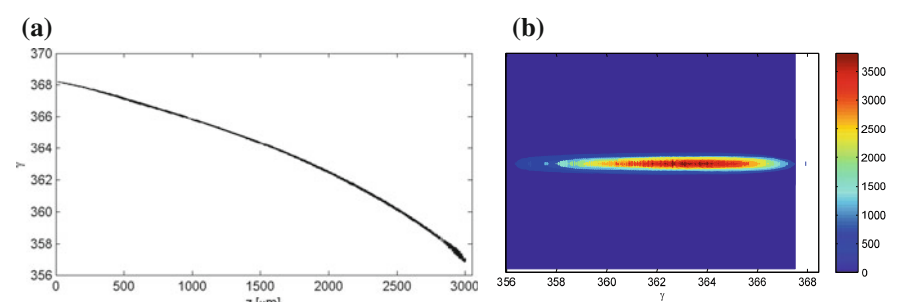


Fig. 4.27 Phase space (a) and energy spectrum (b) of the electron beam at the exit of the accelerator. (Reprint from Ref. [9]. Copyright with kind permission from Springer Science +Business Media)

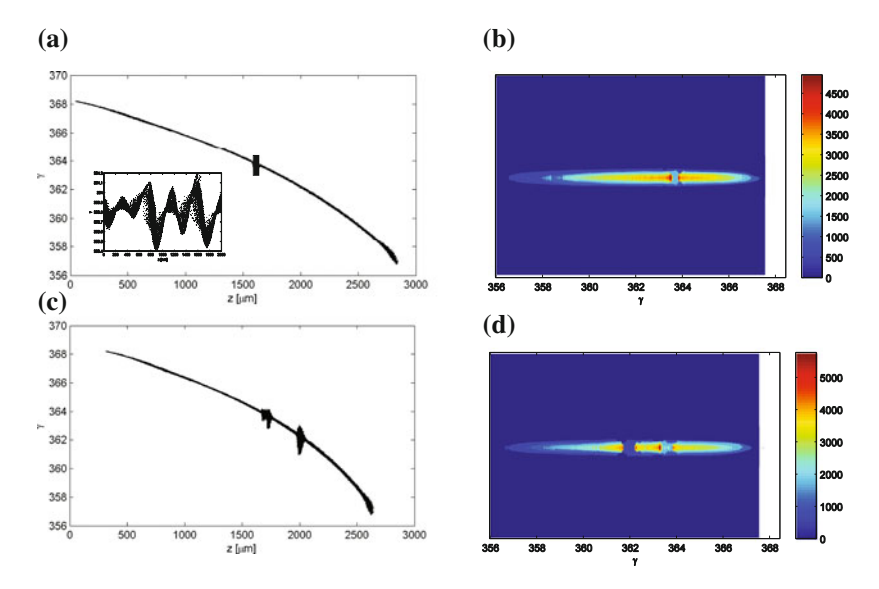


Fig. 4.28 Phase space (a) and energy spectrum (b) of the electron beam at the exit of the first stage; phase space (c) and energy spectrum (d) of the electron beam at the exit of the second stage. (Reprint from Ref. [9]. Copyright with kind permission from Springer Science+Business Media)

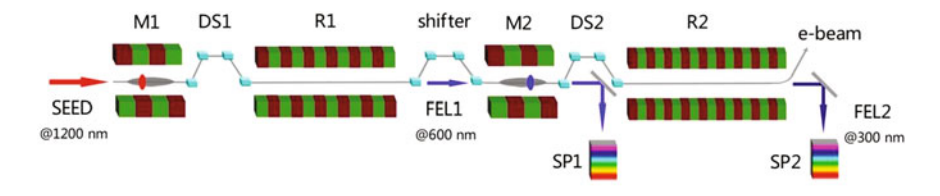


Fig. 4.29 Layout of the cascaded HGHG experiment at the SDUV-FEL. (Reprinted with permission from Ref. [10]. Copyright 1998 by American Physical Society)

4.4.2 Experimental Results of the Cascaded HGHG Experiment at the SDUV-FEL

During the cascaded HGHG experiment, the seed laser wavelength was tuned to 1200 nm by using the OPA system. The beam energy at the exit of the electron linac is set to 148.0 MeV. The radiation wavelength of the first stage is 600 nm. After the first stage, the electron beam is guided into a fresh-bunch chicane to make the first-stage radiation pulse (marked as FEL1) overlap a portion of fresh beam (marked as EB2), then FEL1 will introduce energy modulation to EB2 in the modulator of the second stage (M2). To achieve energy modulation, M2 must be tuned resonant at 600 nm. Thus, the used portion of beam (which radiated in the first stage, marked as EB1) will continue to radiate in M2 (marking this radiation pulse as FEL1p). FEL1 and FEL1p will be separated by several hundreds of

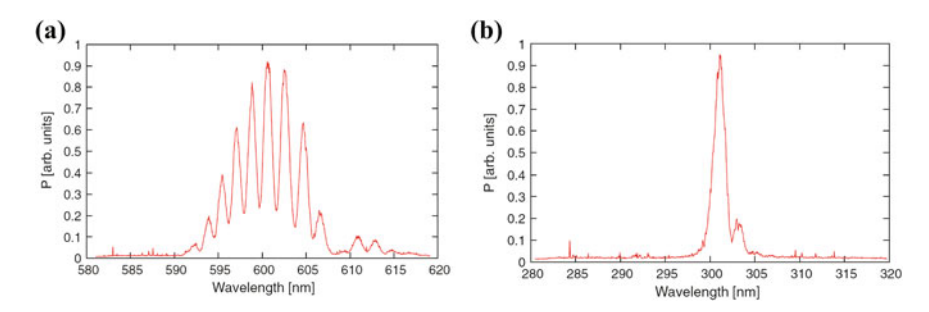


Fig. 4.30 Spectrum measurement results by (a) SP1 and (b) SP2. (Reprinted with permission from Ref. [10]. Copyright 1998 by American Physical Society)

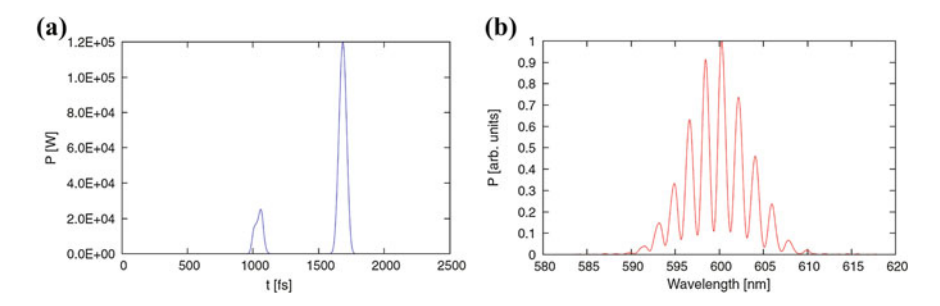


Fig. 4.31 FEL simulation results: (a) radiation pulses after M2 and (b) the corresponding spectrum. (Reprinted with permission from Ref. [10]. Copyright 1998 by American Physical Society)

femtoseconds, depending upon the strength of the fresh-bunch chicane. The observed spectrum after M2 will have some kind of interference pattern, as shown in Fig. 4.30a.

The start-to-end simulation results for the bunch refreshing process are shown in Fig. 4.31, which are consistent with the measured spectrum. The spacing between the two pulses can be easily inferred from the interference pattern, which agrees very well with the fresh-bunch chicane setting.

In the second stage, FEL1 serves as the seed and interacts with the fresh part EB2. The radiation undulators are tuned to be resonant at 300 nm, and EB2 modulated by FEL1 will lase at 300 nm, which is the second harmonic of FEL1. According to the simulation results, the residual bunching of EB1 is nearly smeared out by the dispersive sections, as shown in Fig. 4.32a. The spectrum of the second stage output and the simulation result are shown in Figs. 4.31 and 4.32. It can be seen that the start-to-end simulation results agree well with the experimental results.

References 105

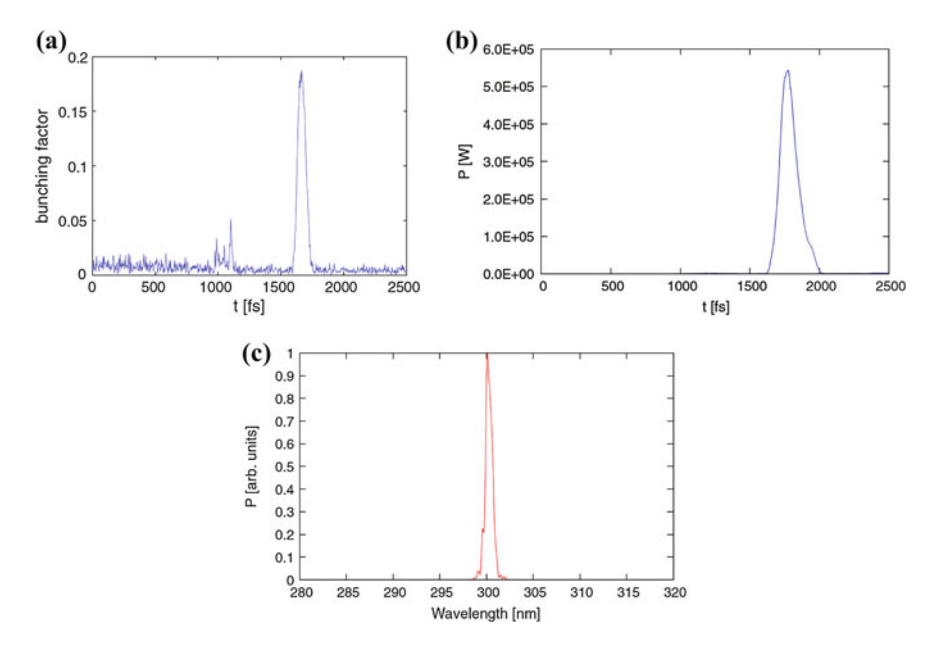


Fig. 4.32 FEL simulation results: (a) bunching factor distribution, (b) radiation pulse and (c) corresponding spectrum. (Reprinted with permission from Ref. [10]. Copyright 1998 by American Physical Society)

References

- Hüning M, Schlarb H (2003) Measurement of the Beam Energy Spread in the TTF Photo-injector. In: The 20th particle accelerator conference (PAC 2003), Oregon, Portland, May 2003, vol 3, IEEE, pp 2074–2076
- Shintake T, Tanaka H, Hara T et al (2009) Stable operation of a self-amplified spontaneous-emission free-electron laser in the extremely ultraviolet region. Phys Rev Spec Top Accel Beams 12(7):070701
- Kornyukhin GA, Kulipanov GN, Litvinenko VN et al (1985) Status of the INP optical klystron. Nucl Instrum Methods Phys Res Sect A Accel Spectrom Detect Assoc Equip 237(1):281–288
- Saldin EL, Schneidmiller EA, Yurkov MV (2005) A simple method for the determination of the structure of ultrashort relativistic electron bunches. Nucl Instrum Methods Phys Res Sect A Accel Spectrom Detect Assoc Equip 539(3):499–526
- Feng C, Zhang T, Chen J et al (2011) Measurement of the average local energy spread of electron beam via coherent harmonic generation. Phys Rev Spec Top Accel Beams 14(9):090701
- Xiang D, Colby E, Dunning M et al (2010) Demonstration of the echo-enabled harmonic generation technique for short-wavelength seeded free electron lasers. Phys Rev Lett 105(11):114801
- Zhao ZT, Wang D (2010) Progress in the SDUV-FEL and development of X-ray FELs in Shanghai. In: The 32nd international free-electron laser conference (FEL 2010), Malmo, Sweden, Aug 2010, JACoW, p 15

- Huang Z, Ratner D et al (2009) Effects of energy chirp on echo-enabled harmonic generation free-electron lasers. In: The 31st international free electron laser conference (FEL 2009), Liverpool, UK, Aug 2009, JACoW, p 127
- 9. Feng C, Zhang M, Lin GQ et al (2012) Design study for the cascaded HGHG experiment based on the SDUV-FEL. Chin Sci Bull 57(26):3423–3429
- 10. Liu B, Li WB, Chen JH et al (2013) Demonstration of a widely-tunable and fully-coherent high-gain harmonic-generation free-electron laser. Phys Rev Spec Top Accel Beams 16(2):020704

Chapter 5 Conclusions and Prospects

Abstract This chapter summarizes the main theoretical and experimental results from Chaps. 2–3 and discusses the possible applications of the new schemes and methods that draw from this thesis.

High-gain FELs hold great promise for the generation of coherent short wavelength radiation with high brightness and ultra-fast time structures, which will enable scientists in physics, chemistry, biology and medicine to study nature down to the molecular and atomic level at a time-scale that fits this resolution. Up to now, SASE and HGHG are two leading candidates for approaching VUV to x-ray region. However, they both have their own disadvantages and limitations. As the SASE FEL starts from electron beam shot noise, the output radiation typically has poor temporal coherence and large shot-to-shot power fluctuations. For the HGHG scheme, it suffers from a limited frequency multiplication factor to avoid large beam energy modulation. To improve the efficiency of frequency up-conversion and meet other requirements of FEL users, some novel high-gain FEL schemes have been proposed in recent years. In this thesis, we focus on the theoretical and experimental studies on some novel seeded high-gain FEL schemes.

In theoretical research, the technique of manipulating the phase space of electron beam, which is widely used in novel seeded FEL schemes, had been systematically studied. After that, several novel high-gain FEL schemes, mainly include the PDM, EESHG, PEHG, mode-locking seeded FEL and CPA-CHG were proposed to generate FEL with shorter wavelength, higher intensity, sub-femtosecond pulse properties, which meet the requirements of FEL users. The PDM can be used to enhance the efficiency of frequency up-conversion of a single stage HGHG or EEHG. For the PDM-EEHG scheme, simulation results shown that the bunching factor at ultra-high harmonics can be increased by a factor of about two, which indicates that coherent x-ray radiation in the "water window" (2–4 nm wavelength) can be generated directly from a 240 nm UV seed laser. The EESHG scheme is not a simple cascaded EEHG but consists of an EEHG and a conventional HGHG like configuration, which also works in EEHG principle. It was shown that a fully coherent hard x-ray radiation can be obtained directly from a conventional VUV seed laser with reduced size and cost in comparison with SASE based hard x-ray

FEL facilities. The PEHG scheme takes advantage of the fact that the TGU can introduce a transverse-longitudinal phase space coupling into the electron beam, which help us to realize the phase-merging effect and significantly enhance the high harmonic bunching factor of HGHG. It was later found that the phase-merging effect can also be realized by using a wave-front tilted seed laser. Mode-locking of seeded FEL can be used for the generation of coherent stable attosecond x-ray pulse trains via a process of mode-locking amplification. The even spacing between the attosecond pulses can be easily altered from sub femtosecond to tens of femtoseconds by slightly tuning the wavelength of one seed laser. By combining The CPA technique with HGHG or CHG, it is possible to produce intense ultra-short radiation pulses via existing seeded FEL facilities or storage ring based sources. By using the CPA-CHG scheme, the out put radiation pulse can be compressed by about two orders of magnitude by the optical pulse compressor. Theoretical and simulation studies for seeded FEL schemes with ultra-short seed laser pulses were also presented. It is found that, the seed laser imperfection experienced by the electron beam could be smoothed and compensated by the slippage effect in the modulator, which may aid in reserving the temporal coherence of seeded FELs. For longer seed laser pulses, we proposed using sub-harmonic modulator, which is resonant at sub-harmonics of the seed, to further enhance the slippage effect in the modulator.

In experimental aspect, several novel experiments have been carried out for the seeded FEL studies at SDUV-FEL. First, a simple method to accurately measure the slice energy spread of the electron beam based on CHG was proposed and developed at the SDUV-FEL for the measurement of the slice energy spread. Experimental results shown that the slice energy spread is about only 1.2 keV at the exit of the 136 MeV linac, which agrees well with the numerical simulations. This method had been used in the following EEHG and cascaded HGHG experiments. In the design study of EEHG experiment, theoretical and simulation studies of the energy chirp effects on the HGHG and EEHG schemes were present. It is found that the central wavelength and output bandwidth of EEHG can be nearly immune to the beam energy chirp by properly setting the strengths of the chicanes. The proof-of-principle experiment for the EEHG was operated in the ultraviolet region. Coherent, stable FEL pulses were generated and successfully amplified by a 10 m long undulator. The experiment results confirm the theoretical prediction of the echo effect in the electron beam and proof that the temporal coherent of the seeded FEL can be improved by properly setting the parameters of EEHG. Design studies for the cascaded HGHG experiment based on the SDUV-FEL were also given. A novel method for the demonstration of the fresh bunch technique based on the energy spectrum of the electron beam has been proposed. The first try of cascaded HGHG with the fresh bunch technique had been made at SDUV-FEL. The coherent signal from the cascaded HGHG at the fourth harmonic of the seed was observed. The experimental results fit quite well with the simulation results.